THE DEVELOPMENT OF MRI-COMPATIBLE SPECT SYSTEM

BY

JIAWEI TAN

DISSERTATION

Submitted in partial fulfillment of the requirements
for the degree of Doctor of Philosophy in Nuclear Engineering
in the Graduate College of the
University of Illinois at Urbana-Champaign, 2012

Urbana, Illinois

Doctoral Committee:

Assistant Professor Ling-Jian Meng, Chair
Professor James F. Stubbins
Professor Zhi-Pei Liang
Adjunct Assistant Professor Michael Aref

ABSTRACT

In recent years, combined MRI and nuclear imaging techniques such as PET and SPECT have received great attentions. MRI provides high-resolution anatomical and functional information along with an exquisite soft tissue contrast. Nuclear techniques could provide an excellent sensitivity to radio-labeled tracers that could be used to follow kinetic molecule interactions. In recent literatures, research on MRI/PET have been widely reported, but the development of combined MRI/SPECT is relatively limited, partially due to the stringent requirements on MRI-compatible SPECT detectors and the interferences between SPECT and MRI systems both operated at the same time.

This dissertation proposed and developed a prototype of the MRI-compatible SPECT imaging system based on a recently developed energy-resolved photon counting (ERPC) CdTe detectors. These detectors consist of CdTe detectors of 1 mm or 2 mm thickness with 350μm pixels. The emphasis of this effort is to develop an ultrahigh resolution (sub-500μm) SPECT integrated with a clinical 3T MR scanner. The designed experimental studies have demonstrated the compatibility of the ERPC detectors for operation inside the 3T magnetic. Furthermore, to achieve high imaging performance, it is crucial to develop a precise model of the charge-collection behavior for CdTe detectors operated in strong magnetic field for reconstruction. In this study, a comprehensive Monte Carlo model has been developed for predicting the response function of the small-pixel CdTe detectors operated inside the MR scanner. This model includes all major physical processes, ranging from gamma ray interactions, charge generation and drifting under strong magnetic field. This model was subsequently validated in a comparative study against experimental results and imaging performance obtained with a prototype MRI-compatible SPECT system. Finally, the experimentally calibrated detector response model was successfully applied to improve the imaging performances of several MRI-compatible SPECT systems built with different detector configurations and MR scanners of different field-strengths. This study provided critical insights for further development of the MRI-compatible SPECT system for

achieving an ultrahigh spatial resolution.

Key words: MRI-compatible SPECT system, small-pixel CdTe detectors, charge collection, clinical 3 T MR Scanner.

To Rui Wang and our parents

ACKNOWLEDGMENTS

On the completion of this dissertation, I would like, first of all, to express my cordial thanks to my graduate adviser, Professor Ling-Jian Meng, who has provided me with much guidance, support, advice, help, and encouragement, without which I would not have been able to complete this work. All I have learned during my study and research under Professor Meng's direction will continue to be of great benefit to every aspect of my future career and the rest of my life.

My sincere thanks also go to Professor James F. Stubbins, Professor Zhi-Pei Liang, and Professor Michael Aref for serving as members of my doctoral committee and for their valuable time and important suggestions. I would like to thank every current and former member in Professor Meng's research group and the department of Nuclear Plasma and Radiological Engineering at the University of Illinois at Urbana-Champaign for their helpful discussions and suggestions. I specially want to thank Dr. Geng Fu for his pioneering work in the high spatial SPECT imaging and for his valuable help when I first started on this topic. I would also like to thank Nan Li and Liang Cai who collaborated with me on research projects. Finally, I want to give my sincere gratitude to my husband, Dr. Rui Wang, and our parents for their dedication and their continued love and support.

TABLE OF CONTENTS

CHAPTER 1
INTRODUCTION

Traditional imaging technologies, such as CT, MRI, SPECT/PET, ultrasound, and optical imaging, are important tools to track the biological effects and diseases in *in vivo* small animal imaging, where these technologies map particular molecules or proteins in high-resolution images. Each of these technologies has their own advantages as well as limitations, and therefore, the so-called multi-modality imaging, which combines the advantages of individual imaging techniques, have recently received increasing attention and popularity. This chapter reviews the advantages and challenges of traditional imaging technologies and introduces multi-modality imaging for *in vivo* small animal imaging applications.

1.1 Nuclear imaging technologies

Nuclear imaging techniques, including single photon emission computed tomography (SEPCT) and positron emission tomography (PET) are based on the tracer principle and external detection. This type of imaging techniques is able to provide information regarding radioactivity concentration inside the tissue and quantify the kinetic process when the drugs interact with and radiolabel molecules inside the body.

A unique advantage of nuclear imaging is the capability of allowing some biological tissues or cells labeled by particular isotopes, called radiotracers, without changing their biological properties. Also, the photons emitted from the radiotracers often carry sufficiently high energy to penetrate tissues several tens of centimeters thick, enabling non-invasive imaging of animals and human body. Various kinds of radiotracers are developed for this purpose and used in clinical application for different functions and targets. A list of radiotracers used in current nuclear imaging is shown in Table 1A [1]. On the other hand, nuclear imaging suffers a major drawback since it is typically associated with appreciable dose from ionization radiation. In the following

sections, two major nuclear imaging modalities, SPECT and PET, are discussed and compared in detail.

Table 1A [1]: Radiotracers used for in vivo nuclear imaging

Radiotracers	Half life	Photon energy (kev)	Imaging modality
C-11	20.4 mins	511	PET
F-18	110 mins	511	PET
Cu-64	12.7 h	511	PET
Tc-99m	6.02 h	140	SPECT
In-111	2.83 days	171,245	SPECT
I-123	13.2 h	159	SPECT
I-124	4.18 days	511,603,723,1690	PET
I-125	60.1 days	27,31,35	SPECT
I-131	8.04 days	364	SPECT

1.1.1 Positron emission tomography

A PET system typically consists of a single ring or multiple rings of detector elements that are working in coincidence around the objects or patients. These detectors are used to detect two simultaneous annihilation photons, which are emitted back-to-back when radionuclide decays and emits positron. Detection of the annihilation photons can be used to determine the original positron decay event onto a so-called line of response (LOR) across the object. Therefore, PET requires no physical collimator and offers a much higher sensitivity than SPECT. The PET imaging process, PET image and system are shown [1]-[4].

Several types of detectors for molecular imaging applications can be used in the PET imaging system, such as scintillator photomultiplier tube combination, semiconductor detectors, and depth-of-interaction detectors. Some detector designs are capable of delivering spatial resolutions of around or below 1mm [2].

Modern PET technology has achieved considerable commercial success in small animals

imaging and medical imaging. However, this technology still faces several challenges. First, the spatial resolution of PET is restricted by the movement of positron before annihilation, which can vary with the energy of the emitted positrons. Second, the performance of the PET system is limited by the performance of detector as well. An ideal detector can achieve both high detection efficiency and accurate localization for 511kev photons, which can be very challenging in reality. In fact, 511 keV gamma rays can easily be scattered (Compton scattering), and result in multiple interaction locations for single incident photon, which affects the determination of initial interaction of incident photons. Sometimes, the thickness of detector is purposefully reduced in order to minimize Compton scattering, but the detection efficiency is degraded as a result.

1.1.2 Single photon emission computational tomography (SPECT)

A typical SPECT system consists of multiple detectors with ring configurations around the objects, and collimators placed between the detectors and objects to select the gamma rays from certain incident direction. SPECT images are obtained by acquiring multiple 2D projections from a range of angular positions, and 3D images can be constructed from the 2-D projections. Compared to PET, SPECT imaging is able to deliver ultra-high spatial resolution and allow multi-dimension imaging, i.e., simultaneous imaging by labeling different biological processes with different isotopes.

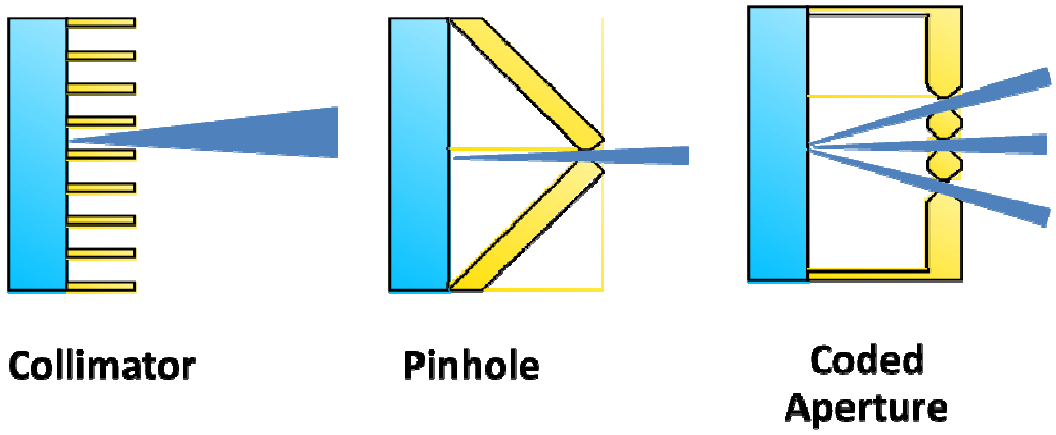

Figure 1A: Three collimators used in SPECT imaging.

There are three classes of collimation methods currently used in SPECT systems: parallel collimator, pinhole collimator and coded aperture, which are shown in Figure 1A, respectively. Adopted in this dissertation work, the pinhole collimator achieves highest spatial resolution among the three, as the image of the object is magnified through the pinhole and projected onto the detector. Recent development on the high-resolution compact detectors [5]-[8] and collimator designs [9]-[10] further improves the spatial resolution of SPECT.

However, high spatial resolution in SPECT is achieved at the expense of field of view and sensitivity since high spatial resolution often means smaller pinhole size. To address this problem, one may consider placing the object closer to the collimator, which is straightforward but less effective. In fact, several detector and pinhole collimation techniques were developed recently to provide both spatial resolution and high sensitivity in SPECT. For example, researchers use multiple detectors surrounding the small animals [7], [12] (U-SPECT-I and FastSPECT II) or multiple pinholes in each collimator with projection overlapping for reconstruction [9] [11]. Another example is the NanoSPECT system [13]-[14], which allows automated 3D-translation stage to enable the helical scanning and translation-SPECT with multi-pinhole collimators.

Despite all these efforts, the sensitivity of SPECT is still limited compared to PET, and the increased sensitivity from the approaches above cannot lead to the improved signal-noise ratio directly, because the every detected photon carries less information than the photon from the original system.

1.2 Other Imaging Systems

1.2.1 Optical imaging

In in vivo small animal imaging, optical imaging is also an important approach, which can provide extremely high sensitivity. This approach uses the light scattered or absorbed by the tissues, and lights emitted from the deep inside the small animal can reach the light sensor (conventional CCD camera) outside the body, even with multiple scattering before being detected. The image can be reconstructed by obtained light intensity spectral and spatial information.

Currently, two optical mechanisms are used in imaging applications, fluorescence [32] and bioluminescence [33]. Firstly, fluorescence uses the external light source with filter to excite the fluorescent molecules, which is engineered in the mouse body genetically. GFP has been used as a successful fluorescent molecule and used in some in vivo imaging studies. Also fluorophores are used to introduce the fluorescent molecule. This process is to label the interesting molecular as radioisotope labeling but with some limitations. The fluorescence imaging has high quantum yields and the fluorescence lights are only emitted by the particular molecular, which leads to low background noise and allow low concentration imaging. However, in this approach, some fluorescence from tissues can cause some background noise. In addition, depth dependent excitation and light scattering are also problems affecting the image quality. Secondly, Bioluminescence is to introduce reporter genes to catalyze light-production by enzymes. Unlike the fluorescence imaging, bioluminescence has no requirement of external light source, and thus there is no background noise from tissue fluorescence and no strong depth dependent light emission based on penetration of excitation lights. However, the bioluminescence signal is very weak, and the sensitivity is relatively low, but the development of CCD technology has improved the imaging sensitivity.

1.2.2 Ultrasound

The ultrasound is an adapted imaging approach for human being and small animal imaging, and has capability of the molecular imaging. The ultrasound imaging allows the high spatial

resolution in tens of microns, low cost and real time imaging with no ionization radiation. The image quality and spatial resolution is related to the depth of penetration and the acoustic frequency. The small animal only has depth of 1-2 cm, which is relatively short, and 20-60MHZ acoustic frequency can be used to achieve very high spatial resolution. The real time imaging is one important advantage for particular medical application, such as cardiac imaging for phenotypic analysis. In addition, the ultrasound (Doppler flow mapping) can also allow the quantitative measurements of blood flow.

In the recent years, some researchers have developed several ultrasound systems for small animal studies. Forster et al (2002) [34] developed a system for micro-imaging. Most research focus on phased array transducers with high bandwidth, signal processing for the high frequency and investigation on non-linear contrast agent response to incident ultrasound radiation.

1.3 Multi-modality imaging system

Multi-modality imaging is an integration of two or more imaging systems for single target application with multiple markers. In addition to the images of target molecules, it's desirable and helpful to achieve both functional and structural images of the same animal or patient. In clinic application, the multi-modality imaging has been rapidly evolved in molecular imaging, which can provide the exact localization in surrounding organs. The CT and MRI are excellent tools for high quality anatomical information. The best examples of integrated imaging systems are PET/SPECT-CT PET/SPECT-MRI. Recently, the current software algorisms have been studied for long time and ready for the co-registration or fuse the images from different separated imaging systems, but the software technologies are restricted due to the organ movement and the dynamic changes. Therefore, a more acceptable approach is either to transfer the object filled with multi-modality markers from one imaging system to the other by use of the common object holder for transportation or to build a dual-modality imaging system, which allows the simultaneous imaging of the same animal by each imaging system and does not move it during

the entire process.

1.3.1 PET/CT and SPECT/CT systems

The most used integration of multi-modality imaging systems is CT combined with nuclear imaging system (PET or SPECT), which has been applied in clinical applications. X-ray CT images provide detailed structural information with a rapid data acquisition, while emission tomography images provide functional information by forming a map for the decay positions of radioisotopes used to label the molecules, ligands etc. Within the past decade, combined SPECT/CT and PET/CT systems have become standard in both pre-clinical and clinical applications.

Dual-modality imaging systems have several advantages. First, CT is a primarily imaging tool to provide structural information, which helps to localize various types of tissues and reveal their anatomical structures. Second, CT scan could provide 3D attenuation information for subsequent correction of PET or SPECT images. To account for the fact that some photons emitted inside the body cannot arrive at the detectors due to scattering and absorption inside the body, one would require a precise attenuation map. It is worth noting that the CT-based attenuation map cannot apply on the SPECT/PET correction directly. The x-ray photons used in CT imaging are generated by an x-ray tube, which are inherently polyenergetic. By contrast, the photons emitted from radioisotopes are monoenergetic with the higher energy. Therefore, the attenuation map for radioisotope photons in different tissues are derived from the CT data by several developed methods [15]-[17].

A simultaneous CT and PET system was first developed (Goertzen 2002) [18][19], and the sequential CT and SPECT or PET have been reported by many groups, and a CT/SPECT system based on EMCCD camera has been developed by our group recently [20], which could deliver the image with high spatial resolution<500 microns (as shown in Figure 1B).

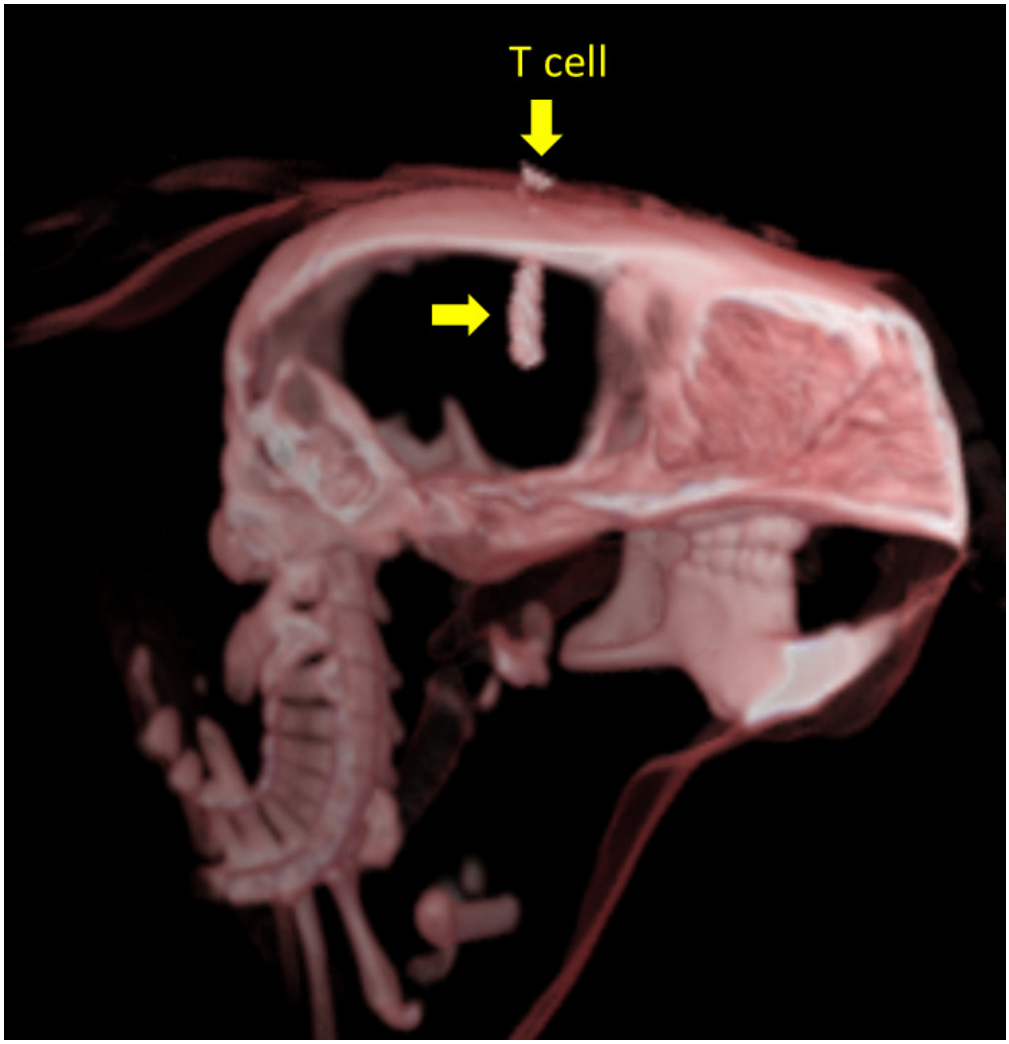

Figure 1B: Fused CT and SPECT images (labeled by I-125) for mouse brain. Courtesy of Dr. Ling-Jian Meng and Dr. Geng Fu, University of Illinois Urbana Champaign.

1.3.2 PET/MRI system

Even with the successful combination of PET/SPECT and the x-ray CT, the patient has to face more ionization radiation. Another modality Magnetic Resonance Imaging (MRI) may take advantage of both high spatial resolution structural image and no ionization radiation. Therefore, the next attempt is to integrate the MRI with the nuclear imaging systems. The MRI is one primary medical imaging technique since in the middle of 1970s, which is used to measure the

physiological parameters and follow the anatomic change in soft tissues related to intervention or diseases in living animals. Compared to the traditional CT, MRI can provide much greater contrast between the different soft tissues inside the body with no ionizing radiation. It uses a powerful magnetic field to align the nuclear magnetization of hydrogen atoms in water of the body, and then a Radio frequency (RF) field is used to systematically change the alignment of this magnetization. This process leads to a rotating magnetic field produced by the hydrogen nuclei, which is detectable by the scanner. Most small animal imaging is currently using MRI with magnetic field strength 4.7T 9.4T 11.7T and even up to 21.1T.

Some image alignment algorithms are available to co-register the MRI and PET images from two separate systems for small animal studies, but it is not optimized. A better approach is that either transfer small animal from one imaging modality to the other by using specially designed bad with multimodality markers or doing simultaneous or near simultaneous imaging without moving small animals, which provides high accuracy of anatomic localization for PET uptake and are more suitable for dynamic imaging studies.

One of the major difficulties for combining nuclear imaging techniques with MRI is the potential interference between both modalities. The presence of PET/SPECT inserts cause interference on MRI imaging by disturbing the homogeneity of main magnetic field. Due to the materials used to make those components, the eddy currents may be generated in those components. On the other hand, the strong magnetic field and gradient field may interference the photon detector response. Traditional PMTs cannot directly used in even weak magnetic field, and thus the PMTs have to be placed far away from the magnetic field and connected by long optical fibers, but long optical fiber leads to attenuation of scintillator lights and energy resolution of detected events. Therefore, the PMT-based PET systems are limited for use of PET/MRI system. Recently, some groups applied the APDs for light readout in their PET/MRI, capable of operating simultaneously with MRI with no significant distortion, has been reported in [21]-[25]. In semiconductor detectors, the incident photons can be converted to charge carriers (electron and hole), which are

collected by electrodes. When thin detector used, the detection process and signal readout of semiconductor detector are nearly unaffected by the main magnetic field. The use of APD has some challenges for magnetic field environment. The performance of the detector is largely depending on the temperature and bias voltage, and the signal readout requires the preamplifier attached adjacent to the detector. A MRI-compatible PET system has been developed in University of California Davis (Cherry 2006) based on the lutetium oxyorthosilicate (LSO) as the scintillator and position-sensitive avalanche photodiodes (PSAPD). Short optical fibers are used in this system. There are other researchers who developed PET insets without optical fiber and APDs associated with readout electronics are all attached with scintillator elements (Pichler 2006) [25]. These reported PET/MRI system demonstrated the feasibility and perspective of this dual-modality system for multiple imaging applications.

1.3.3 SPECT/MRI system

There are relatively few publications on combined MRI/SPECT system. This is partially due to the lack of MRI-compatible detectors and the need for detector motion that may interfere with MRI data acquisition. Similar to PET imaging, semiconductor detectors are recently used to replace scintillator detector in SPECT. To make SPECT system working inside MRI, one has several design considerations to achieve good imaging performance. In addition to the consideration mentioned in PET/MRI system, detection process in SPECT is affected by the strong magnetic field. Especially for the thick pixel detector, the incident gamma ray induced charge carrier drifting path always affected by magnetic field, which leads to projection shifting and the position error or blurring in reconstruction.

Recent efforts on the development of MRI-compatible PET imaging modules with new detector techniques [21]-[25], and shielding or collimation materials [26] for use inside MRI systems without introducing severe interference between both modalities. In addition, CdTe/CZT detectors has been proved strong magnetic field compatible recently and considered an excellent gamma ray sensor candidate for MRI/SPECT system. Wagenaar et al. has reported the design

considerations of an MRI compatible SPECT system based on CZT detectors [27]. A prototype of MRI compatible SPECT system developed by the same group has been reported in [28]. Breton et al. [29] and Goetz et al. [30] have reported the use of a conventional PMT based SPECT system in a low field (0.1 T) MRI system for dual-modality small animal imaging.

Similar with PET inserts, to implement the simultaneous imaging of SPECT and MRI, it demands that the inference between the SPECT and MRI should be minimized with the presence of all the SPECT components. Therefore, all the SPECT inserts have to be made of low magnetic susceptibility materials, including mechanical supporting, shielding, collimation materials and structure, to avoid the degradation of MR images. Although the semiconductor detectors used for SPECT provide the possibility of imaging operated in MRI, the specific MRI-compatible ASIC has not been developed, and thus several technical challenges are still needed to be considered. Another restriction is that the relatively small space of MRI scanner bore limits SPECT system placement inside MRI, which leads that only compact detectors have to be used in the MRI-compatible SPECT system.

A MRI-compatible SPECT system based on pixel CdTe/CdZnTe detectors and multiple-pinhole aperture are developed in University of Illinois at Urbana-Champaign. The motivation for this work is to develop a SPECT system based on the CdTe detector that can be used inside a pre-existing 3T MRI scanner. This system is designed to offer a very-high spatial resolution <500 μm when operated inside the MRI system. To achieve these targets, we proposed to use high-resolution Energy–Resolved Photon Counting CdTe detectors [31] in a stationary ring configuration that is placed inside the MRI system. For developing such a system, there exist several uncertainties that need to be addressed:

1) Will the high-resolution CdTe detectors proposed work in strong magnetic field?

2) With the presence of the CdTe detectors and the associated electronics, can MR images be acquired without severe distortion?

3) What material should be used for SPECT apertures or other SPECT components without introducing severe interferences in MR images?

4) Will the strong magnetic field affect the detector response, spatial resolution, and reconstruction process?

5) How is the imaging performance of MRI-compatible SPECT system by using varying different detectors (1mm 2mm and 5mm in thickness) and in different magnetic field strengths?

6) How the images of phantom obtained in 3T MRI?

All these questions will be discussed in the following chapters.

1.4 Outline of the Dissertation

The remaining chapters of this dissertation are organized as follows:

Chapter 2 reviews hybrid pixel detector, including hybrid detector fabrication process, bump-bonding and CMOS process, along with the ASIC design of the Energy-resolved photon counting (ERPC) detectors. In addition, the development of ERPC detectors by using different crystals are presented, finally some preliminary results on the detector uniformity and the energy resolution of all individual pixels are used to prove the performance of the ERPC detectors.

Chapter 3 describes the prototype of a SPECT system based on a single ERPC detector. To investigate the detector response, a pencil beam source is formed to irradiate detectors with the known incidences for charge sharing evaluation. Then the design of the SPECT system based on single detector, including, detector arrangement, collimation, shielding, and support mechanics, are discussed. All the components placed in MRI-compatible SPECT system are selected and tested in strong magnetic field. Some MRI images acquired with presences of SPECT detector and collimator candidates in the 3T MRI scanner are displayed. Finally some preliminary imaging studies by using Co-57 sources were obtained, along with imaging study in 3T MRI scanner with the same source and SPECT scanning geometry.

Chapter 4 begins with the introduction of the detection process of the gamma ray by using semiconductor detector. We built a Monte Carlo simulation model covering all the physics from initial gamma ray interaction down to measurable signal and signal readout chain to produce energy spectra of selected detector pixels. The parameter used in the model is calibrated and

compared to the measured results. Experimental validation is designed to form known irradiation geometries. The simulated energy spectra are compared with measurements and prove the accuracy of the model. When considering the strong magnetic field, the observed distortion on the pixel detector is also modeled to compare with measured detector response in 3T MRI scanner that helps to refine the SPECT system response function (SRF) in reconstruction. Simulated SPECT images of mouse brain are compared with refined SRF and normal SRF. The refined SRF improves the image quality and spatial resolution. Several cases are discussed, such as by using different detectors on varying magnetic field strengths.

Chapter 5 presents our MRI-compatible SPECT system based on 1mm and 2mm ERPC detectors. Every SPECT components, such as detector housing, arrangement, cooling and non-magnetic mechanics, are described in this chapter. In addition, the detailed distortion in the projection due to both Lorenz force (first-order effect) and uniformity of magnetic field (second-order effect) is investigated experimentally. Some phantom studies are implemented by this setup, and reconstructed images by using the normal SRF and refined SRF are presented.

Conclusions and proposed future work are given in Chapter 6.

CHAPTER 2
CdTe/CdZnTe(CZT) HYBRID PIXEL SENSOR

Pixelized CdTe/CdZnTe detectors have several attractive features for detecting x-rays and low energy gamma rays. As semiconductor materials, both CdTe and CZT have relatively large band gap, leading to low leakage current and excellent energy resolution at room temperature, and provide large stopping power and excellent detection efficiency for low energy gamma rays commonly seen in SPECT imaging. In addition, it is easy to fabricate detectors with small pixel sizes that result in good spatial resolution. Several research groups have developed and evaluated CdTe or CdZnTe detectors of various configurations [35]-[42] for SPECT imaging systems.

In this chapter, we discuss the design and development of a so-called Energy-Resolved Photon Counting (ERPC) CdTe detector for use in SPECT imaging. The ERPC detector is designed based on hybrid detector concept. In this design, the CdTe crystal is tailored to 2.2 cm ×1.1 cm and bump-bonded on top of ASIC module with the same size. Each hybrid detector has 64 × 32 pixels with pitch size 350μm, and the ASIC circuitry of each pixel consists of amplifiers, discriminators and the basic counter. To enable capability of spectroscopic measurement, an analogue-to-digital converter (ADC) is added onto each pixel channel at a relatively high count-rate for gamma ray interactions, which is developed by our group, in conjunction with Ajat Oy Ltd, Finland [43]. In addition, a time stamp in pixel can in principle be obtained for each event, which enables coincidence measurements typically required in PET applications. More details on the front-end circuitry and signal processing methods are described in chapter 2.2. In general, the ERPC detector combines very high energy and spatial resolution, and a reasonable count capability, which are necessary for future SPECT applications. Preliminary experimental results are presented in this chapter.

2.1 Introduction of hybrid pixel detector

The ERPC detector uses a typical hybrid detector configuration. This configuration is by making the detector and ASIC assembled by flip-chip bonding, in which one piece is made flipped to other surface. During this process, each detector pixel is connected to the ASIC pixel by a conducting bump, such as indium, gold, solder or conducting glue. So far, several techniques have been developed and reached reliability. The schematics and of a hybrid pixel detector are shown in Figure 2A [44] [45].

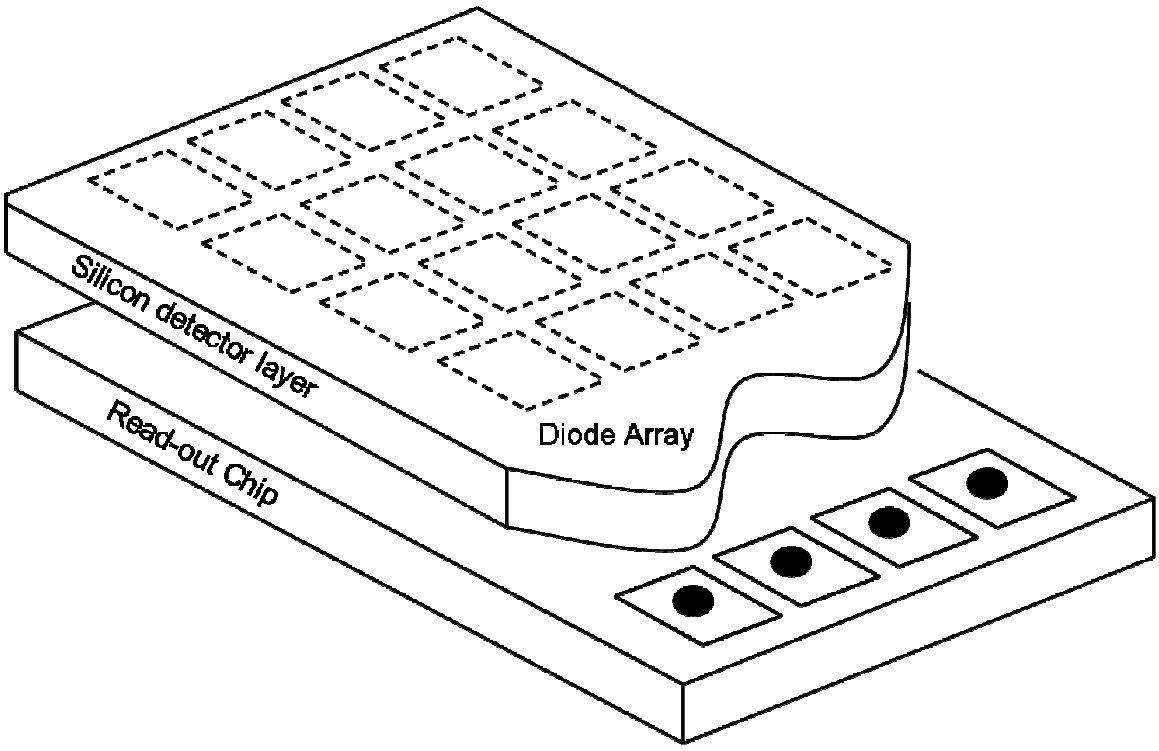

Figure 2A: Schematics of a flip-chip pixel detector with attachment of detector and ASIC

With the highly pixelated hybrid structure, each pixel channel of circuitry contains a signal readout unit, including a pre-amplifier, a main amplifier, and peak-hold circuitry. To develop a hybrid pixel detector with high intrinsic spatial resolution, several other functions need to be included for signal readout for each pixel unit, such as signal amplification, storing and

discrimination, noise filtering, and signal restoration. In addition, one has to incorporate address-decoding and to allow for selection among different readout modes. The physical dimension allowed for those functions should be within a single pixel area. Therefore, each pixel has the capability of spectroscopic measurement for the incident gamma ray and providing accurate spatial information of interactions. Given the large number of pixels to be read out, many recently developed ASICs offer a special mode called sparse readout. It allows one to read out only those channels with induced signals. Similarly, some readout systems allow one to read out several columns of pixels around the specific pixel with a real signal. Sometimes, there is a universal threshold will be set for select events, or all the signals from all detected events are stored. On the ASIC, each pixel could work in both photon-counting mode and energy resolved mode for direct measurement of the signal amplitudes. All the functions mentioned above are implemented within a very small area (350μm×350μm) for single pixel. In this chapter, the design of ERPC ASIC is presented.

The most commonly used technology of constructing integrated circuits for pixel detector is Complementary metal–oxide–semiconductor (CMOS) [46]. The CMOS electronics uses p-type and n-type metal oxide semiconductor field effect transistors (MOSFETs) in devices, which are insulated to each other, since one of them is placed with doping to the bulk material to form a well by diffusion.

However, the property of the p-type and n-type devices is not perfect, due to difference of mobility of electron and holes (holes move much slower than electrons under the same situation), In addition, the bulk concentration varies significantly. Therefore, similar process may cause different transistor geometries, which may indirectly affect the uniformity of the detector.

2.2 Design of the ERPC detectors

2.2.1 Basic ERPC detector design

The objective of this work is to develop a high-resolution gamma ray camera for small animal imaging studies. For this purpose, there are two design considerations for gamma ray imaging application. Firstly, *in vivo* SPECT imaging, it is critical for a system to achieve a reasonable balance between spatial resolution and detection efficiency. Although some researchers reported the imaging system with spatial resolution <200μm, but volumes with pixel physical dimensions close to the resolution capability may not contain adequate activity to maintain a sufficient counting statistics in projection acquisition. In our implementation, we have chose a target resolution ranging from 250 to 350 μm for small animal SPECT applications. Secondly, charge sharing between adjacent anode pixels is another issue for highly pixelized detector design, which is confirmed to degrade energy resolution. In principle, the energy resolution degradation can be reduced, if signals of all adjacent pixels around the triggering pixel are induced and summed. However, it doesn't help to recover the charge loss due to the gap areas between pixels. To minimize the multiple pixel events, the detector pixel should be designed acceptable for the target spatial resolution. With ~350μm pitch size and 300μm anode size, the possibility of charge shared events could be reduced less than 10% for 140 keV full-energy gamma ray interactions, which is good enough for SPECT application.

The Energy-Resolved Photon Counting (ERPC) detector is designed based on the hybrid detector concept, which is made up with multiple hybrids of 2.2 cm × 1.1 cm in size [47]. Each detector hybrid consists of a highly pixelized CdTe (or CZT) crystal that has a 64×32 array of square pixels with a pitch size of 350μm × 350 μm, which is bump-bonded to custom-designed readout ASIC. As the Figure 2B, each detector hybrid is wire-bonded to a readout PCB and an external cable is used to connect PCB and host PC. For the SPECT application, CdTe crystals up to 2mm and CZT crystals up to 6mm in thickness are proposed to be used in the EPRC detector design, which provides an excellent detection efficiency up to 100% for 30keV gamma rays, ~90% at 140keV and ~75% at 159keV. A schematic of the ERPC modular detector is shown in

Figure 2B, and photograph of the single detector module is shown in Figure 2C.

In our prototype system, there is no steering grid is implemented between the anode pixels, but a guard ring surrounding the 32×64 pixel array, 25 mm in width. The total gap between the guard ring and adjacent anode pixels is 50 mm. During the operation of detector, a bias voltage of 200V

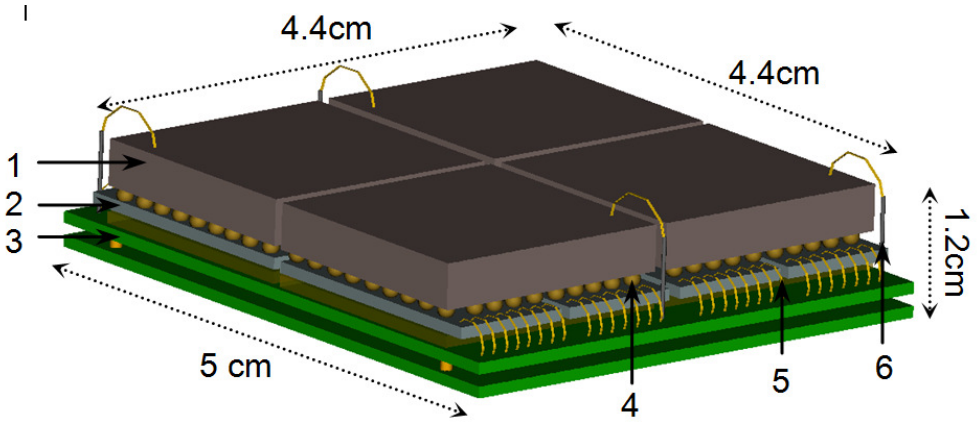

Figure 2B: The proposed ERPC detector. (1) CZT crystals of 4.4cm × 4.5 cm × 2-4 mm in size, (2) ERPC ASICs, (3) Readout PCBs, (4) indium bump-bonding between CZT detector to the ASIC, (5) wire-bonds between the ASIC and the PCBs and (6) Cathode signal out.

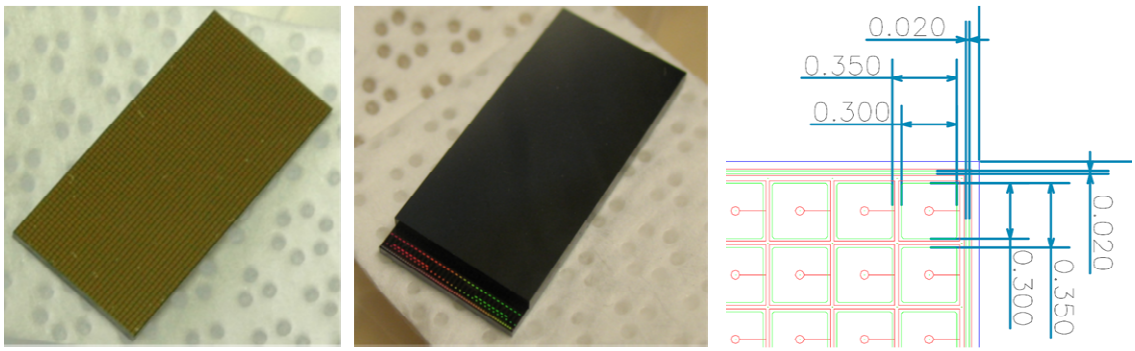

Figure 2C: (left) Single ASIC module of 11mm × 22mm × 1mm in size and having 32×64 pixels with 350µm × 350 µm pixels; (Middle) single crystal-ASIC hybrid module; (Right) pixel configuration layout.

for 1mm thick crystal (400V for 2mm crystal) is applied to the cathodes. For low energy gamma rays of 140keV, the induced the photoelectrons or Compton recoil electrons by incident gamma ray have very short drifting range. This process leads to the generation of the initial electron cloud with small dimension around 10μm. With the actual anode pixel area 300 μm ×300 μm in size and inter-pixel gap 50 μm in size, the initial electron clouds created by gamma ray interaction are collected in single pixel volume (single-pixel event) mostly. Moreover, the probability of single-pixel events should be dominated under the current detector configuration and properly further increased by reducing the size of the inter-pixel gap.

2.2.2 Front-end readout circuitry

In the ERPC detector design, the CdTe/CdZnTe detectors are flip-chip bonded onto a newly designed application specific integrated circuitry (ASIC). Each ASIC is 22 mm × 11 mm in size with pixel pitch size of 0.35mm × 0.35mm. Each CdTe/CdZnTe crystals are tailored to match this pixel configuration. Each pixel circuitry contains signal readout components and associated logic units. In signal readout, bump-bonding pad, an AC-coupled charge-sensitive amplifier, filtering amplifier (shaping time of ~1μs), a peak-hold circuitry, a comparator and a 10-bit multi-function counter are used for both photon counting and A-to-D conversion (as shown in Figure 2D). Meanwhile, various logic units for controlling, address decoding and selection between readout modes are also designed for each pixel. An external analog controlling voltage is used for adjusting the threshold for each pixel. In addition, all the wire-bonding pads, control signals, power feeds and output signals are located at one edge of the ASIC module (as shown in Figure 2G). The detailed parameter of ASIC design is shown in Table 2A.

Each detector pixel has different response due to varying offset and gain, and thus causes energy resolution degradation when collecting spectrum by all pixels. To address the issue, each pixel channel is equipped with two 8-bit digital-to-analogue converters (DACs) to compensate the pixel-to-pixel variation of energy scale by offset and gain. This accurate energy scale alignment of all 16384 readout channels of the detector allows the high performance and the energy

resolution of the entire detector (all pixels) would be improved to be close to the energy resolution measured by individual pixels.

When the gamma ray interacts with the detector, a trigger signal from anode pixel is generated to kick off the 10-bit time-to-digital converter (TDC), and also the same trigger signal starts a ramp generator, which is implemented by using a 10-bit digital-to-analogue converter (DAC). This DAC is driven by a clock signal working at 10MHz. After triggering, this ramp generator produce a steady increased ramp signal, which is compared with the signal held by the on-pixel P/H circuitry in Figure 2E. If the two signal amplitudes are closed to each other, then another trigger signal is generated to stop the TDC immediately. Therefore, the time interval between the start and stop trigger of the TDC is ideally proportional to the anode signal amplitude induced on the corresponding pixel, and the energy deposited in corresponding pixel can be recorded. In addition, the signal from the cathode can be readout be a discrete amplifier and A-to-D conversion. Since both anode and cathode signals can be readout, the depth-of-interaction information can be derived based on the signals from both electrodes (as shown in Figure 2F).

To satisfy count rate requirement in different SPECT applications, this novel ASIC has the capability of on-pixel A-to-D conversion with variable precisions. With the current ASIC design, one can choose to digitize the analogue signal with both 6-bit and 8-bit precision based on the desired count rate, which is implemented by changing the step size of the ramp generator. A maximum of 6.4μs and 25.6μs are used to perform a 6-bit and 8-bit A-to-D conversion for each event, and up to 100k counts per second (cps) with 6-bit and 25k cps with 8-bit ADC precision are allowed for the current ASIC design. When counting total eight independent hybrids for one detector, each ERPC detector has a capability of a count rate of 0.8M cps or 0.2M cps depending on the ADC precision. This count rate capability is adequate enough for most SPECT imaging application, since event rate to detectors is very limited with high-resolution collimation apertures used in imaging process.

TABLE 2A: Design Specifications for the ERPC ASIC

Physical dimensions	1.1 cm × 2.2 cm, with 32×64 pixels
Pixel size	350 μm ×350 μm
Preamp gain	10 μV/electron
Shaping time	~1μs
Gain correction	8-bit
Offset correction	8-bit
Threshold control	10 bit common to all channels.
ADC	On pixel, 6-bit or 8-bit
Readout modes	▪ Photon counting. ▪ Energy resolved readout with on-pixel ADC
Count rate capability	▪ 0.25Mcps per pixel in photon counting mode. ▪ 0.8M cps with 6-bit ADC and 0.2M cps 8-bit ADC
Energy resolution (with CZT detector)	3-4 keV FWHM @140keV (measured)
Dynamic range	12 keV – 250 keV

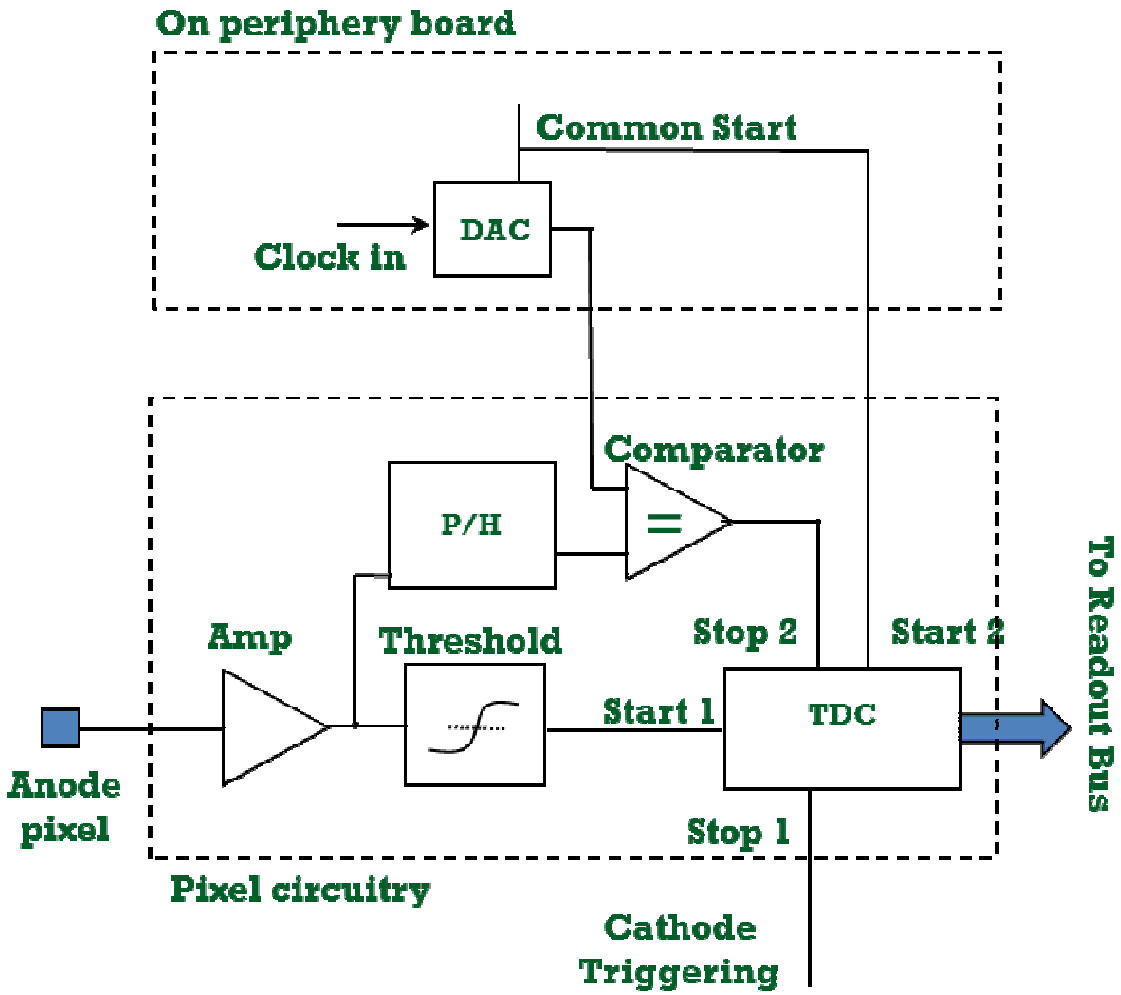

Pixel circuitry

Figure 2D: Circuitry for each CMOS pixel

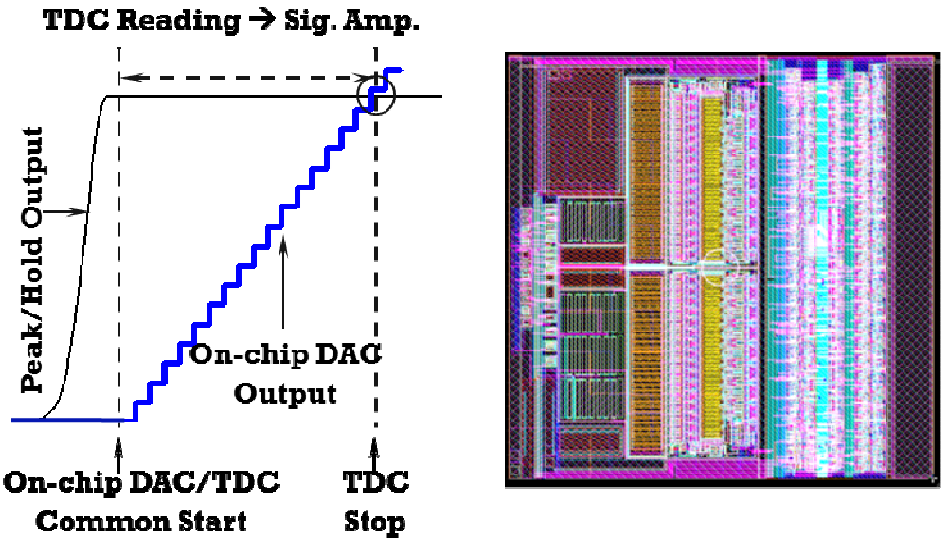

Figure 2E: (Left) signal from ramp generator and signal in P/H circuitry; (Right) Pixel layout: 350 µm×350 µm, containing 2682 electrical components

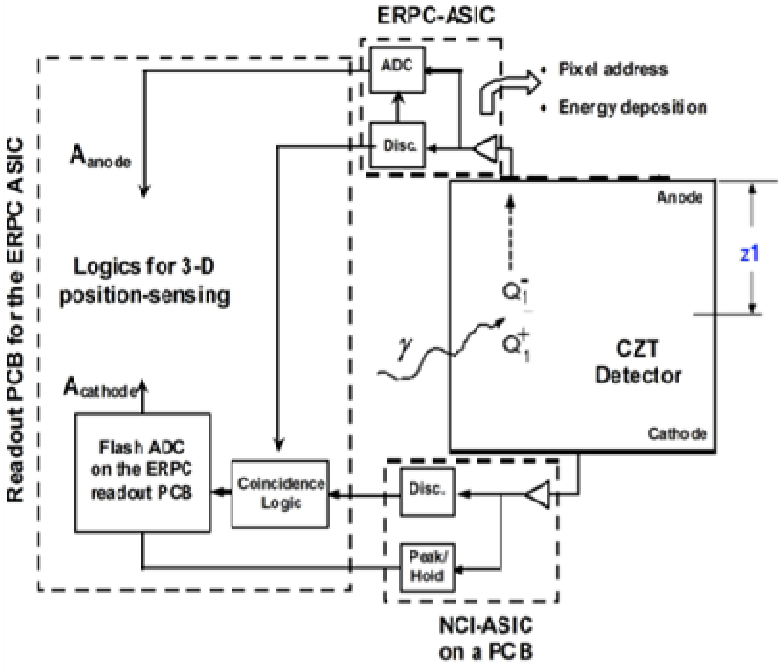

Figure 2F: Schematic of using the cathode-to-anode ratio to derive the depth-of-interaction [48].

2.2.3 Digital readout circuitry

As Figure 2G, a hybrid is wire-bonded to a digital readout PC board placed at the side of the detector. This PCB board provides power feed logic and timing signals for four ASICs, has a 32-MB data buffer for temporarily storing digital signal amplitude and pixel index. Some FPGAs on PCB control the detector readout operation, and acts as a connection between the data acquisition software and ASICs. To trigger the events, a universal threshold is set for all pixel channel, and controlled by an 8-bit DAC mounted on PCB, which allows the resolution around 0.46kev.

The power consumption of a single ASIC in active mode is around 0.8W. Each camera with a total of eight ASICs requires a maximum power consumption of around 10W. The camera is mounted onto a copper back plate, with a peltier cooling unit attached on the opposite side for heat dissipation. The digital PCBs can be connected to the host PC either through a USB 2.0 or a Camera Link interface. If placed in MRI room, cables with 10 meters in length are needed to connect detectors and PC or power supplies outside the MRI room.

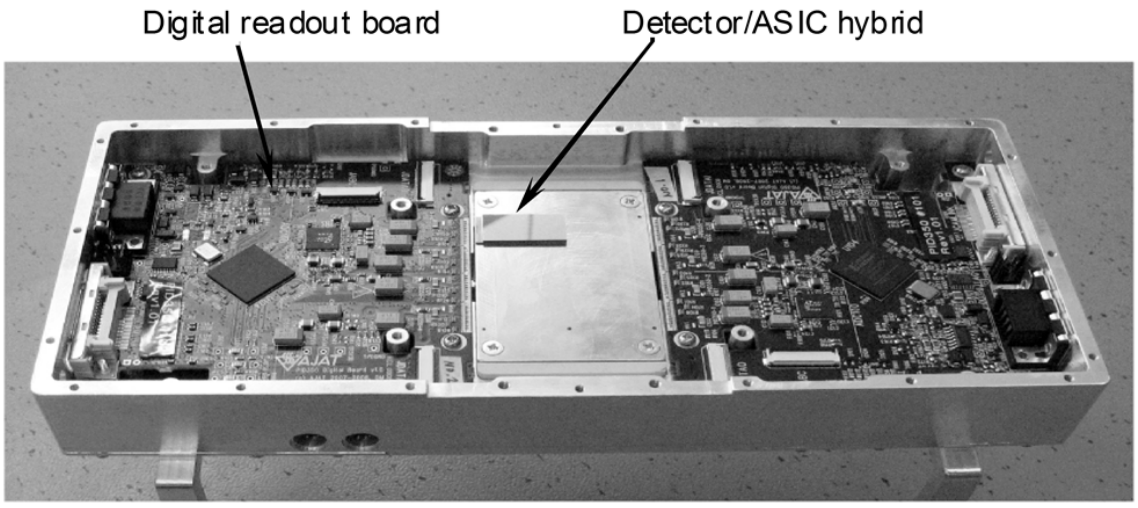

Figure 2G: The prototype ERPC detector assembly with a single hybrid attached.

2.3 Development of ERPC detectors

The ERPC detectors is developed based on a pixelated photon-counting CdTe detector, which is the earliest version of CdTe detector with the hybrid design (Chapter 2.2) in as shown in Figure 2H (MGC700T2, Ajat, Finland), This detector shares similar front-end readout electronics with the ERPC detector, which includes pre-amplifiers, shaping amplifiers, discriminators, gain and DC trimming circuitry and so on. The MGC detector also has a very similar physical configuration as the ERPC detector, which consists of multiple detector/ASIC hybrids of 1.1 cm × 2.2 cm in size. The MGC detector uses pixelated CdTe detector of 0.75 mm in thickness bump-bonded onto a CMOS photon-counting ASIC. In this study, we used a detector of 2.2 cm × 2.2 cm in size. It has 44 × 44 pixels with a pitch size of 0.5 mm × 0.5 mm.

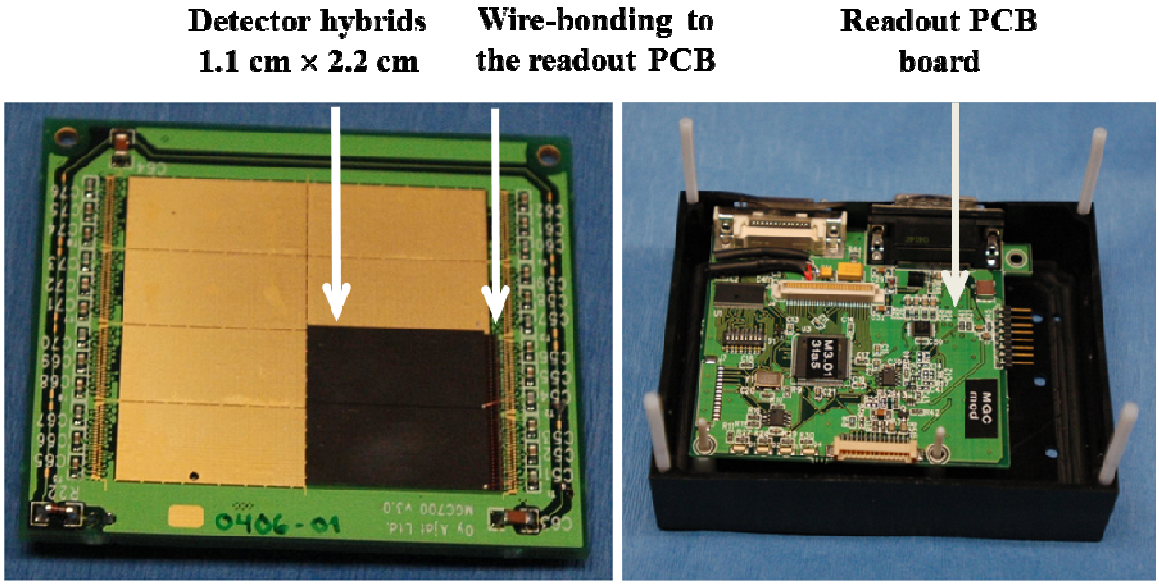

Figure 2H: (Left) MGC700T2 CdTe photon counting detector with two hybrids mounted in a copper plate; (Right): Digital readout PCB placed in a plastic box.

The first prototype of the ERPC detector (Figure 2I) has eight closed packed standard CdTe hybrids with 1mm crystal, providing total detection area 4.4cm × 4.4cm. There is wire-bonding from the crystals to the readout PCB at one edge. As shown in Figure 2I, the PCBs at the side of the detection area consist of the digital readout circuitry for handling four CdTe/ASIC hybrids.

For subsequent use in MR scanners, we have replaced some of the components of the PCBs with their non-magnetic counterparts. In addtion, we are developing the other ERPC detector with more compact design as Figure 2J. Only two hybrids are used with total detection area 2.2cm × 2.2cm for more SPECT imaging applications, which has very small dead space. Meanwhile, 2mm-5mm CdZnTe crystals (as Figure 2K and 2L) are used in different ERPC detector designed for higher energy SPECT tracers. When using the CdZnTe crystals, two different CdZnTe-ASIC bonding techniques (SnBI bump-bonding and Ag/Cu conductive epoxy bonding) are under evaluation. Similar with CdTe detector, the anode side of the CdZnTe detectors have square pixels of 350 um pitch but with smaller actual pixel contacts 250 um × 250 um in size in Figure 2M (fabricated by Creative Electron Ltd.).

Each anode pixel has a thin layer of gold (50 nm thickness) in direct contact with the CdZnTe crystal and a second layer of nickel of 100 nm on top of the gold layer. The CdZnTe detectors are connected to the ASICs through a bump-bonding process that uses SnBI solder alloy as the bonding material. This technique requires a peak temperature of 170°C, which is above the maximum temperature suggested by CdZnTe manufactures.

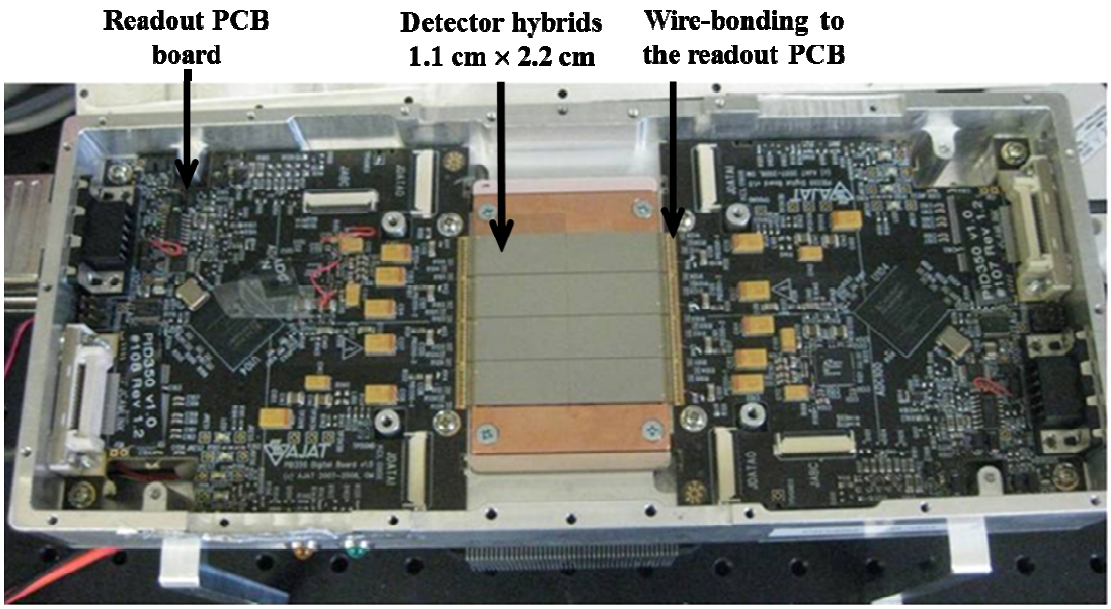

Figure 2I: The prototype ERPC detector assembly with eight hybrid attached.

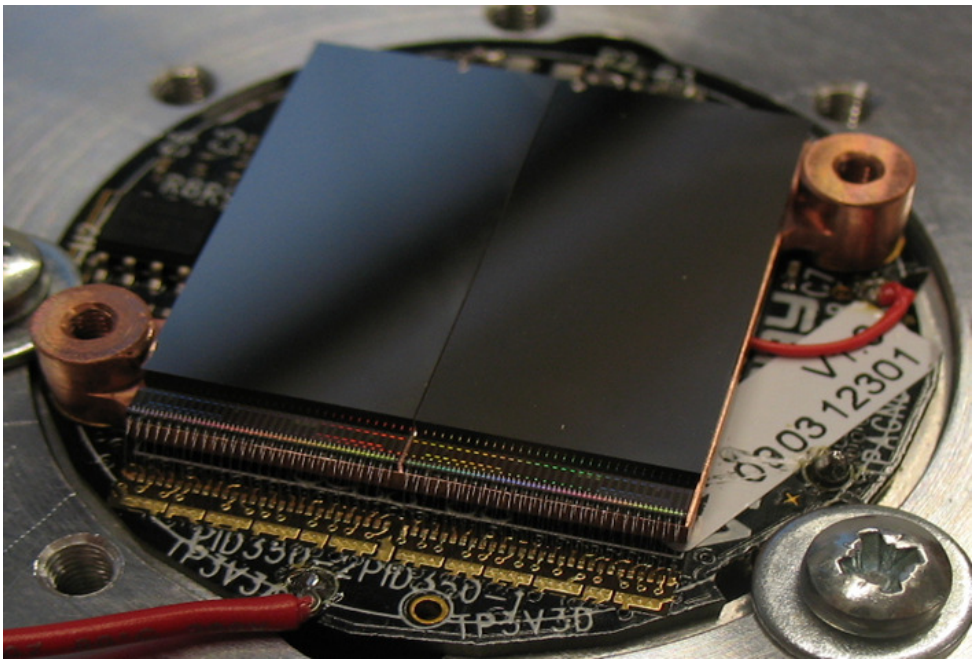

Figure 2J: Compact ERPC detectors with two standard CdTe hybrids.

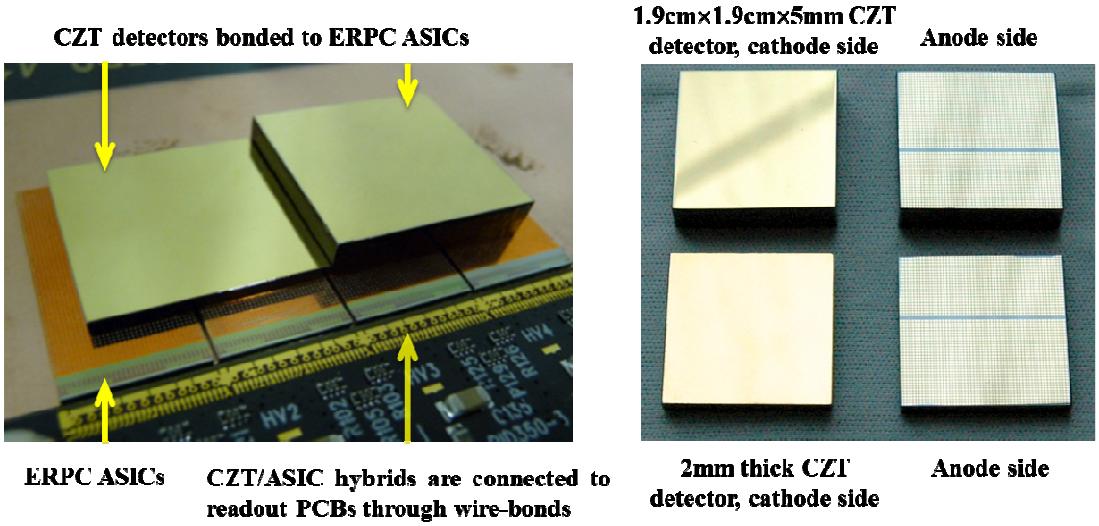

Figure 2K: ERPC detectors with 2mm and 5mm CdZnTe crystals.

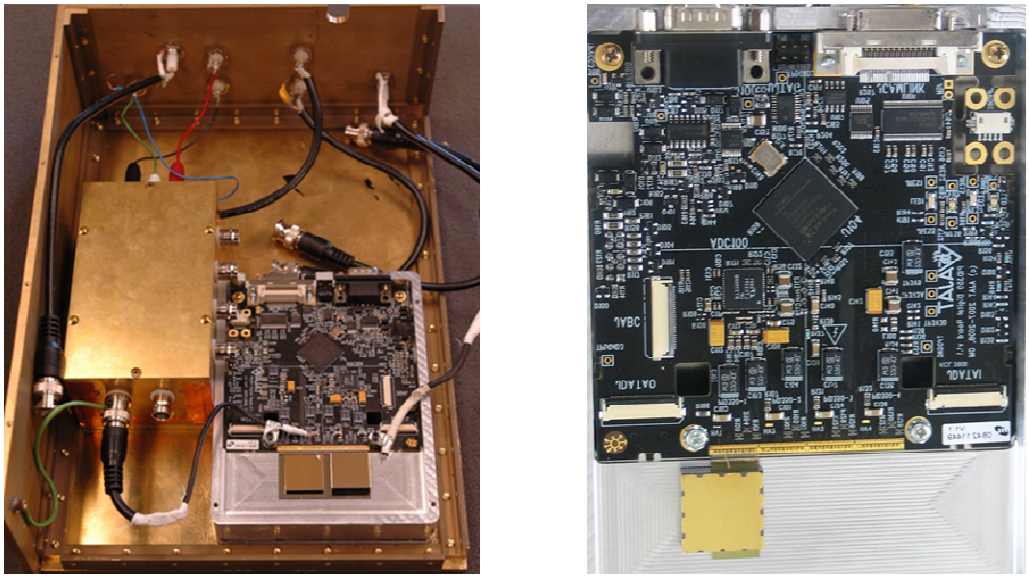

Figure 2L: Prototype of the CdZnTe ERPC detectors.

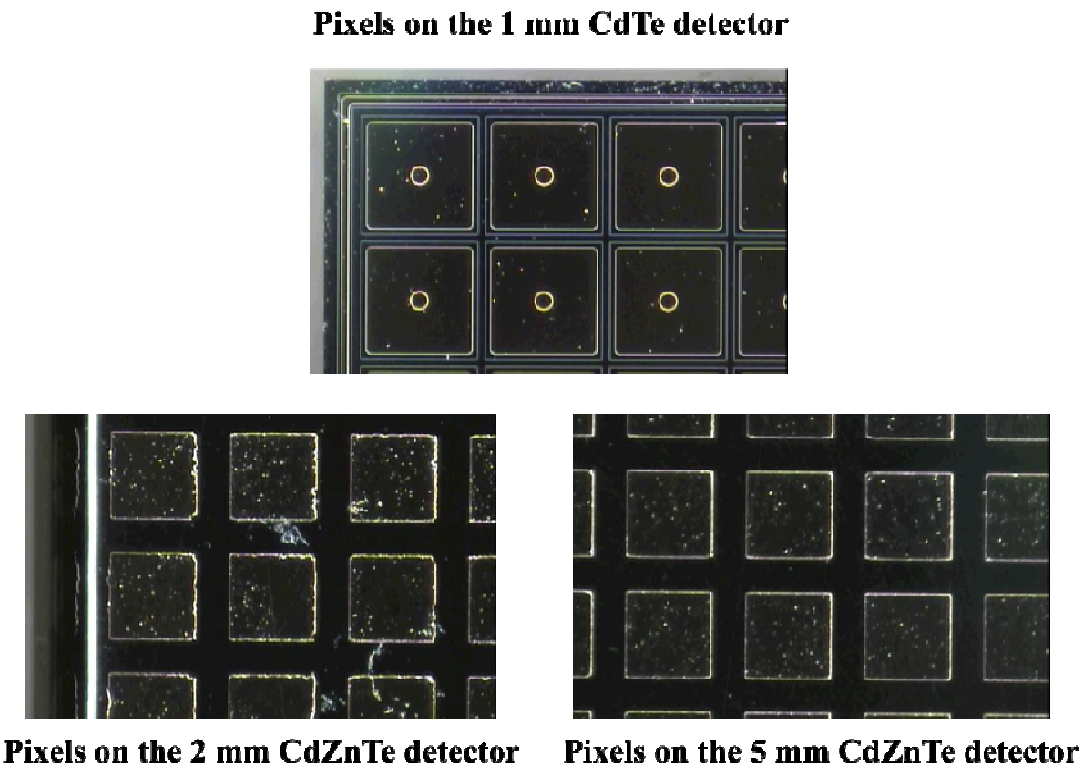

Figure 2M: Photos of 1mm CdTe pixel (anode area: 300μm×300μm), 2mm CdZnTe pixel and 5mm CdZnTe pixel (250μm×250μm).

2.4 Preliminary evaluation of ERPC detector performance

Detector uniformity is a very important aspect in evaluation of detector performance. To investigate the detector uniformity with 128×128 (CdTe) or 50×50 (CdZnTe) pixels, two open sources Co57 and Am241 are used to irradiate the entire detector. With ERPC-ASIC design, each pixel channel can generate an energy spectrum with peaks of 59.9kev for Am241 and 122kev for Co57. Those relatively positions of two peaks can help to derive the energy scale (gain and offset) and energy resolution for each working pixel. By using the 1mm- 2mm CdTe detectors and 2mm CdZnTe, energy spectra of open sources are acquired, and gain and energy resolution@122kev maps are shown in Figure 2N. The gain displayed is defined as number of ADC units per kev. As maps in Figure 2N, 1mm and 2mm CdTe detectors (128×128 pixels) has shown the appreciate distribution centered at 1ADC unit/kev, and their energy resolution@122kev (FWHM) is centered at 5-6kev. For 2mm CdZnTe detector (50×50 pixels), there is no obvious change for gain distribution but slightly larger FWHM maps with energy resolution centered @8kev. This is partially caused by larger inter-pixel gap for CdZnTe detector (100μm gap/CdZnTe and 50μm gap/CdTe with pitch size 350 μm for both), which may lead to higher possibility of gamma ray interaction in gap volume, and thus more charge loss and charge sharing among the adjacent pixels. In those ERPC detectors, roughly 1-2% CdTe pixels and 10% CdZnTe pixels do not work properly, labeled by black in the maps. This bad dead pixels are caused by the either bad connection between crystal and ASIC or the CMOS defects, but should not influence the performance for SPECT imaging with current 1-2mm CdTe detectors. With gain and offset maps, all the detector pixels can be aligned up to optimize performance of all 16384 detector pixels.

After alignment of all pixels, the measured energy spectra of single pixel and all individual pixels are shown in the Figure 2O. The single pixel can resolve the Ba-133 and Co-57 peaks with FWHMs @ 81kev and @122kev are around 2-3kev. Also the aligned energy spectrum with events detected by all pixels is shown in Figure 2O. The FWHMs of Am-241@59.9kev and Co-57@122kev peak are 5.3kev and 4.6kev, which are slightly worse than the individual pixel due to remaining misalignment among the pixels. Even with this degradation, the energy

resolution is still good enough to select the counts in photo peak window in SPECT imaging for most radioisotopes.

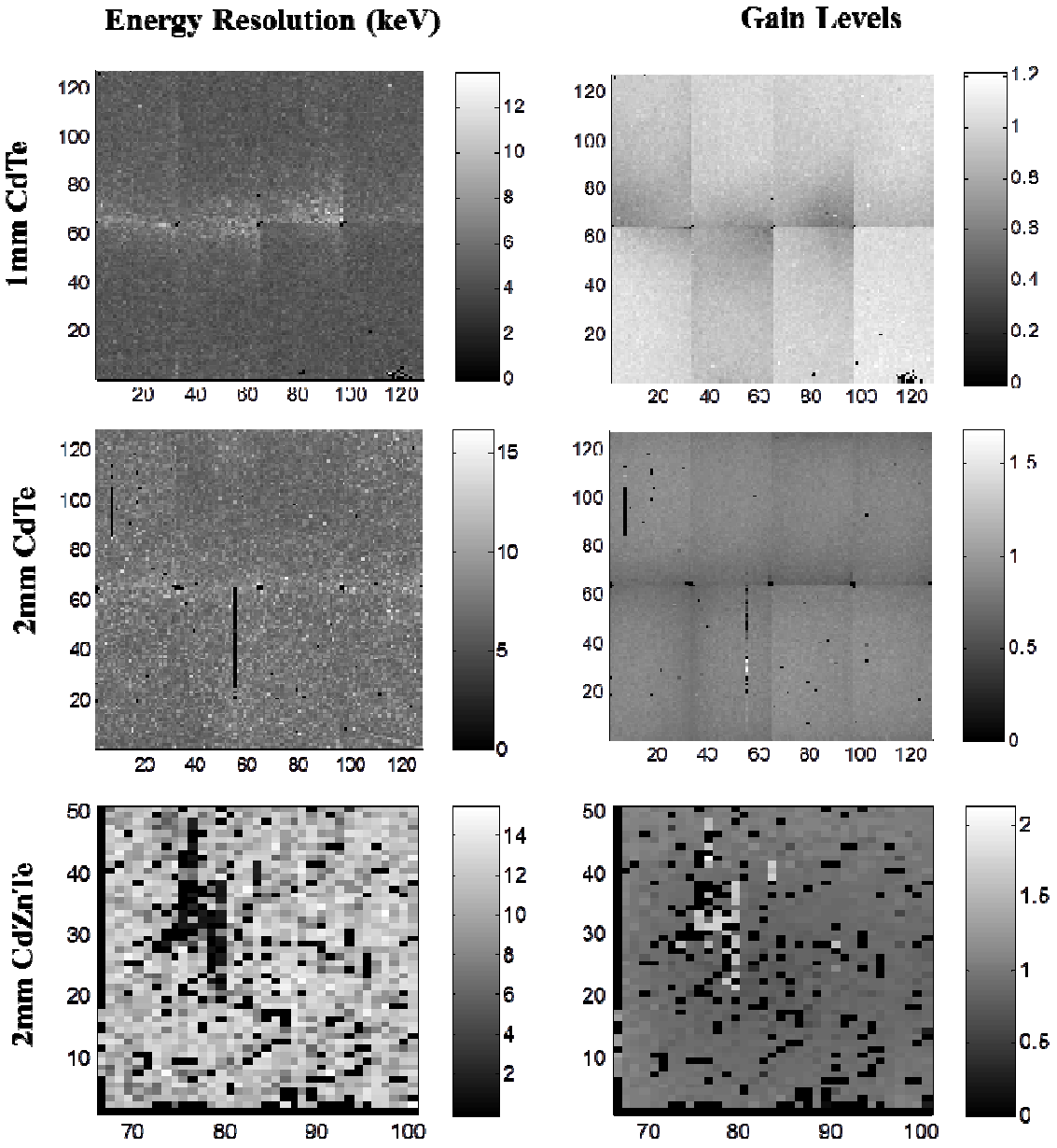

Figure 2N: Measured energy resolution and gain maps for 1mm CdTe detector (top row), 2mm CdTe detector (middle row), and 2mm CdZnTe detector.

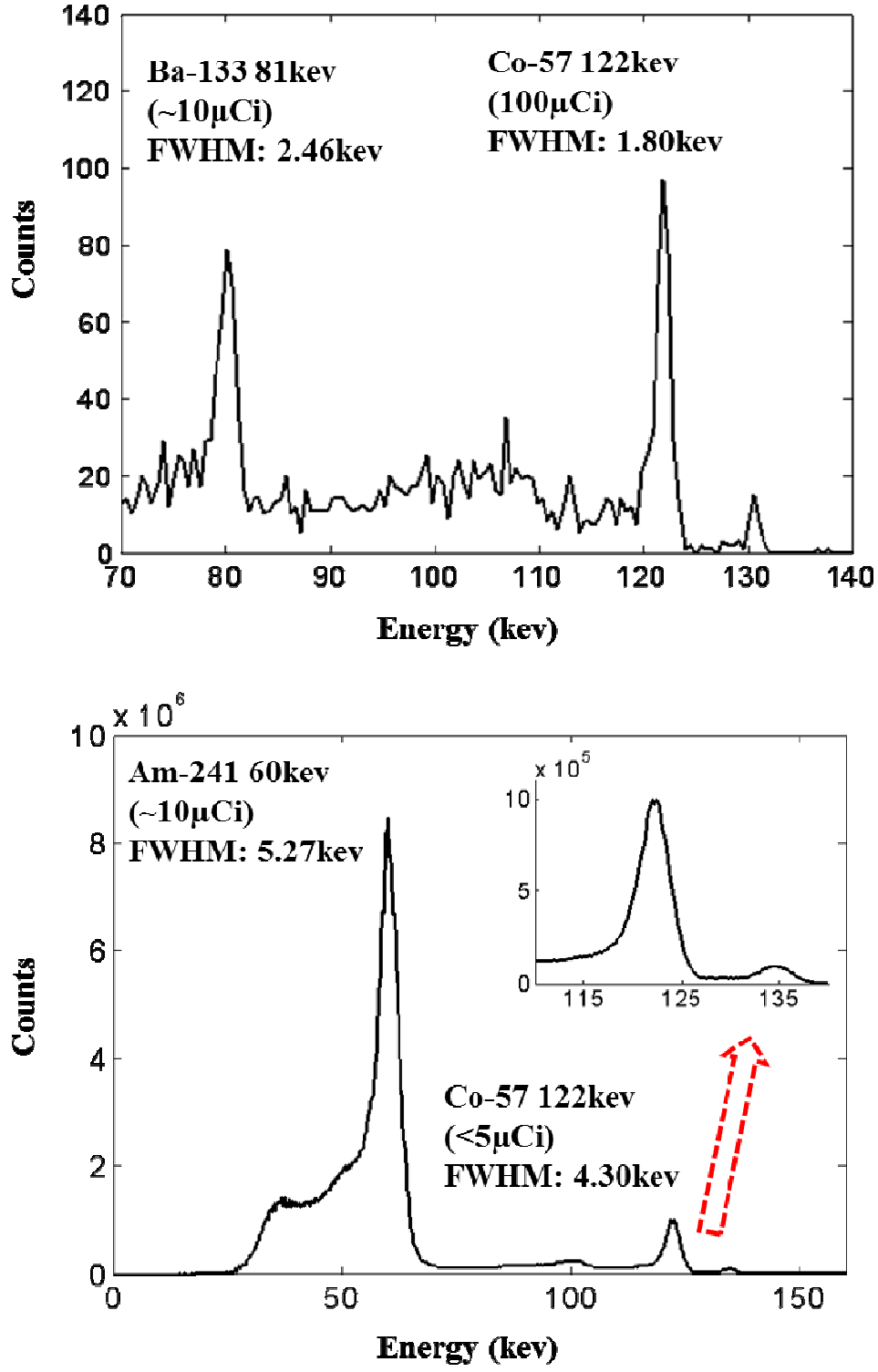

Figure 2O: Measured energy spectrum of individual pixel (top) and all detector pixels (bottom)

2.5 Summary

In the chapter, the Energy-Resolved Photon Counting detector design, the prototype of the ERPC detector with varying crystals, and preliminary performance results were presented. The detector prototype is made up of eight standard hybrids closely packed to provide 4.4cm×4.4cm detection area. Each detector hybrid module (CdTe) has array of 32 ×64 square pixels with pitch size 350μm× 350μm and anode size 300μm× 300μm. The CdTe and CdZnTe detector shared the same ASIC design, which is equipped with pre-amplifier, shaper, comparer, peak-hold circuitry discriminator and ADC. To evaluate the performance of the detector, we investigated the detector uniformity and energy resolution with the multiple open isotopes, and 4-5 kev energy resolution @122kev has been proved experimentally. This energy resolution and the intrinsic spatial resolution (350 μm) allow the multiple low energy SPECT tracers, such as I-123, Tl-201 and Tc-99. The design of ERPC detector allows the varying detection area by using standard detector modules, which can be tailored in multiple compact SPECT system for small animal studies.

Although, the prototype of the ERPC detector has exhibited promising performance for gamma ray imaging, there are several keys for further improvements. Firstly, as shown in Figure 2N, small amount of pixels do not work due to some manufacture process, especially the CdZnTe detector with larger inter-pixel gap size. We are still investigating the possible causes and solutions for the bad pixels to change the uniformity of all pixels in detector. Secondly, the current housing of the detector prototype is relatively large, because two digital PCBs are placed at both sides of crystals. The setup make the overall size of the detector housing is much larger than the detector modules (4.4cm×4.4cm) as Figure 2I. We are developing next generation detector with digital readout placed on the backside of the detector modules, which reduces the overall size of the detector housing. Thirdly, depth-of-interaction (DOI) can be derived based on the cathode and anode signals. In the future detector design, the DOI information needs to be considered and implemented to provide 3D positions of events. With DOI information, the SPECT imaging response function could be refined to achieve the better spatial resolution, and this improvement is more obvious when operated in strong magnetic field. In the chapter 4, some

mouse brain phantom simulation with DOI outside and inside 3T magnetic field will be presented.

CHAPTER 3
FEASIBILITY OF USING PIXELIZED ERPC DETECTOR UNDER STRONG MAGNETIC FIELD

In this chapter, we present a preliminary study based on a prototype MRI-compatible, ultra-high resolution SPECT system for use in a pre-existing Siemens 3.0 T MR scanner. The system uses an ultra-high spatial resolution energy-resolved photon-counting (ERPC) CdTe detector that we have recently developed. This detector consists of eight hybrids, each having a pixilated CdTe detector of 1mm thickness, bump-bonded to a custom-designed CMOS readout ASIC. Each detector hybrid offers an imaging area of 1.1cm × 2.2cm that is divided into an array of 32 × 64 pixels with a pitch size of 350μm × 350μm. The prototype SPECT system has been designed and tailored for use inside the 3.0 T Siemens scanner for tomographic imaging. It consists of a single ERPC detector head coupled to a collimation aperture, which is installed inside a non-magnetic gantry. This non-magnetic gantry allows the detection system to be moved in and out the Siemens scanner and to be rotated around the object for obtaining a sufficient angular sampling supports the detector. In this prototype, all shielding, supporting and cooling structures are proved to be MRI-compatible. The following text starts from discussion of MRI-compatibility of detector and other major SPECT components in 4.7T MRI scanner, and then the imaging performance with presence of magnetic field and spectroscopic performance will be evaluated by using point source.

3.1 MRI-compatibility of CdTe detector and other major SPECT components

Before carrying out SPECT imaging studies inside the MRI scanner, we have firstly assessed

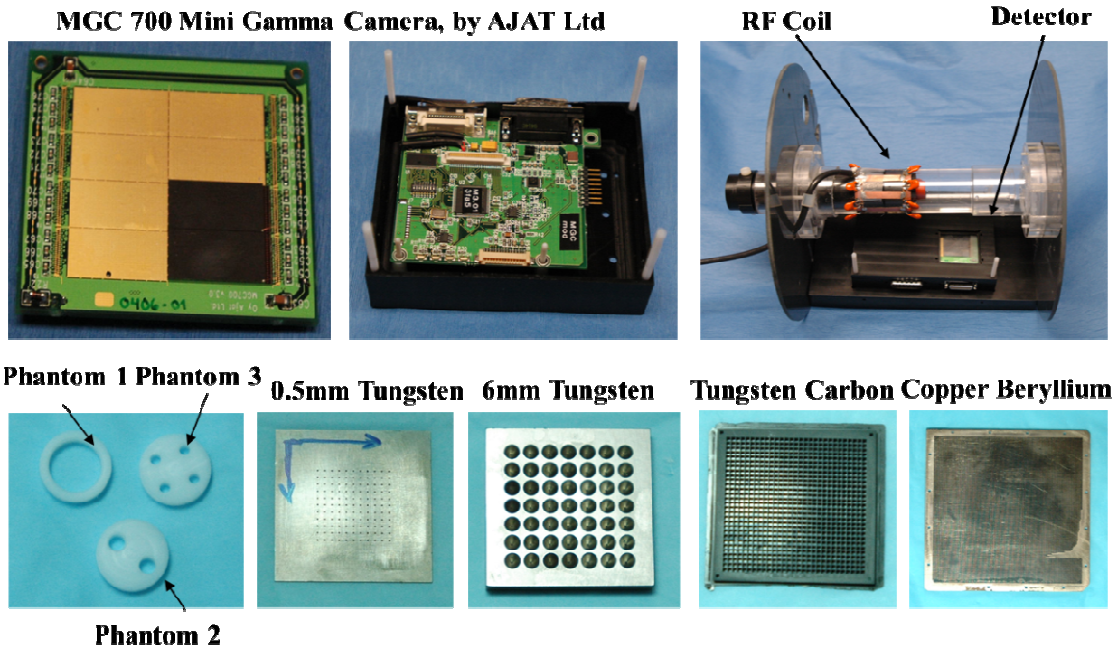

Figure 3A: (Left): The CdTe photon-counting detector used in the experimental study. It consists of two CdTe/ASIC hybrids, as detailed in Section II.B. (Right): The system gantry used in this study, which supports the RF coil, the cylindrical phantom, the CdTe detector and the SPECT collimators inside the MRI system. (Bottom): MRI phantom insert 1, 2 and 3, and several collimator candidates in SPECT system.

TABLE 3A: Parameter of 4.7T MRI scanner

Magnetic field	4.7 T
Relaxation time	T1=150 ms
ID of RF coil	3 cm
ID of scanner bore	22 cm
Maximum gradient	65mT/m at 200 T and 100A
Repetition time	TR=600 ms
Echo time	TE=20 ms
Number of transients/averages	NT=2
Spectral width	SW=25 kHz
Field of view	FOV=2.0×2.0 cm^2
Matrix size	256×128
In-plain resolution	78×156 μm^2
Slice thickness	1.0 mm (no gap)
Number of slice	12
Acquisition time	2.35 min
Phantom solution	3mM Cu_2SO_4

the impact of SPECT components on MRI image quality. To evaluate MRI imaging performance with the presence of the SPECT detector and collimator materials (as Table 3B and Figure 3A), we used a test phantom that contains three cylindrical inserts (1.3 cm in diameter and 3 mm in thickness). 10mm 3mm and 2mm cylindrical holes are drilled through the inserts as shown in Figure 3A. These inserts are placed inside a glass tube filled with 3mM Cu2SO4 water solution. The MRI scanner has a horizontal bore of ~20cm diameter. It is operated at room temperature with field strength of 4.7 T at the center of the scanner. The gradient coils are driven by a set of Varian amplifiers, which can be created up to 65 mT/m at 200V and 100A with rise time 15μs. During MRI imaging, spin-echo multi-slice pulse sequences are applied for MR image acquisition. Table 3A lists some specific MRI parameters used in this study. MR images of the phantom (Figure 3B) are compared based on their visual appearances, signal-to-noise ratio (SNR) and image uniformity.

Different collimator candidates (listed in Table. 3B) for SPECT imaging are evaluated by manually placing them in a collimator holder coupled to the CdTe detector. Note that with this manual process, the relative position of phantom may vary with different collimator materials. The SNR is one important parameter used to evaluate MR image quality, which is defined as the ratio between the signal amplitude at a given pixel and the standard deviation across multiple pixels in the background region as shown in Figure 3C and 3D. By comparing those MR images, most of the materials for collimators yield similar image SNRs for Phantoms 1, 2 and 3. The only exception is the aperture made of a single piece tungsten alloy (Figure 3A) that consists of a small amount of ferromagnetic materials (2.1%Ni and 0.9%Fe), but the use of lead and thin sheets of pure tungsten in the 4.7T magnets did not produce a severe distortion. Therefore, stacking multiple layers of these tungsten sheets or lead collimator would provide an adequate stopping power without introducing severe distortion in MR images. This offers a practical solution for the proposed SPECT system in strong magnetic field.

TABLE 3B: Detector components and collimator materials tested inside the MRI system

SPECT Components Tested (Material No #)	Dimension	Description	Material Ingredient
CdTe detector (1)	22×22×0.75mm^3	Two modules packed	
CdTe detector with copper foil (2)	Foil: 200μm thick; CdTe:22×22×0.75mm^3	Two modules packed CdTe detector Detector was shielded by 200μm foil	
Tungsten (W) (3)	35×35×0.5 mm^3	Single piece	Pure Tungsten 99.9%
Tungsten (W) (4)	35×35×0.5 mm^3	A stack of six piece	Pure Tungsten 99.9%
Lead (Pb) (5)	35×35×3mm^3	Single piece	Pure Lead
Lead (Pb) (6)	35×35×3mm^3	A Stack of two piece	Pure Lead
Lead block stack (7)	5×5×3mm^3 for each block	Multi-layer lead stack; Non-contacted blocks	Pure Lead
Tungsten Carbide (8)	40×40×2mm^3	Parallel hole aperture	N/A
Copper Beryllium (9)	80×80×2mm^3	Parallel hole aperture	N/A
Tungsten (10)	35×35×6mm^3	Single piece multi-pinhole aperture	18.5g/cc,97%W,2.1%Ni, 0.9%Fe

In this MRI imaging studies, a CdTe photon-counting detector is placed inside a plastic box with copper foil of 200 μm thick wrapped around as an electric shielding, which is attached outside RF coil, a high-pass “birdcage” transmitter/receiver RF coil. The RF coil has an inner diameter of 3.2 cm and an outer diameter of 3.6 cm. Any MRI phantom in a glass tube is supported at the center of the RF coil (as Figure 3A).

This study also demonstrates that the presence of the CdTe photon counting detector and the copper shielding would not lead to a noticeable distortion in MR images. Given the similarity between the CdTe photon counting detector used in this study and the Energy-Resolved Photon Counting (ERPC) CdTe detector (different ASIC) used in the SPECT system, we concluded that

the EPRC detector is able to work inside the MR scanner without significant degradation in MR image quality.

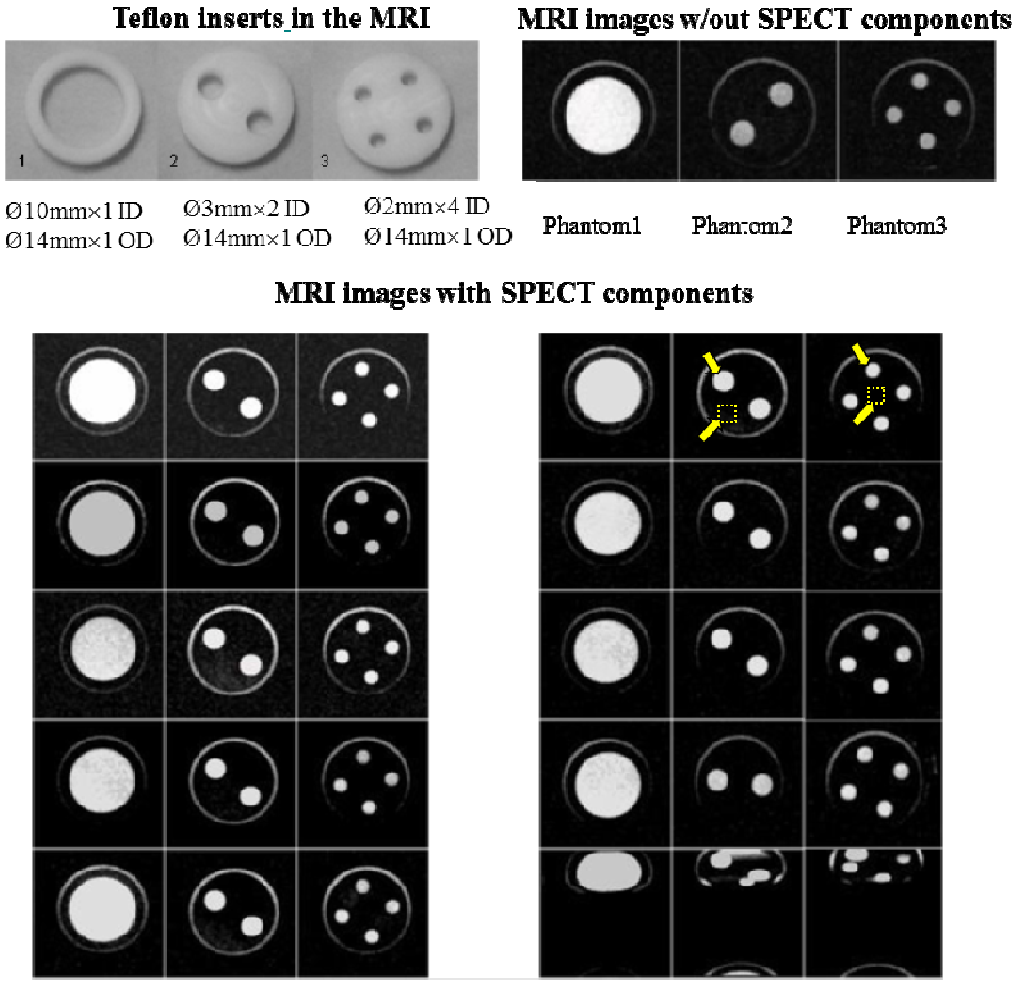

Figure 3B: MRI images of the phantom with the presence of different SPECT components. Left column: (from top to bottom) CdTe detector only, CdTe detector and copper shielding foil, single piece of tungsten(0.5mm in thickness), a stack of six tungsten pieces, single piece of Lead (3mm in thickness); Right column: 6 mm thick lead (made of two layers of lead sheets);multilayer lead block; tungsten carbide parallel-hole aperture (2mm thick);parallel-hole aperture made of copper beryllium (2mm in thickness), 6mm thick tungsten piece. The arrows in the figure indicate the point and area that were selected for the calculation of the SNR in MR images.

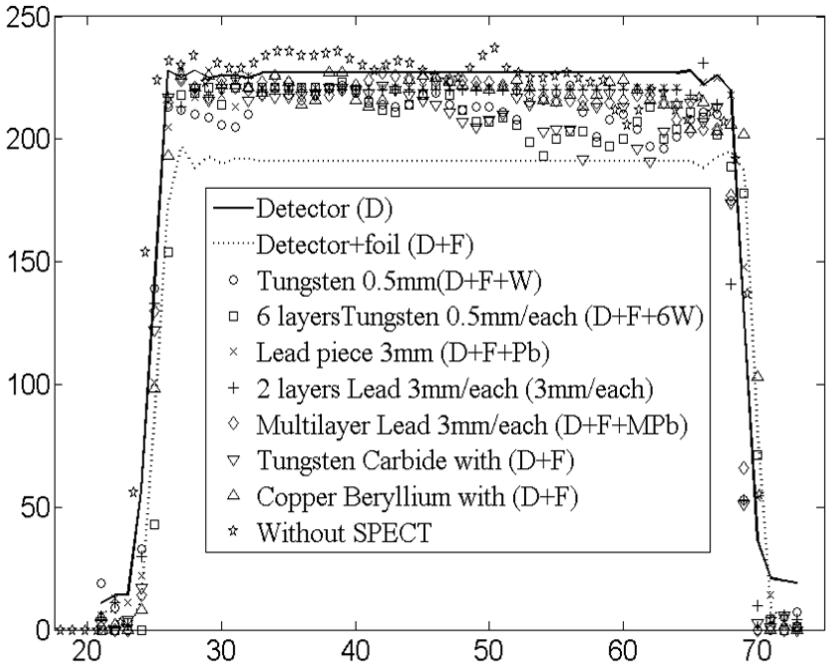

Figure 3C: Cross sectional view of the insert Phantom1 with the presence of different SPECT components

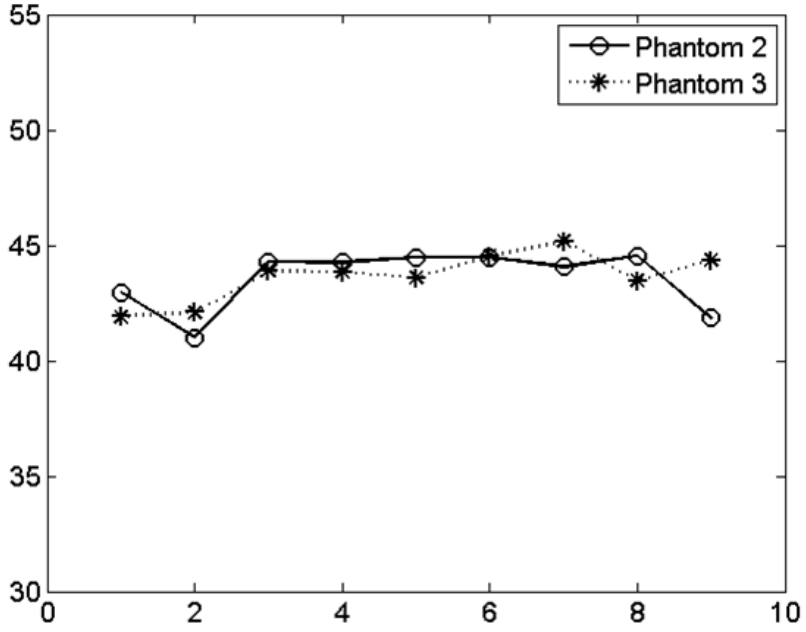

Figure 3D: SNR of the MRI images shown in Figure 3B. Materials #1-9 are corresponding to the first nine entries in Table 3A.

3.2 Spectroscopic performance of ERPC detector outside and inside strong magnetic field

To evaluate the energy performance ad charge sharing of the pixelized ERPC detector, we used flood source and pencil beam gamma ray source to irradiate either selected small region (in anode area or inter-pixel gap area) or the whole detector area. The pencil beam source is created by an experimental setup (as shown in Figure 3E). In this setup, a "parallel" gamma ray beam (Co57) is used to scan and irradiate the pixels of detector from various angles. The collimator we used is made of a stack of finely machined tungsten blocks of 500μm × 600 μm × 12mm in size. It leaves a square hole of 100 μm × 100 μm ×12mm as shown in Figure 3E. The collimator/source assembly is placed closed to the surface of the detector, and positioned by a high precision non-magnetic 2-D linear stage and a goniometer. This setup allows the collimated gamma ray beam to irradiate various regions of detector with various incident angles.

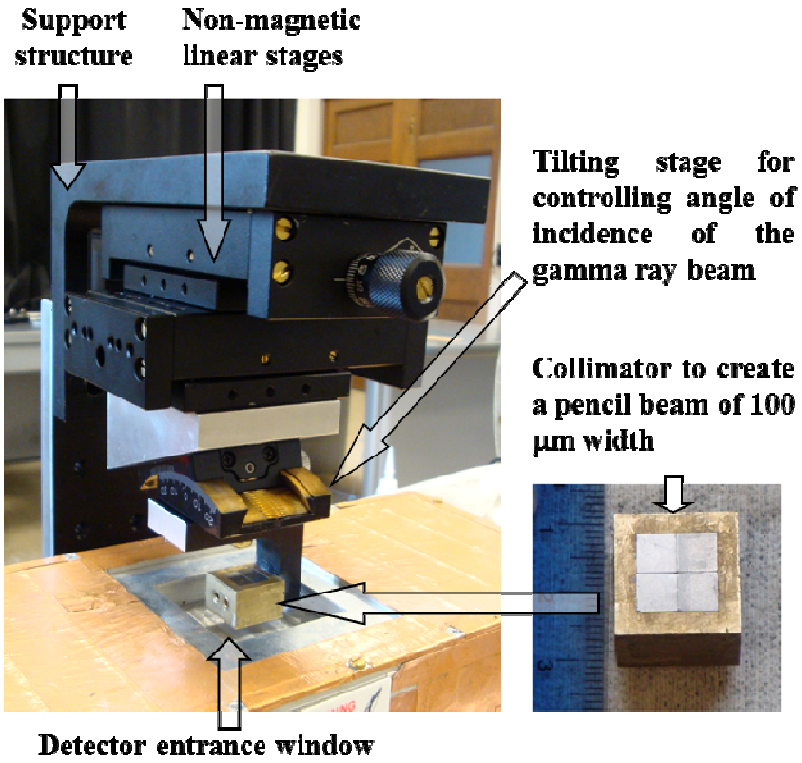

Figure 3E: Experimental setup to create a gamma ray pencil beam (Co57)

By using this pencil beam, we scanned pixels of detector to form events located at different region and depth of single pixel. The energy spectra measured on a single pixel with events at different depth of interaction and different sub-pixel locations (from center of the pixel to the center of the inter-pixel gap) are shown in Figure 3F and 3G. The measured energy resolution of individual pixels could reach 3-4kev, but it increases as beam transported from center of pixel to inter-pixel gap due to charge sharing and charge loss.

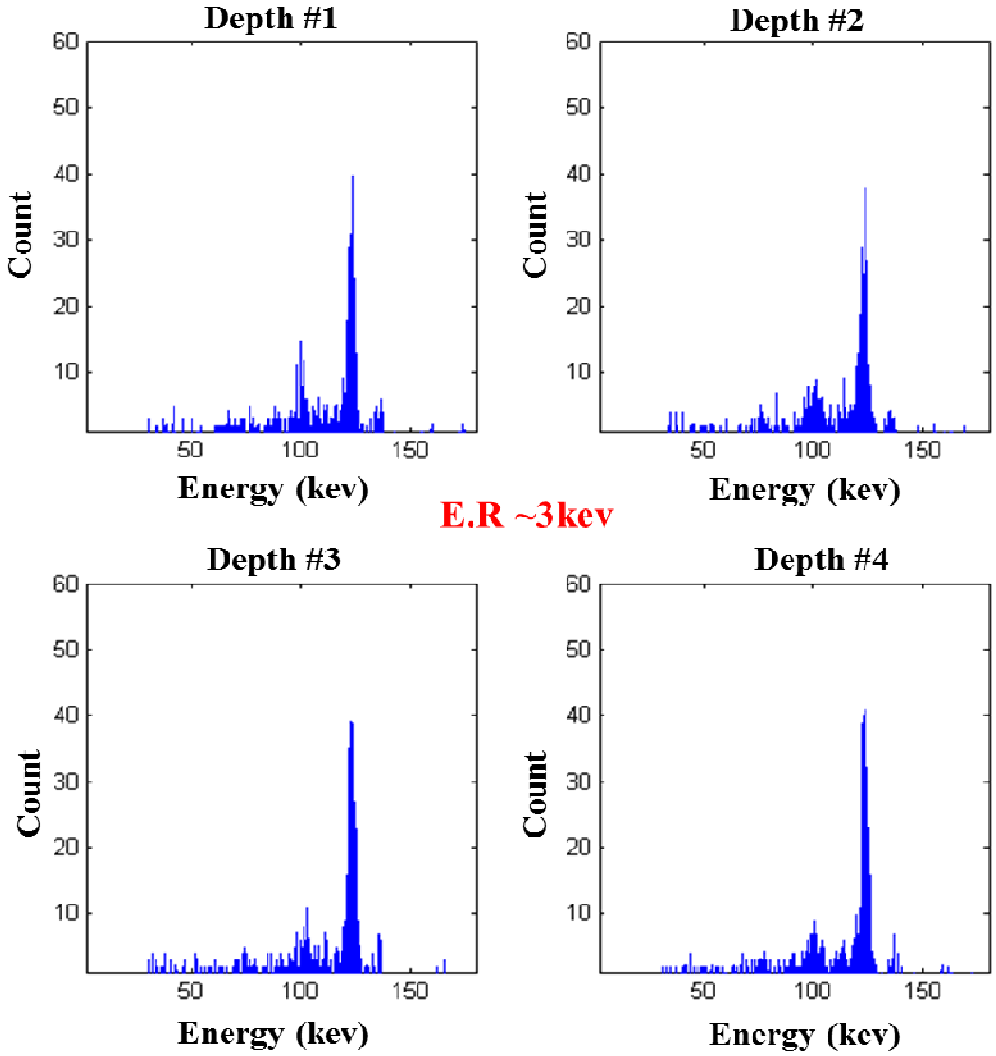

Figure 3F: Energy spectra measured on a single pixel with events at different depths-of-interaction.

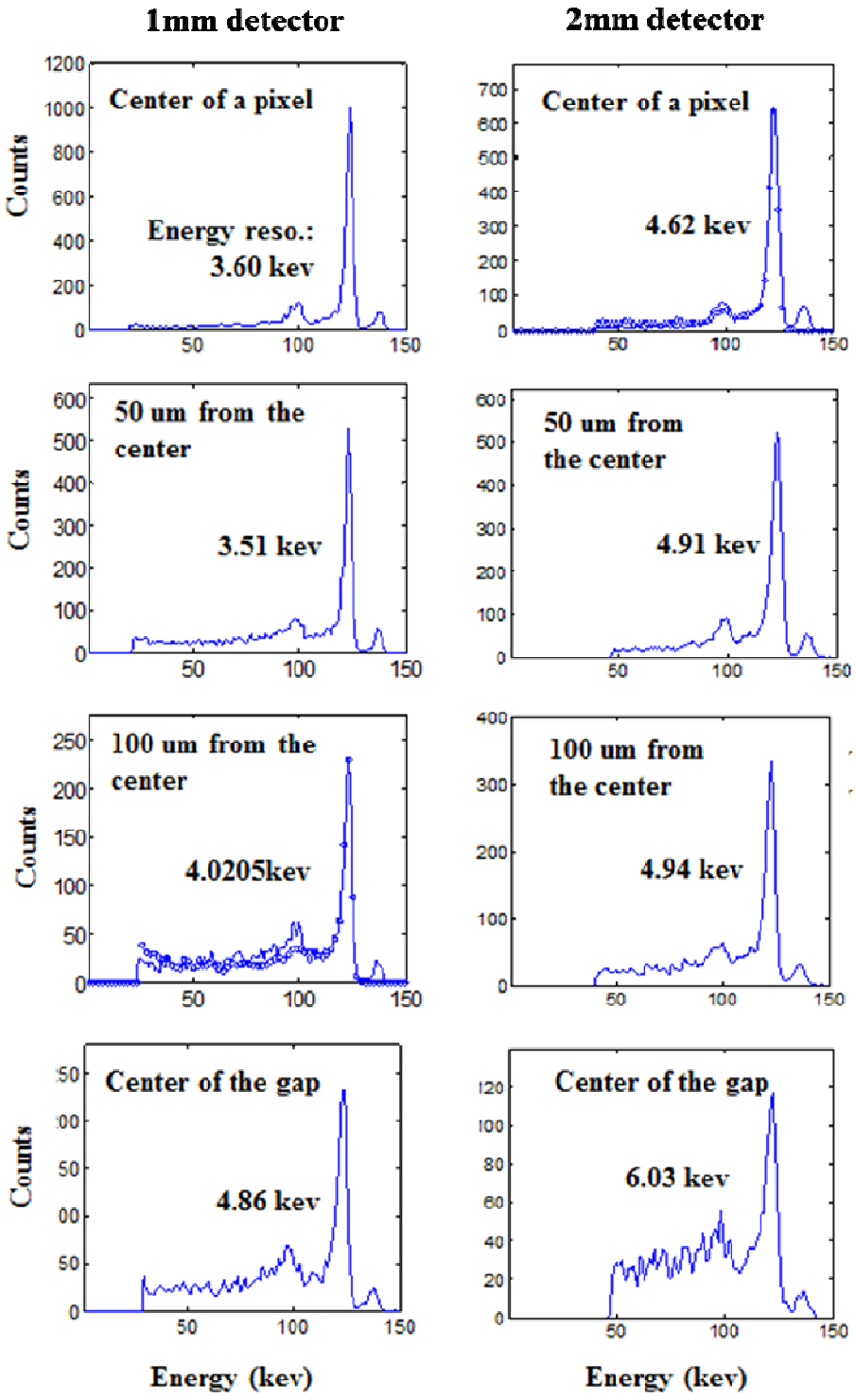

Figure 3G: Energy spectra measured in single pixel of 1mm and 2mm with incident beam at multiple locations from center of the pixel to center of the inter-pixel gap. The energy resolution was ranging from 3 to 6kev.

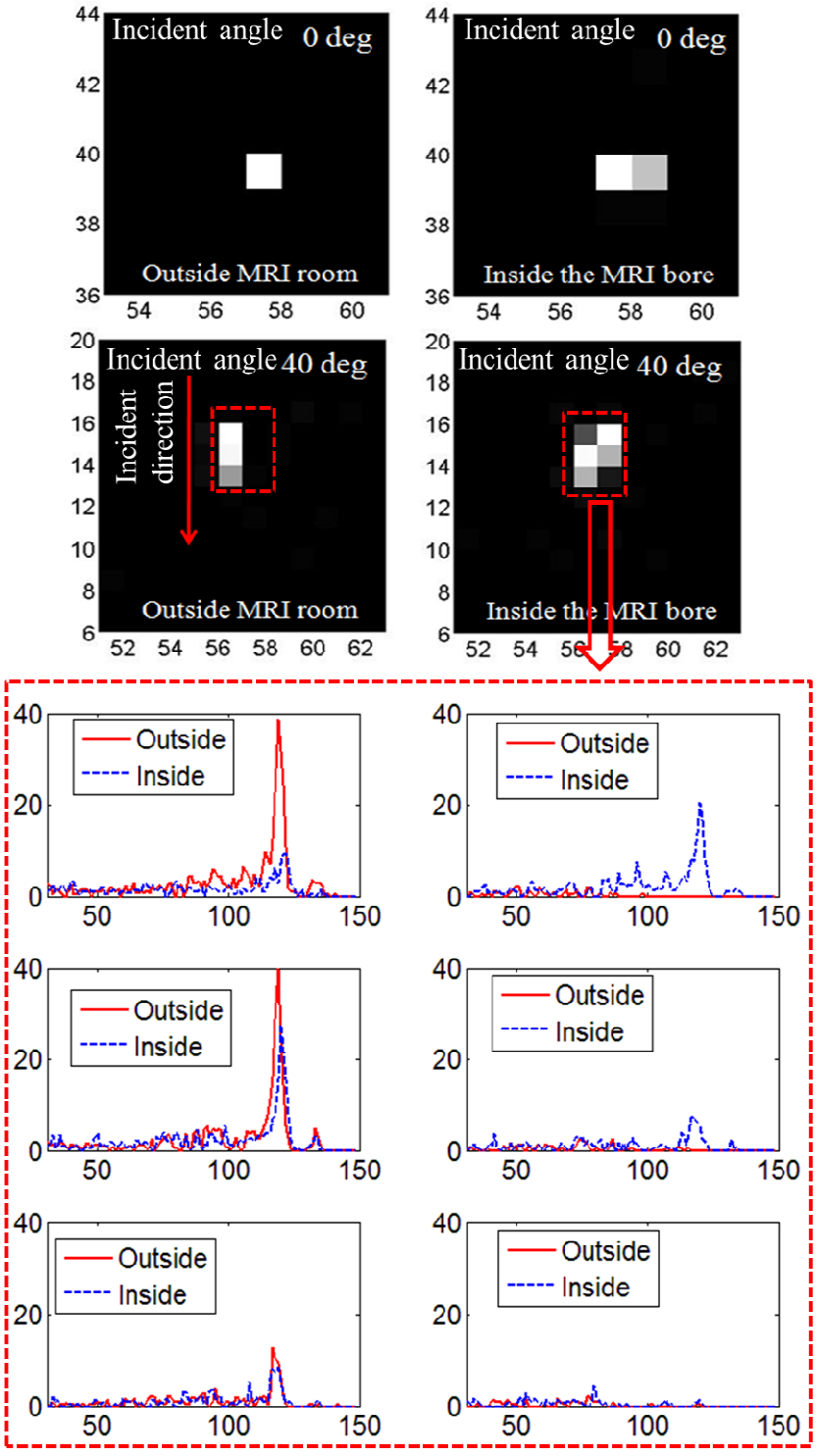

Figure 3H: (Top) Projections of collimated source Co57 at incident angle 0 deg and 40 deg inside and outside the MRI scanner. (Bottom): Energy spectra of group of pixels in projections acquired inside and outside MRI magnetic field.

In this study, we also investigated the effect of strong magnetic field on ERPC detector using the experimental setup shown in Figure. 3.E. A pencil beam is used to irradiate multiple pixels on the ERPC detector operated inside and outside the MR scanner. With the 0 and 40 degree incident angle, the projections and the pixel energy spectra of experimental results obtained with the 100μm × 100μm pencil-beam collimator are shown in Figure 3H. Clearly, the amplitude of shift depends on the depth-of-interaction, and thus the events interact near the cathode have much higher probability to drift to and be collected by the neighbor pixel than the events interacted near the anode. The detailed charge collection process with effect of magnetic field is discussed in chapter 4. We also used flood sources (Am-241 10μCi, and Co-57 5μCi) to irradiate the whole detector area (16384 pixels) operated outside and inside the pre-existing 4.7T MR scanner.

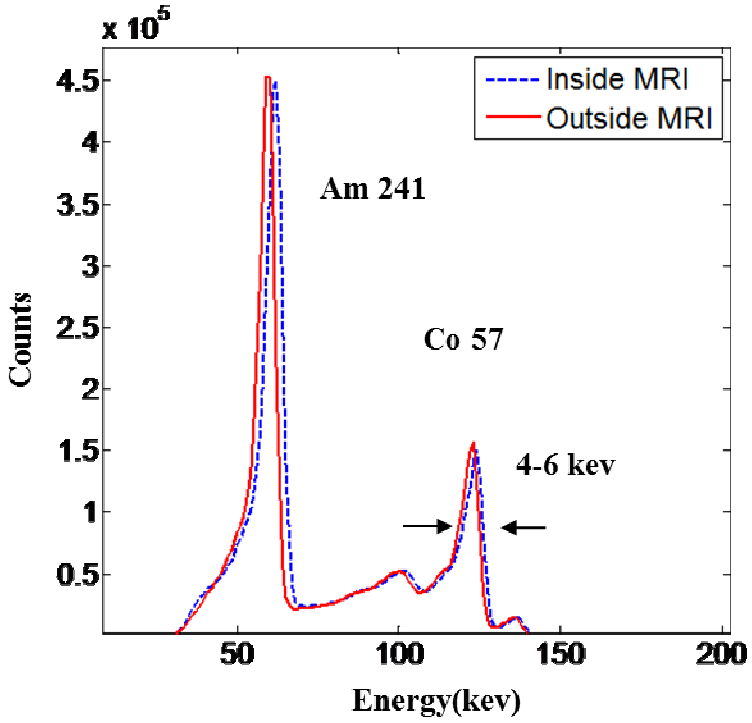

Figure 3I: Energy spectrum of single detector module acquired inside and outside MRI magnetic field.

The obtained energy spectrum of each pixel was aligned, and the energy spectrum of all detector pixels is shown in Figure 3I. With and without magnetic field, the two energy spectra have the same shape and energy resolution was measured to be around 4-6kev for both situations (as

Figure 3I). There is no significant effect on spectral response with presence of magnetic field. This leads to possibility of accurate analysis of charge sharing of multiply-pixel events with effect of magnetic field. The functionality of the ERPC detector based SPECT system is confirmed by the point source images obtained inside the MRI scanner, which will be discussed in chapter 3.4.

3.3 Design of the MRI-compatible SPECT system

After confirming the MRI-compatibility of major SPECT components, we have recently proposed a very high spatial resolution SPECT system that can be placed inside a pre-existing Siemens 3.0T MRI system (Figure 3J). The schematic of the designed system is shown in Figure 3J. The MRI scanner has a horizontal bore with inner diameter around 28cm. It is operated at room temperature with the field strength of 3.0T at the center of the scanner. The proposed SPECT system consists of 4 ERPC detectors (as shown in Figure 3K) arranged in rotating or stationary ring configuration coupled with multiple pinhole collimators. Total apertures are wrapped around the Ø3.5cm RF coil, and the object could be held in a tube supported inside the RF coil. The detailed design parameters of the combined system are shown in Figure 3J and Table 3C. ERPC detectors used in system have 1mm and 2mm thick CdTe crystals, which are described in chapter 2. The photos of 4.7T and 3.0T pre-existing MRI scanners are shown in Figure 3L.

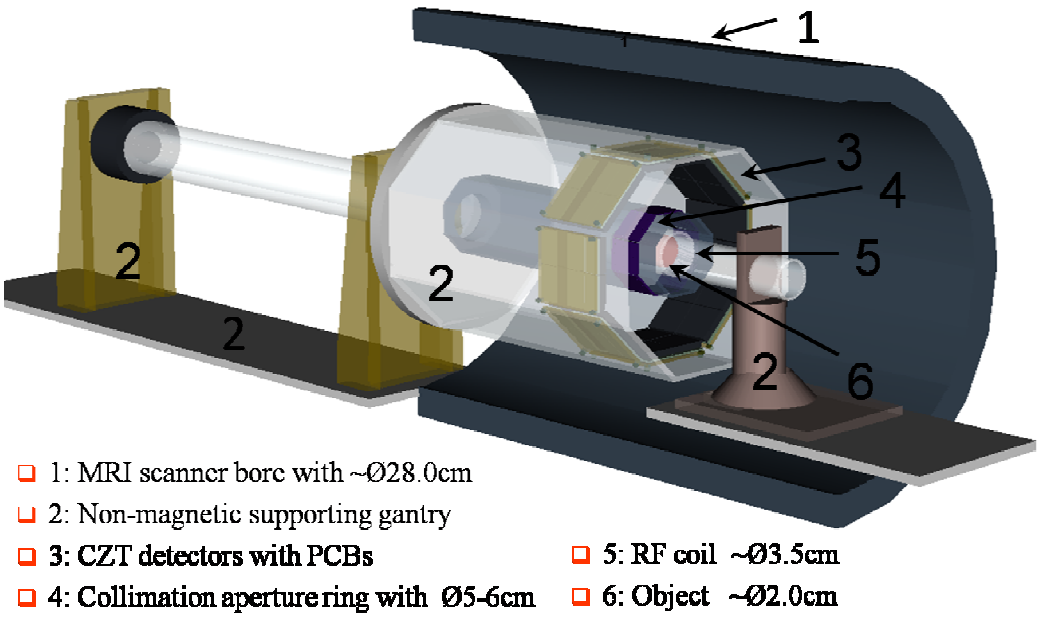

Figure 3J: Schematic diagram of the proposed SPECT/MRI system, with components as labeled. The support gantry has maximum O.D. 18cm. The cables and air pipes run through the tube.

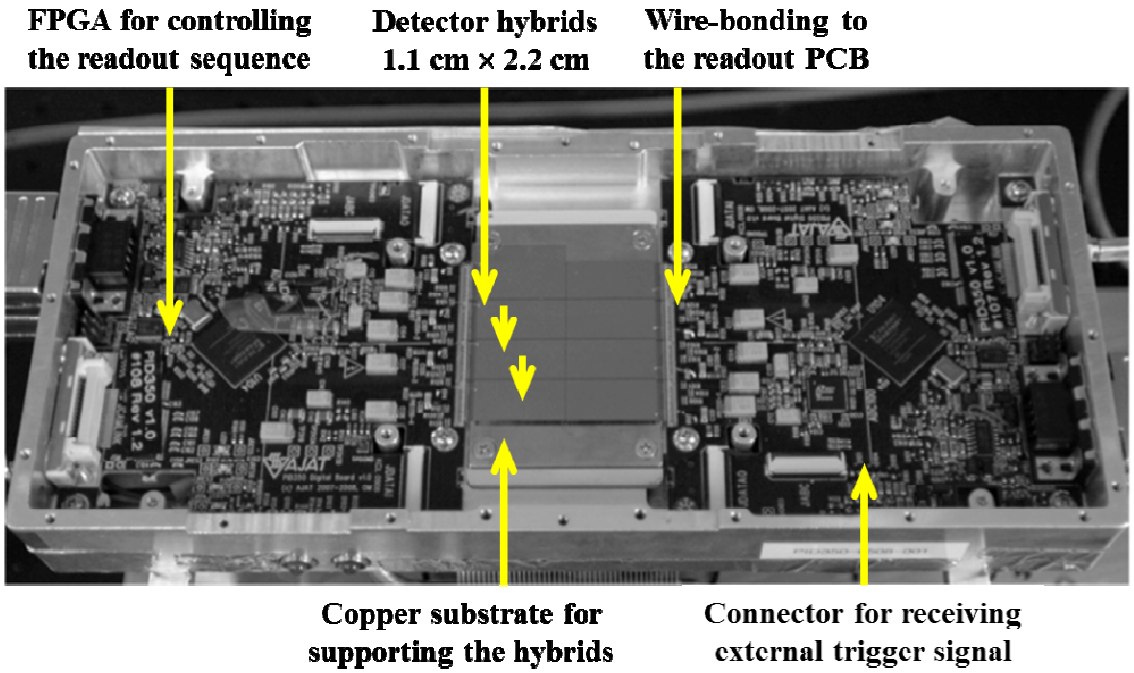

Figure 3K: ERPC detector with eight closed packed detector hybrids providing 4.4 ×4.4cm detection area.

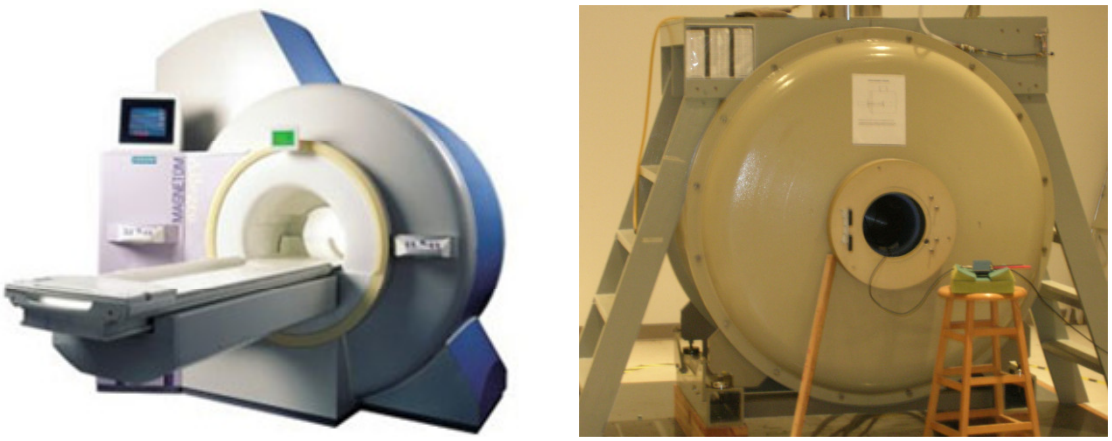

Figure 3L: A photo of the Siemens Allegra 3 T and 4.7T MRI scanner located at UIUC campus.

TABLE 3C: Design parameters of the MR compatible SPECT

Geometry parameters	**Parameter Values**
Object-to-aperture distance	~3.0 cm
Aperture-to-detector distance	~3.0cm
No.of pinhole/Aperture.	5×5; 3 × 3
Pinhole size	Ø200μm -- Ø400μm
Pinhole accept angle	30°;80°
Number of Detectors	8 (stationary)
Detector size	4.4cm ×4.4cm
Detector thickness	2-4mm
Expected image. Resolution	<500μm

3.4 A prototype of the MRI-compatible SPECT system based on a single ERPC detector

With the proved MRI-compatible ERPC detector, we built a prototype of the MRI- compatible SPECT system based on single ERPC pixelized CdTe detector. In this system, we made a supporting gantry by using non-magnetic materials such as Plexiglas, Brass and Aluminum (in Figure 3M) to hold detector and collimator. This non-magnetic gantry allows the system to be

translated in and out the scanner and rotated around the object to obtain a sufficient angular sampling by a non-magnetic manual rotation stage. As shown in Figure 3M, the cooling of the detector is achieved by blowing compressed air onto a copper heat sink attached to the detector. All the power supplies and other electric devices for detector and data acquisition are placed outside the MRI room and connected to the detector by cables of more than ten meters in length.

The proposed pinhole collimator used in our design is made by stacking multiple layers of tungsten pieces that is proved to be MRI-compatible in chapter 3.1. We made a nine-layer tungsten collimator with single tungsten piece of 3.5cm × 3.5cm× 0.5mm in size (in Figure 3M). The size of pinholes is defined 200 μm with an open angle of 80 degrees on both sides, and the pinhole distance is 5mm. In the following preliminary imaging study, we also used another one-layer Lead collimator of 3.5 cm × 3.5 cm× 6 mm in size, with 3 × 3 tungsten pinhole inserts of 400μm diameter. The average pinhole distance is 7 mm. In this experimental setup, a single ERPC detector for tomographic imaging a phantom is implemented without magnetic field. The phantom contains Co-57 sources, 100μCi sphere source and 100μCi cylinder source inserted into a water-filled glass tube, as Figure 3N.

In this SPECT imaging study, the ERPC CdTe detector is rotated manually around the object at eight steps of 22.5 degree apart, and the rotation axis is parallel to the axis of MRI scanner. The object-to-aperture and detector-to-aperture distances are both 32 cm. to form the field-of-view (FOV) of this system geometry around 20mm. In addition, the point-source imaging study is repeated with the SPECT system placed inside and outside the MRI scanner, while keeping the imaging geometry unchanged. The total imaging time for the data acquisition is one hour and the image is reconstructed with the standard MLEM algorithm in 20 iterations. In reconstruction, photon penetration in pinhole aperture is modeled. The reconstructed images of two sources at six different view angles are shown in Figure 3O, in which 250μm sphere source could be resolved very well, with spatial resolution 390μm in Figure 3R.

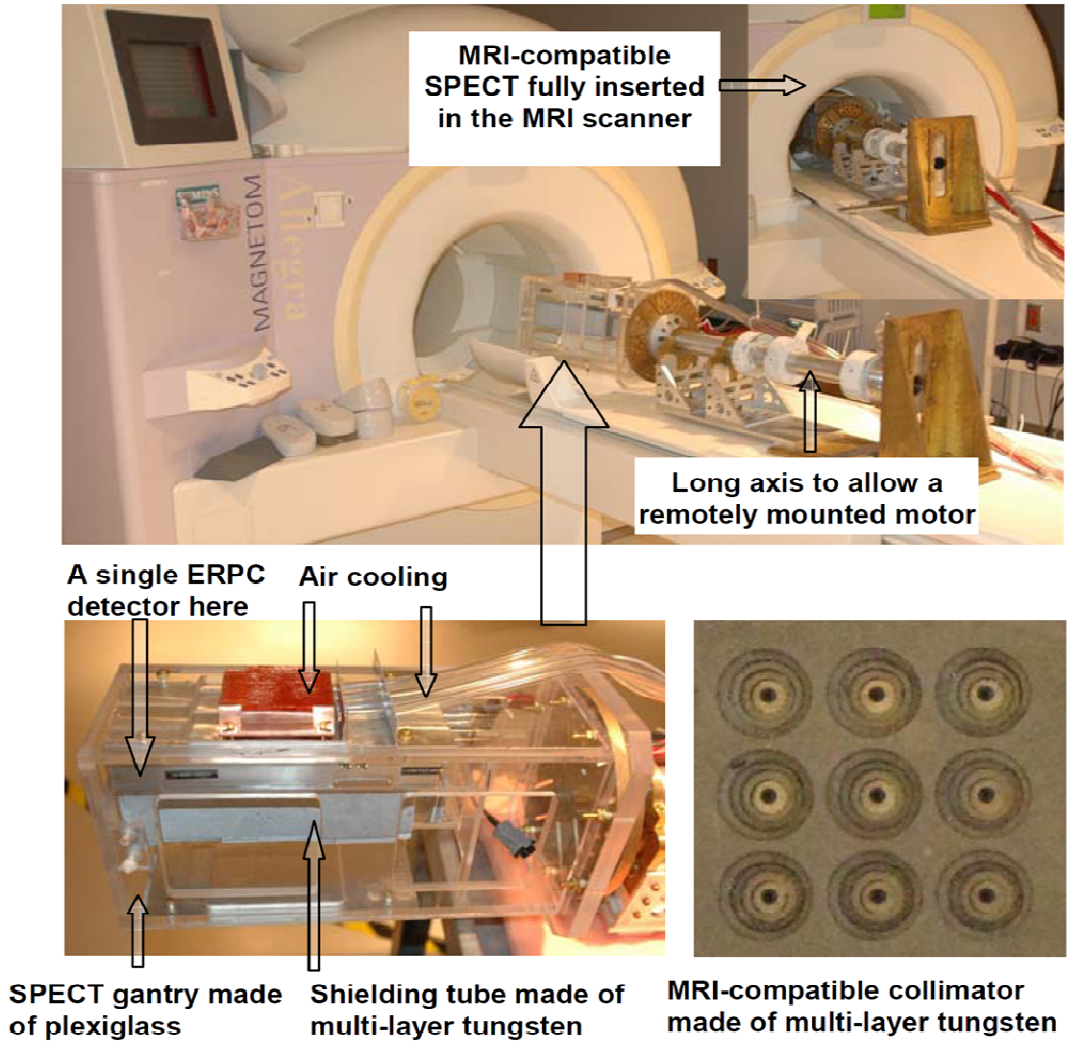

Figure 3M: Upper: A prototype MRI-compatible SPECT system installed on the patient bed of Siemens 3T MR scanner; Left bottom: The non-magnetic gantry with a single ERPC detector and cooling; Right bottom: The MRI-compatible collimation aperture made of multiple layers of 0.5 mm thick pure Tungsten sheets.

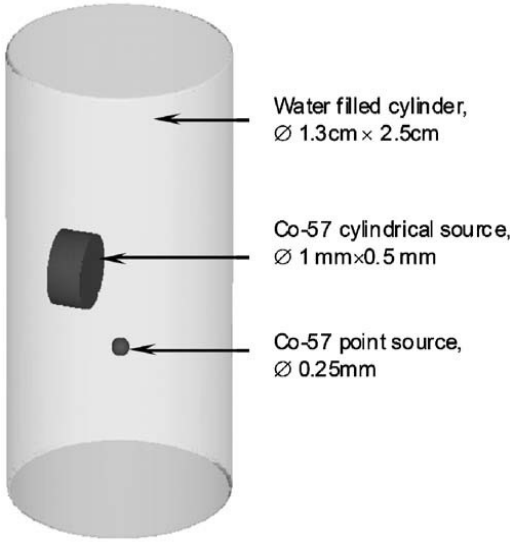

Figure 3N: Phantom containing two Co-57 sources

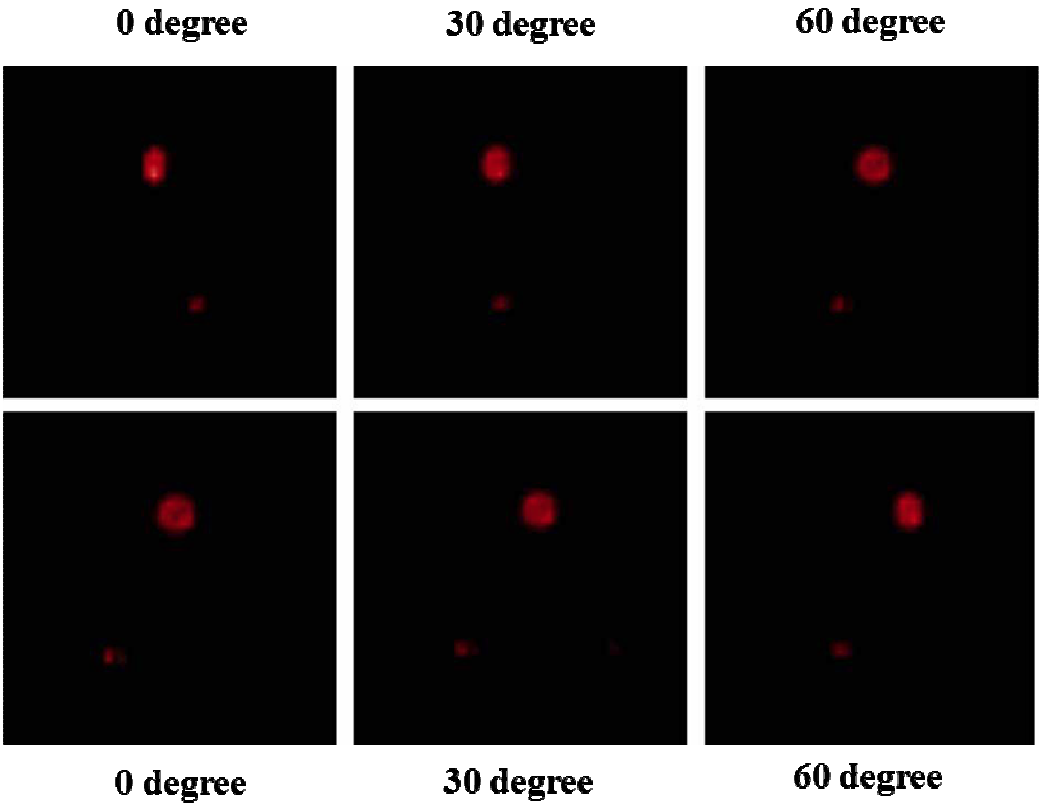

Figure 3O: Reconstructed images of two Co-57 sources at six different view angles.

By this phantom study, the imaging performance is proved with this detection system. When keeping the imaging geometry exactly unchanged, we placed the system with sphere source into 3.0T MRI scanner to investigate the effect of strong magnetic field in SPECT images. For that purpose, we compared the pinhole projections and the 2D cross-section of SPECT image acquired at the center of the MRI scanner and outside MRI room (as Figure 3P and 3R).

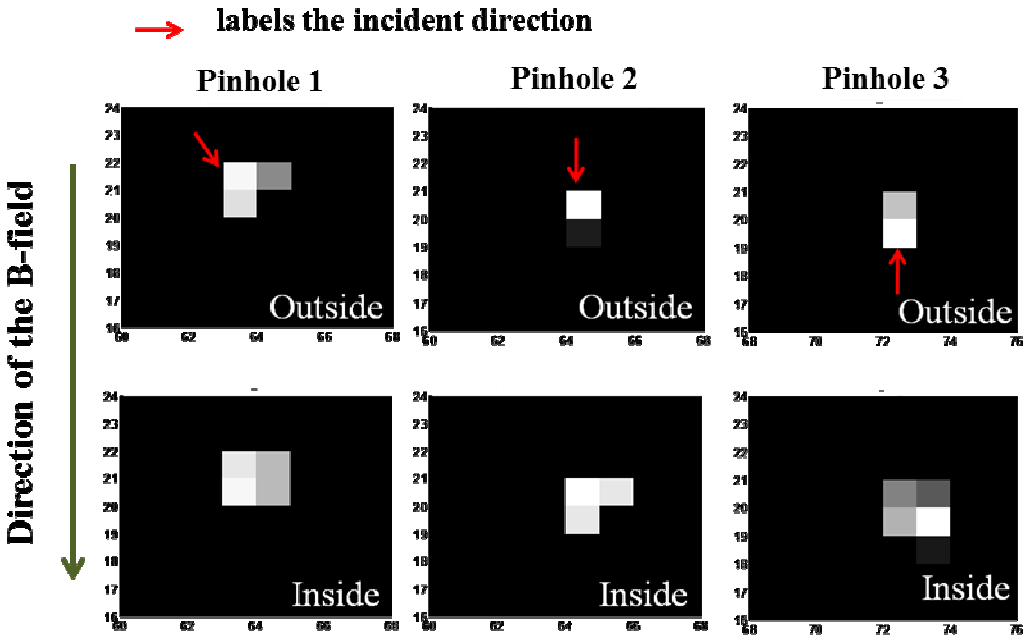

Figure 3P: Pinhole projections obtained inside and outside MRI

With three different incident directions, the pinhole projections show obvious spreading vertical to the magnetic field due to Lorenz angle for electron drifting (as Figure 3Q). If no correction is added into the reconstruction, it leads to the broadening of point source image along the direction vertical to the magnetic field. But along another direction parallel to the main magnetic field, there is no significant degradation of the imaging performance. With SPECT images of the point source, we confirmed that the spatial response of highly pixelized detector is affected by magnetic field and the strong magnetic field causes obvious position error and spatial resolution degradation.

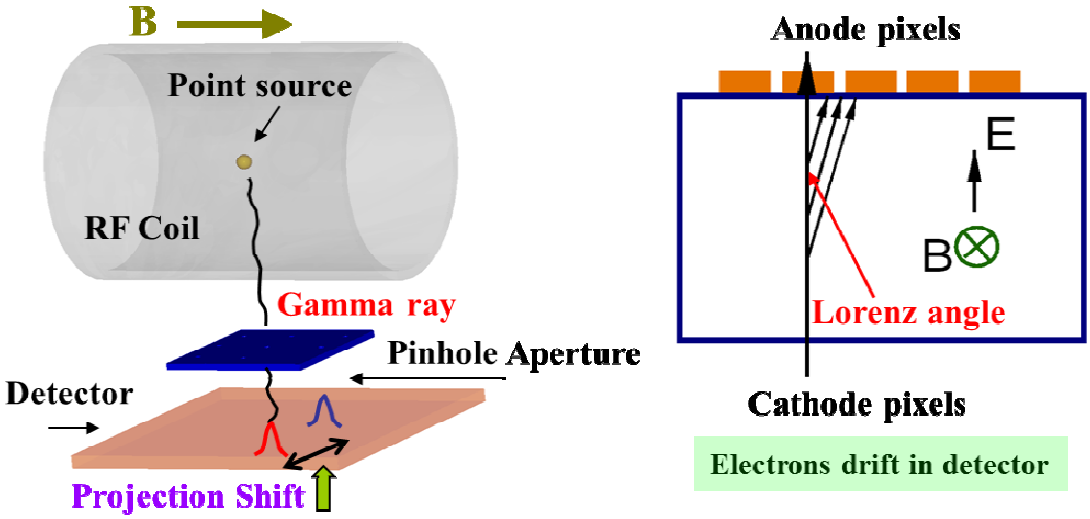

Figure 3Q: Lorenz force applied on electrons in semiconductor detector

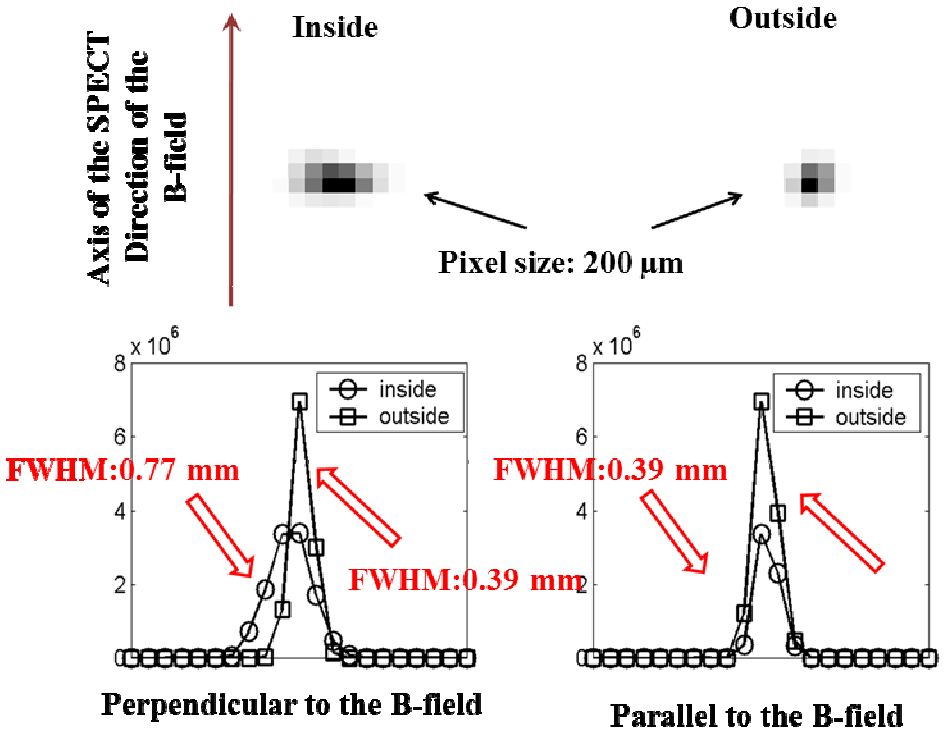

Figure 3R: Top: 2-D cross sections of the point source images acquired with exactly the same SPECT geometry inside and outside the 3.0T MRI; Bottom: 1-D cross sections of the point source images cutting through the peak pixel.

3.5 Summary

In this chapter, we presented some preliminary imaging results obtained by a prototype of a high resolution SPECT system based on the energy-resolved photon counting CdTe detector system. A series of studies are performed to investigate the performance of the detectors and the SPECT system. These studies demonstrate that the ERPC detector could reliably work inside the 3.0T MRI scanner, and prove the feasibility of high spatial resolution in MRI scanner. It provides an excellent energy resolution of around 4keV and an intrinsic spatial resolution of 350μm for gamma rays with 140keV incident energy.

Placing a high-resolution semiconductor sensor inside a strong magnetic field raises several concerns. Besides the interference from the metal parts of the gantry, the eddy current induced by varying magnetic field on the large cathode plane and readout circuitry leads an increased noise level as previously reported in [20]. Secondly, as reported chapter 3.4, even when a detector with 1mm in thickness is in use, the collection of charge carriers, acquired projections and the reconstructed image are still affected by the Lorenz force. Therefore, a relatively thicker detector (ex. 2-4 mm) leads to an increased probability for charge sharing, event positioning error and image blur as previously shown in Figure 3P and 3R. For achieving an ultrahigh spatial resolution, the field-induced event-positioning error appears to be a critical issue that needs to be solved for achieving the target resolution (300-500μm). One of the most straightforward methods to solve this issue is to add the charge collection process with effect of magnetic field in the system response function (SRF) of SPECT, which helps to compensate the broadening or blur of the image acquired inside the MRI and allow capability of high spatial resolution. This procedure provides a more accurate modeling of important physical processes inside MRI, which should allow one to account for the event positioning error caused by magnetic field.

To improve the sensitivity of the pinhole system, the current SPECT setup needs to be refined by adding more detectors inside the magnetic field for image studies. The charge shifting and collection based on magnetic field can be further modeled. Detailed measurement of the charge sharing events and collection is needed to modify the SRF at all angular positions. More phantom

studies are needed to further study the interference between SPECT and MR systems. This proposed MRI-compatible SPECT system allows a near ideal co-registration between the very-high resolution functional SPECT images and MR images with excellent tissue contrast. One can therefore correlate the complementary information from both systems for in vivo mouse brain imaging and many other applications.

CHAPTER 4
STUDY OF THE RESPONSE OF CdTe ERPC DETECTORS IN STRONG MAGNETIC FIELD

In this chapter, we present the results from a detailed study of the response function of small-pixel CdTe and CdZnTe (CZT) detectors operated inside strong magnetic field. This represents a key step towards the development of a MRI-compatible SPECT system that is based on a recently developed energy-resolved photon-counting (ERPC) CdTe detector with 350 μm pitch size. For CdTe or CZT detectors operated inside a strong magnetic field, the movements of electrons and holes and the subsequent charge-collection processes are affected by Lorenz force. To model the effect of magnetic field, precise understanding of the charge collection behavior and the field-induced distortion in projections are crucial for reconstructing SPECT images inside a MRI system. In this study, we have developed a comprehensive Monte Carlo model for predicting the response function of ERPC CdTe detectors operated inside the MR scanner. This model is subsequently validated in a comparative study against experimental results obtained with a prototype MRI-compatible SPECT system. Finally, the experimentally calibrated detector response model is used to predict the imaging performances of several MRI-compatible SPECT systems built with different detector configurations and MR scanners of different field-strengths. This study provides critical insights for further refining the design of the MRI-compatible SPECT system for achieving an ultrahigh spatial resolution.

4.1 Monte Carlo simulation model of the charge collection behavior in semiconductor detector

4.1.1 Gamma ray transport

The interactions of gamma ray and its secondary particles in the object, the collimators and the detectors are modeled with GEANT 4 [49]. This model includes detailed geometry of a

spherical Co-57 source and two types of collimators (chapter 3.1 and 3.4) that we used in experimental studies. The simulation yields a list mode data that records the location and energy deposition for each event interaction.

4.1.2 Initial Charge Carrier Distribution

In generation process of random charge carrier with a given energy deposition, E_d, at a known position R, the number of electron-hole pairs N is assumed to be a Gaussian random number, with its mean being

$$N_{avg} = \frac{E_d}{\varepsilon} \tag{1}$$

and the standard deviation being

$$\sigma_N^2 = F \cdot N_{avg} = F \cdot \frac{E_d}{\varepsilon} \tag{2}$$

where ε is the ionization energy. The Fano factor is assumed to be 0.1 for CdTe [50]. The initial positions of each charge carriers, $\mathbf{r_0}$, are chosen randomly based on a modified isotropic 3-D Gaussian function centered at interaction position given by GEANT 4 simulation and with a standard deviation $\sigma_{\mathbf{r_0}}$ of 10-20 μm. Note that the tail of the Gaussian distribution is truncated, the distance between the center and the actual initial position of any carrier is bounded to below two times of the standard deviation. Therefore, the maximum charge carrier cloud size, allowed in this simulation, is between 30-40 μm in radius [51].

4.1.3 Charge Carrier Movement inside ERPC Detectors

The electric field **E** and weighting potential function φ (in respect to the cathode and given anode pixels) within the pixelized CdTe detector are calculated numerically (5.0 μm grid size) by solving Poisson equation with boundary conditions according to exact configuration of the ERPC detector. The calculation is implemented by commercial software Maxwell3D [52]. A bias voltage of 200V/mm is applied between the cathode and the anodes pixels in this calculation.

With an electric field strength of 200 V/mm, the charge carriers are assumed to drift following

TABLE 4A: Parameter of simulation

Material parameters	Parameter
Mobility of electron μe	1100 $cm^2/(V \cdot s)$
Mobility of hole μh	200 $cm^2/(V \cdot s)$
Lifetime of electron τe	3.0 μs
Lifetime of hole τh	2.0 μs
Ionization energy for	4.65 ev
Lorenz angle for electron	18 degree
Lorenz angle for hole	2.0 degree
Electric field strength	200V/mm

the electric field lines with a velocity of

$$v_{e,h} = \mu_{e.h} \cdot E \tag{3}$$

where **μ** is mobility of charge carriers as shown in Table 4A. To model the movement of charge carriers under the influence of both electric field and magnetic field, we adopted the method discussed in [53], which gives the expression for the mobility matrix of charge carriers in the steady state for general directions of electromagnetic field vectors. Considering the main magnetic field combined with Hall Effect, the velocity of charge carriers could be derived by formula being

$$\begin{bmatrix} v_x \\ v_y \\ v_z \end{bmatrix} = K \cdot \begin{bmatrix} 1+\mu_H^2 B_x^2 & \mu_H^2 B_x B_y - \mu_H B_z & \mu_H^2 B_x B_z + \mu_H \cdot B_y \\ \mu_H^2 B_x B_y + \mu_H B_z & 1+\mu_H^2 \cdot B_y^2 & \mu_H^2 B_y B_z - \mu_H B_x \\ \mu_H^2 B_x B_z - \mu_H \cdot B_y & \mu_H^2 B_y B_z + \mu_H B_x & 1+\mu_H^2 B_z^2 \end{bmatrix} \times \begin{bmatrix} E_x \\ E_y \\ E_z \end{bmatrix} \tag{4}$$

Due to the orientation of detectors in respect to the main magnetic field, which always allows the detector plane parallel to **B**, we assumed **E**=E_x and **B**=B_y, to simplify the charge carrier drift velocity being

$$\begin{bmatrix} v_x \\ v_y \\ v_z \end{bmatrix} = K \cdot \begin{bmatrix} E_x \\ 0 \\ -(\mu_H)_{e,h} \cdot B_y E_x \end{bmatrix}; \quad K = \frac{-\mu}{1+\mu_H^2 B^2}; \tag{5}$$

where μ_H is the Hall mobility. Therefore, for a detector positioned inside a MRI scanner, the charge carriers always move at the direction with fixed angle $\theta_{e,h}$ (as Figure 4A) respecting the

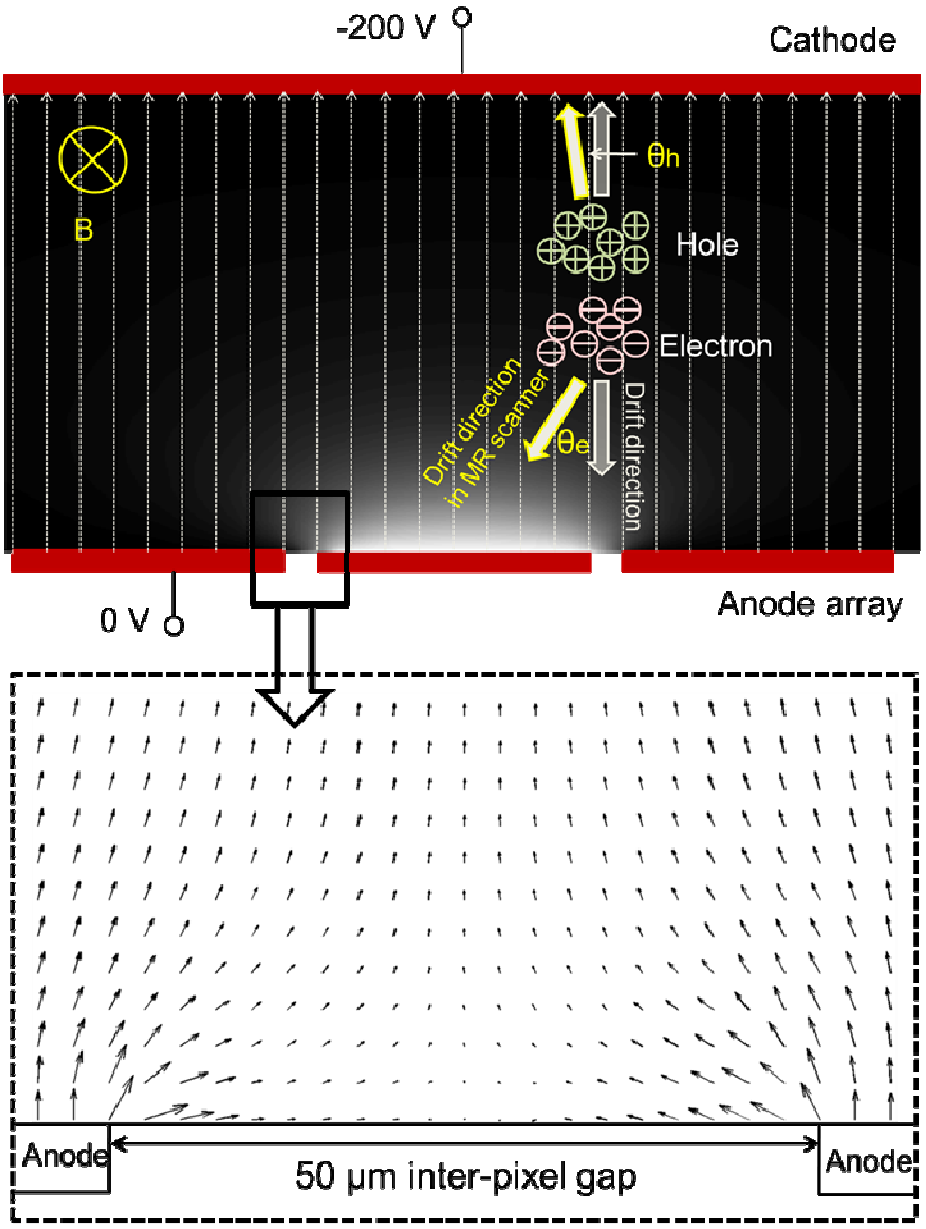

Figure 4A: Top: Electron and hole drift in electromagnetic field of pixelized detector and 2D weighting potential (gray scale); Bottom: Simulated electric field in pixel gap region.

electric field ***E***. The angle can be calculated as

$$\tan\theta_{e,h} = \frac{v_z}{v_x} = -(\mu_H)_{e,h} \cdot B_y \tag{6}$$

With the initial position and the motion equation of each charge carrier, one can predict its trajectory from the origin to the collecting electrode. Note that not all the charge carriers can be collected by the electrodes because of charge trapping during their transportation (de-trapping is not considered), so we defined a life time $\tau_{e,h}$ that represents the characteristic average time before an electron or hole falling into a trap, and actual trapping time for all charge carriers (electrons and holes) is determined randomly following exponential distribution being

$$P_{e,h}(t) = \frac{1}{\tau_{e,h}} \cdot e^{\frac{-t}{\tau_{e,h}}} \tag{7}$$

With the initial charge carrier distribution and drift, when an interaction occurs, our model can track the movement of each charge carrier in electromagnetic field, and record the trajectory $\mathbf{r_{e,h}}(t_i)$ at constant time steps t_i with unit time dt (1.5×10^{-9} s) from charge origin to the collecting electrode or trapping location.

In addition, charge diffusion, electron particularly, is another physics factor, which influences the detector spectral response. To simplify the computation, we assumed that the diffusion is separated from drifting process. In our model, the diffusion is implemented and combined at the starting location of drifting for each charge carrier, and thus the start position of each charge is regenerated by a 3-D Gaussian function centered at the initial charge position $\mathbf{r_0}$ with a standard deviation σ. The value of newly defined σ, instead of $\sigma_{\mathbf{r_0}}$, is calibrated by using uniform setting and depth-dependent setting, and results of simulation are presented in Chapter 4.3.

4.1.4 Charge Induction on the Anode Pixels of ERPC Detectors

With predicted the trajectory of each electron-hole pair j, $\mathbf{r^j_{e,h}}(t_i)$, the induced charges $Q_j(t_i)$ of the any anode could be derived by the equation (8) [48] [55]

$$Q_j(t_i) = -q_0 \cdot [\varphi(r_e^j(t_i)) - \varphi(r_h^j(t_i))]; \tag{8}$$

where q_0 is the unit charge. By considering all the trajectories of charge carriers, the total induced charge each interaction is induced by

$$Q(t_i, R) = \sum_{j=1}^{j=N} Q_j\,(t_i); \tag{9}$$

where N and R are the total number of electron-hole and location of each event interaction. An example of anode waveform is shown in Figure 4b.

By integrating all these effects, our model can achieve accurate predictions on the charge drift with and without magnetic field. This information helps us to compensate the event-positioning error in reconstructed images induced by the strong magnetic field.

4.1.5 Uncertainty of the Simulated Waveforms on Anodes

As we discussed, the random fluctuations associated with charge carrier generation and transportation caused uncertainty in waveform on anodes. Moreover, the readout electronic noise contributes the extra uncertainty to the waveforms, which is proved to be more significant for energy resolution and modeled by Gaussian white noise. The noise from charge carrier has the variance and covariance of the induced charges at time t_i are given as

$$\mathrm{Var}(Q(t_i) \mid R)) = \sum_{N} \sum_{Q(t_i)} [Q(t_i, R) - \overline{Q}(t_i, R)]^2 \cdot P(t_i, N)$$

$$\mathrm{Cov}[Q(t_i), Q(t_i + \Delta t)] = \sum_{N} \sum_{N_d(t_i)} \sum_{Q(t_i+\Delta t)} \sum_{Q(t_i)} [Q(t_i, R) - \overline{Q}(t_i, R)] \times [Q(t_i + \Delta t, R) - \overline{Q}(t_i + \Delta t, R)]$$
$$\times P(t_i, t_i + \Delta t, N, N_d(t_i)) \tag{10}$$

where $\overline{Q}$ is the mean waveform. N and $N_d(t_i)$ are number of charge carriers initially and survived after a drift time t_i [54].

4.1.6 Modeling of Shaping Amplifier Response

By simulating induced charges on anode pixel as a function of drifting time ti, the waveforms on anodes are described by equation (11).

$$Q(t_i, R) = \sum_{j=1}^{j=N} Q_j\,(t_i); \quad t_i \le T_c$$
$$Q(t_i, R) = \sum_{j=1}^{j=N} Q_j\,(T_c); \quad t_i \ge T_c \tag{11}$$

where T_c is the time by which all free charge carriers are collected. Ideally, the readout energy from each pixel channel should be proportional to the induced charges. However, the charge collection time fluctuation, which leads to the ballistic deficit effect, may cause energy resolution

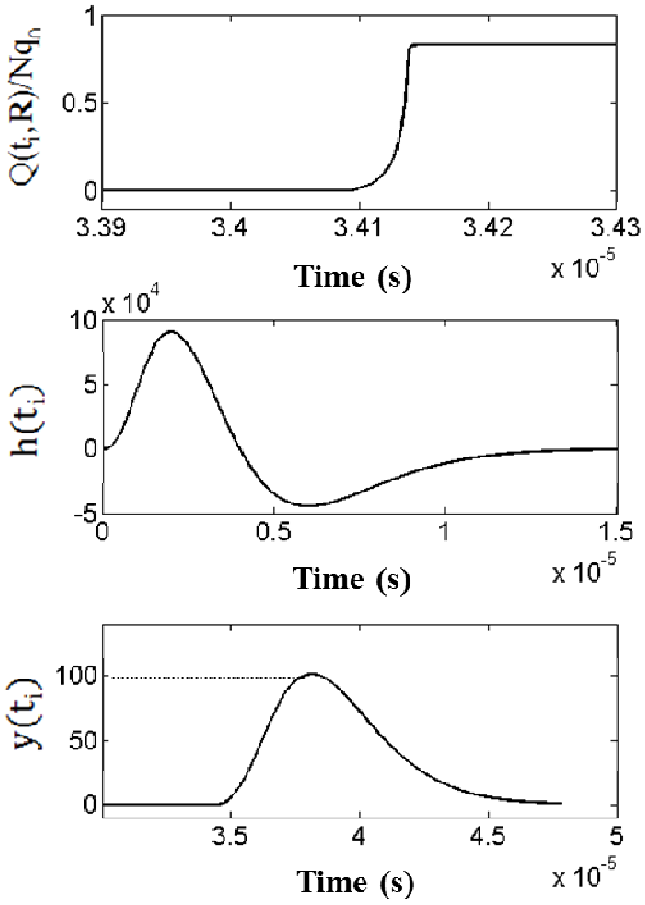

Figure 4B: Simulated pre-amplifier output pulse waveform and shaped pulse using CR-$(RC)^m$ function @122kev. Top: Scaled waveform; Middle: CR-$(RC)^m$ shaper response function; Bottom: Signal after shaping.

degradation in preamplifier output signal shaping process. Therefore, the loss of amplitude of shaper signal due to the ballistic deficit effect cannot be ignored in our model.

To convert the preamplifier output signal to the energy related amplitude of shaper signal, we continually modeled the response of CR-$(RC)^m$ shapers and discrimination process of the readout system, which is implemented by a convolution of the waveform $Q(t_i, R)$ and an impulse response function $h(t_i)$ for CR-$(RC)^m$ system.

$$y(t_i) = Q(t_i, R) * h(t_i)$$
$$h(t_i) = \frac{1}{m!} \cdot e^{\frac{-t_i}{\tau_{RC}}} \cdot [m \cdot \frac{t_i^{m-1}}{\tau_{RC}^m} - \frac{t_i^m}{\tau_{RC}^{m+1}}] \quad (12)$$

where $m = 4$ and τ_{RC} is RC constant with value 1μs. The amplitude of shaper output signal $y(t_i)$ represents detected energy E_f. A sample of preamplifier and shaper signals has been showed in Figure 4B.

These integrated modeling steps allow us to reproduce the physics in gamma ray detection and predict the detector energy and spatial response to any incident event in strong magnetic field. In Figure 4C, all modeling steps are presented, and simulated results are validated experimentally by multiple studies.

4.2 Experimental validation of charge collection and detector response with and without effect of varying magnetic field strength

To validate and optimize the modeling, we experimentally evaluated the 1-2 mm CdTe ERPC detector responses inside a 3T magnetic field, which is one of the critical steps for the development of a high spatial resolution MRI-compatible SPECT imaging system for small animal studies. In this experiment, two source-collimator assemblies (as shown in Figure 4D) are designed to create incident photon beams with known angles-of-incidence. We compared the modeled spatial and spectral responses of detectors with experimental results obtained by those

two geometries. This allowed us to calibrate the parameter settings and to verify the accuracy of modeling by comparing the spectrum shape.

Firstly, a "parallel" gamma ray beam created by a highly machined collimator is used to scan and irradiate the pixels of detector from various angles. The collimator we used is made of a stack of finely machined tungsten blocks of 500μm × 600μm × 12mm in size. It leaves a square hole of 100μm × 100μm × 12mm as shown in Figure 4D (Chapter 3). This collimator with a Co-45 point

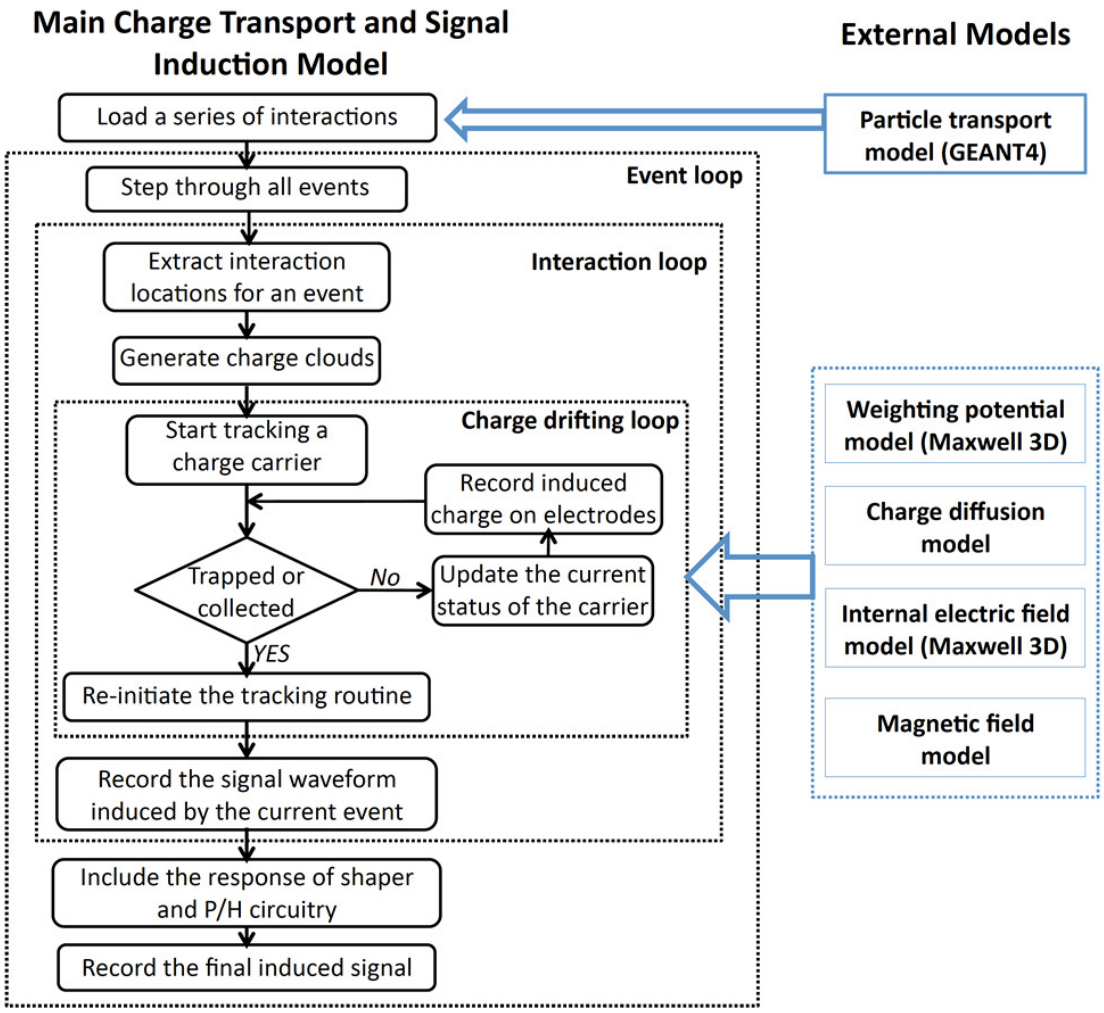

Figure 4C: Simulation steps for charge drifting and collection

source is placed closed to the surface of the detector, and positioned by a high-precision non-magnetic 2-D linear stage and a goniometer. This setup allows the collimated gamma ray beam to irradiate planned regions of detector with known incident angles.

Secondly, a Tungsten multiple pinhole aperture is fixed on top of the detector as Figure 4D and a Co-57 point-source is moved around at known locations to create multiple realistic incident beams seen in typical SPECT imaging. The pinhole aperture is made of multiple Tungsten pinhole inserts (Ø200 μm and Ø 400 μm) embedded into a 8mm thick square lead piece. A precise system calibration process can derive the geometry parameter for the pinhole setup.

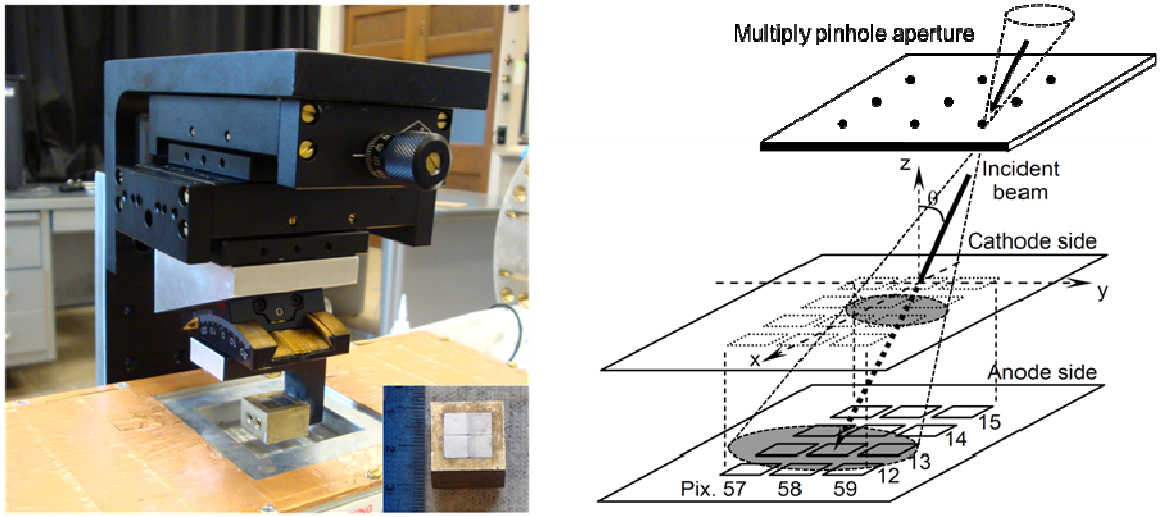

Figure 4D: (left): The general view of the mechanical setup for collimator scanning above the detector. The picture at the corner is the top view of the collimator with 100μm × 100 μm square hole at the center; (Right) Schematic of pinhole-detector geometry.

The measured energy response under those two geometries allows detailed studies of the charge collection process and helps to demonstrate the modeled detector response under exact detector configurations. The experimental measurements are repeated in a pre-existing Siemens MRI scanner with geometries unchanged. The obtained projection distortion induced by the strong magnetic field is compared with the predictions from corresponding simulations and an excellent agreement has been achieved, as Chapter 4.3.

4.3 Comparison results of modeling and measurement

4.3.1 Detector Response without Magnetic Field

The main purpose for this study is to confirm that the simulation procedures, as described in Chapter 4.1, could yield an accurate prediction of spatial and spectroscopic response functions of pixelized ERPC CdTe detectors. The first step is to fine-tune the simulation parameters, including drifting and diffusion parameters, to produce realistic energy spectra. In Figure 4E, 4F and 4G, several simulated 122 keV photopeaks are compared with the measured ones.

By using two source-collimator assemblies as described in chapter 4.2, we simulated projections and energy spectra of the irradiated pixels of 1mm and 2mm CdTe ERPC detectors. The gamma ray pencil-beam with normal incidence is controlled to scan along the straight line parallel to the cathode plane of the detector, which formed multiple realistic beam locations among pixels. We simulated the irradiation and predicted the beam projections and their spectral performance with known incidences. The incident beam profile is provided by Geant4 and its local position of the detector is obtained by least square fitting.

The CdTe detectors response differently when interactions occur at the different depths. This has been confirmed by simulated results in the sense that the use of depth-dependent charge collection process provided a better fit to the measured energy spectra (Figure 4E). To achieve this conclusion, several parameters such us $\mu\tau$ (Table 4A) for charge drifting and σ for diffusion were fine-tuned to compare with the measurements.

First of all, under $\mu\tau$ setting as Table 4A, we simulated the 122kev photopeaks of single pixel in projection obtained by 1mm and 2mm detector (Figure 4E) with setting σ = 10 μm, 16 μm, 26 μm, and depth-of-interaction (DOI) z dependent $\sigma(z)$ of electron ($\sigma(z)$ is set as a linear function from 0 μm to 30 μm with DOI from anode to cathode). In this study, we assumed that the detector response change caused by hole drift with different σ settings in diffusion is negligible. The simulated energy spectra for 1mm and 2mm detector are shown in Figure 4E. By summarizing comparisons, the shape of spectra is less sensitive to $\mu\tau$ than σ as simulated 122kev photopeaks with different parameter settings, since the thickness of detector is only up to 2mm. In the model,

all the parameters in charge collection are chosen based on the sum of squared relative errors labeled in Figure 4E, which are from comparisons between simulated and measured counts in energy window cut around the 122kev and calculated by

$$\text{Error} = \sum_{i} \left(\frac{\text{Count}_i^{\text{exp}} - \text{Count}_i^{\text{model}}}{\text{Count}_i^{\text{exp}}}\right)^2; i \in [111,130\text{kev}] \tag{13}$$

With current setting of μτ-product (Table 4A) and σ(z), we are able to predict the gamma ray projections on 1 mm ad 2mm thickness detectors and the corresponding energy spectra with a reasonable accuracy as shown in Figure 4F and 4G.

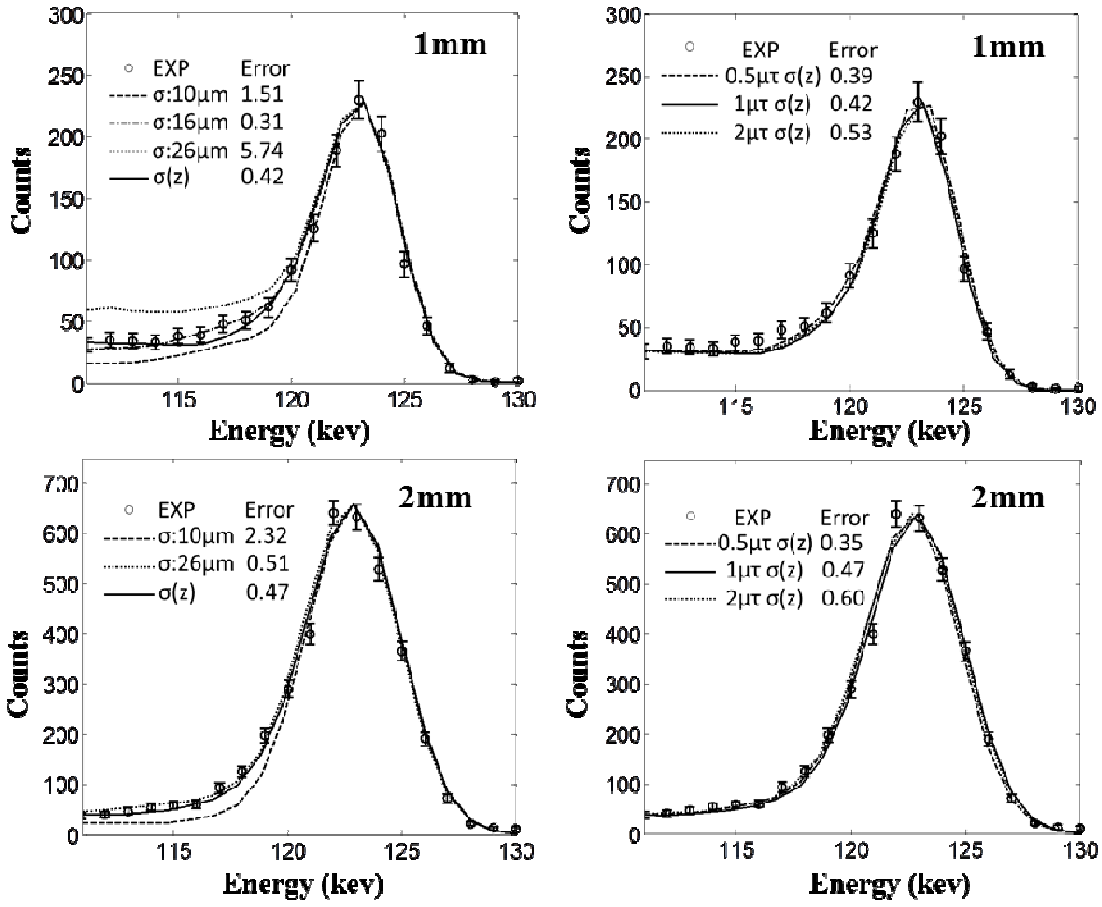

Figure 4E: (Left column) Simulated and measured energy spectra (122kev) of a single pixel for 1mm (top) and 2mm (bottom) ERPC CdTe detector with multiple σ setting; (Right column) Simulated and measured energy spectra (122kev) of a single pixel for 1mm (top) and 2mm (bottom) ERPC CdTe detector with multiple μτ setting.

In Figure 4G, it is noticed that simulated energy spectra within lower energy range including X-Ray escape peak and Compton scattering continuum are lower than the measurements. This is caused by the backscattering, which was not considered in the model. However, this mismatch is negligible, because only the counts within the photopeak range are accounted in detector response and measured projections. Simulated and measured count distributions of 1-2mm detector are compared and labeled in Figure 4F. The minor difference is mostly depending on the accuracy of pencil-beam position obtained by least square fitting. With the pencil-beam geometry, the spatial and spectroscopic response of 1mm and 2mm detectors can be predicted with calibrated model and an agreement is achieved between simulation and measurement. But the accuracy of the model needs to be much improved by pinhole imaging system.

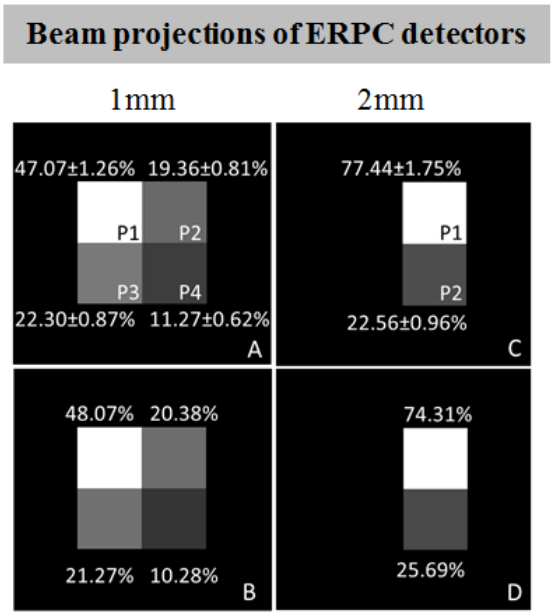

Figure 4F: Measured (A) and modeled (B) beam projections for 1mm ERPC CdTe detector and measured (C) and modeled (D) beam projections for 2mm ERPC CdTe detector.

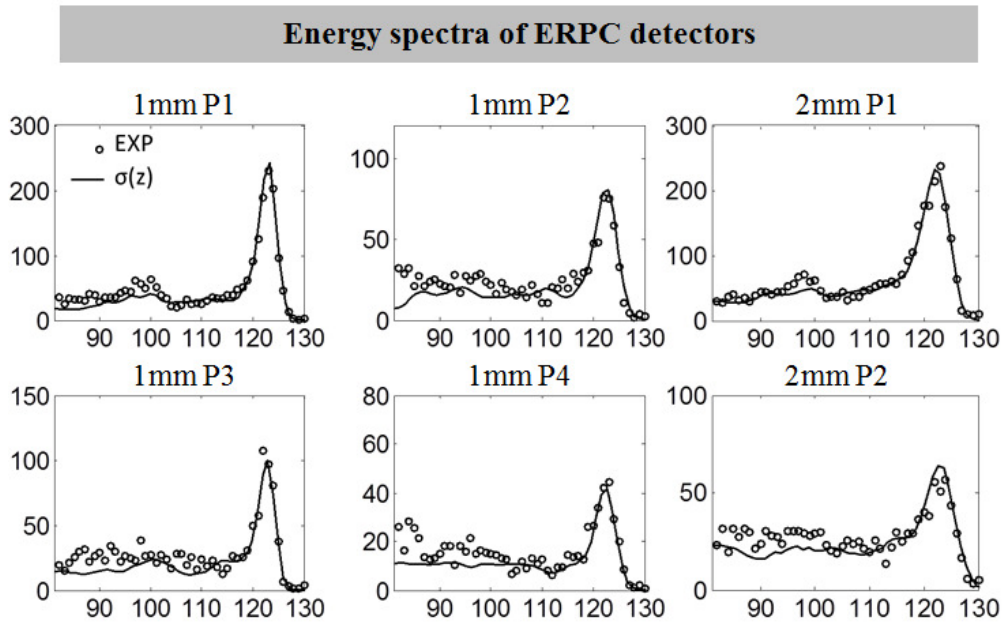

Figure 4G: Corresponding pixel spectra for 1 and 2mm ERPC detector obtained by experiments and simulations. All parameter setting in the model are in Table 4A.

4.3.2 Detector Response in 3T Magnetic Field

The magnetic field-induced the projection distortion is quantified by using another setup, sphere source (Ø250μm) coupled to multiple-pinhole aperture (200 and 400 μm) as Figure 4D. Projections of the fixed Co57 point source are obtained with experimental setup placed inside and outside the MRI scanner to cover SPECT imaging process (Figure 4I). This MR field induced distortion is modeled and built it into SPECT image reconstruction for blurring compensation. Precise geometry calibration with no presence of magnetic field helped to describe the path of the photon transmission through the pinhole aperture and detector. In the calibration, a single pixel volume was divided into 8×8×8 subpixels to map the projection shifting as the location of interaction changes in the single pixel volume.

As plot in Figure 4H, the projection of 1mm detector shifted 160 μm averagely (first-order effect) when the system is placed and rotated in 3T magnetic field area. However, the inhomogeneity of main magnetic field with presence of SPECT inserts caused that projections suffered different shift amplitudes toward different directions at eight angular positions

(second-order effect). The acquired projections of the fixed Co57 source at all angular positions of imaging process helps to quantify the Lorenz angle in 3D space as a function of angular position and pinhole number, and thus a projection shift map can be built into reconstruction with known Lorenz angles, which covers the first- and second- order effects.

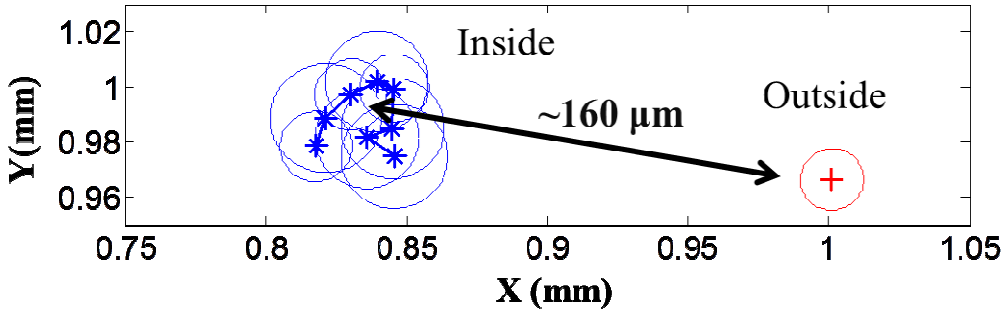

Figure 4H: Pinhole projections of point source acquired outside MRI and eight angular locations for SPECT inside 3T MRI scanner with incidence geometry unchanged. The radius of each circle is standard deviation of 2D position of projection.

We modeled the projections of a point source through a pinhole and repeated the computation with and without effect from 3T magnetic field. These results are compared to the experimental results, as shown in Figure 4I.

By using 1 and 2 mm ERPC CdTe detectors, source-pinhole projections obtained outside and inside 3T MRI scanner are shown and compared with modeled ones in Figure 4J. The error labeled is calculated by a formula being

$$\text{Error} = \sum_{j} (p_j^{exp} - p_j^{mod})^2; \text{ with } \sum_{j} p_j^{exp} = \sum_{j} p_j^{mod} = 1 \qquad (14)$$
$$j \in \text{Pixel pool in a single pinhole projection}$$

where pj is the normalized count in pixel j. The 3T field-induced distortions in detectors with two different thicknesses are both predicted by the model, reflected in projection (Figure 4I and 4J) and 122kev photopeak spectra of mainly responded pixels (Figure 4K and 4L). In this spectrum

simulation, only photoelectric effect is considered and other physics such as scattering and X-ray

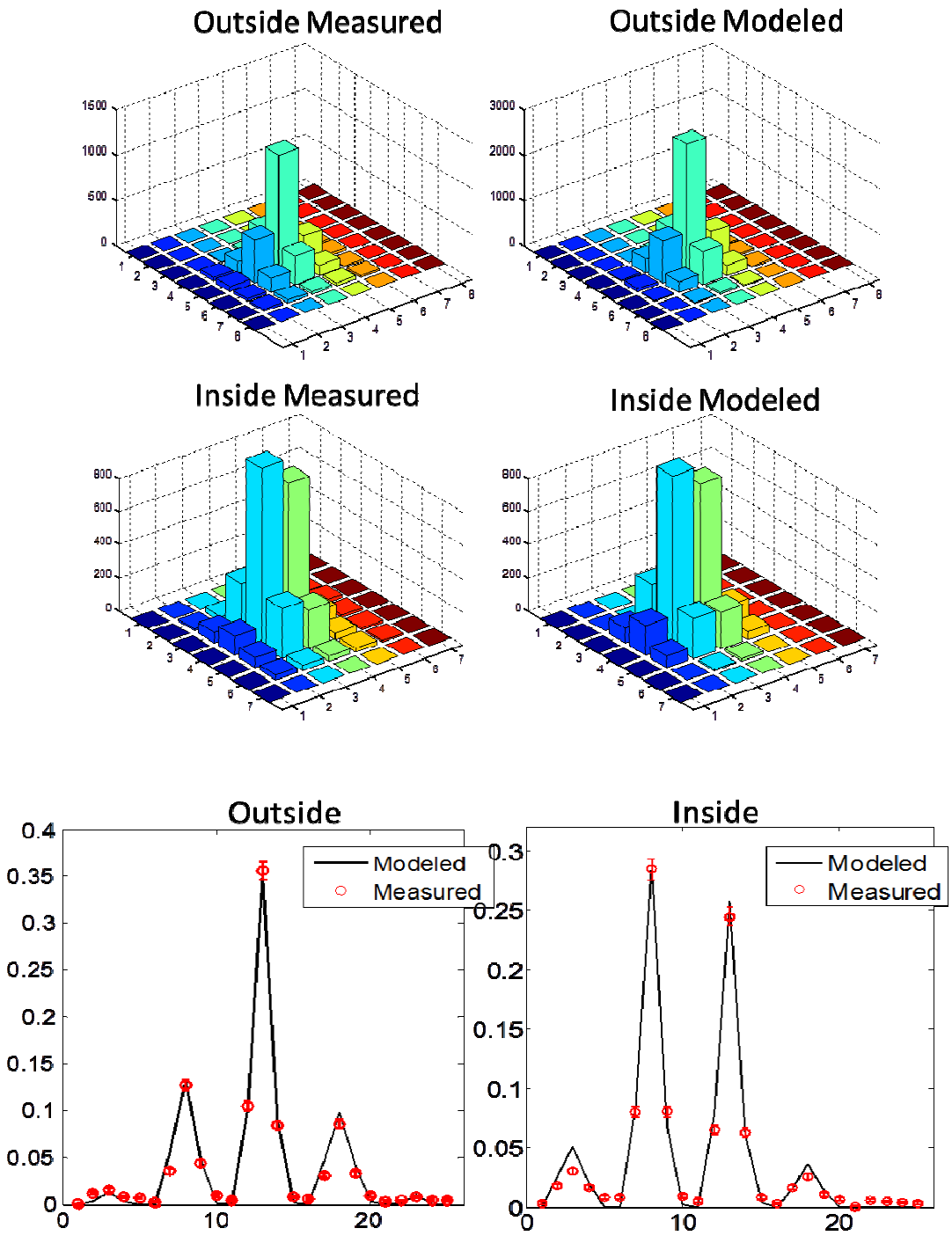

Figure 4I: Top: Measured and modeled pinhole projection outside and inside 3TMRI; Bottom: Normalized count distribution of the responded pixels.

escape are not included in the model, which partially leads mismatch in lower energy region. Also, the uncertainty of the geometry calibration is not negligible for this comparison. In SPECT setup, nine pinhole (200 μm) projections for 1mm detector and four pinhole (400 μm) projection for 2mm detector are modeled to fit measurements, and errors calculated by (14) are plotted in Figure 4M, as a function of angular position and pinhole number. Most simulated projections fit the measurements very well, and slightly better agreement on 2mm CdTe detector based on labeled error is partially caused by higher sensitivity with larger pinhole size and thicker crystal.

4.4 Simulation of SPECT images obtained in varying magnetic field

Continued with investigation of 1-2mm detector response when working in 3T MR field, pixelized detector response and imaging performance with thick detector (2mm and 5mm) in MR field (3.0T and 9.4T) are evaluated by SPECT imaging simulation.

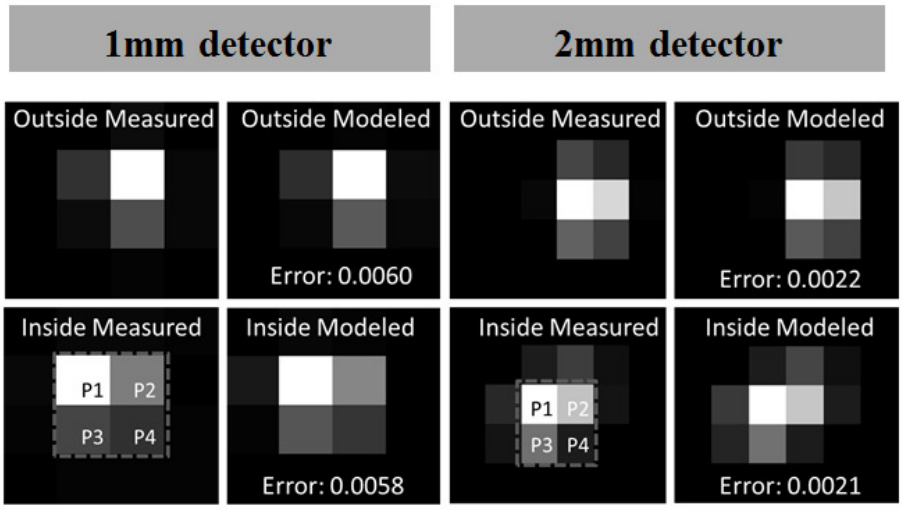

Figure 4J: Pinhole projections of 1mm (Left panel) and 2mm (Right panel) ERPC detector acquired outside/inside MRI with modeled projections. 200 μm and 400 μm pinhole apertures were coupled to 1mm and 2mm detector.

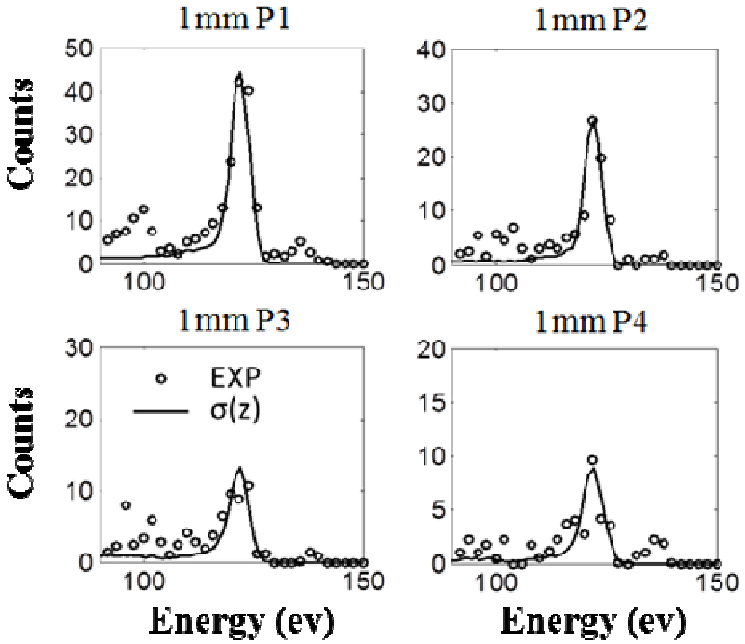

Figure 4K: Corresponding pixel spectra for 1 mm ERPC detector experimentally obtained inside 3T MRI scanner and compared with modeled spectra.

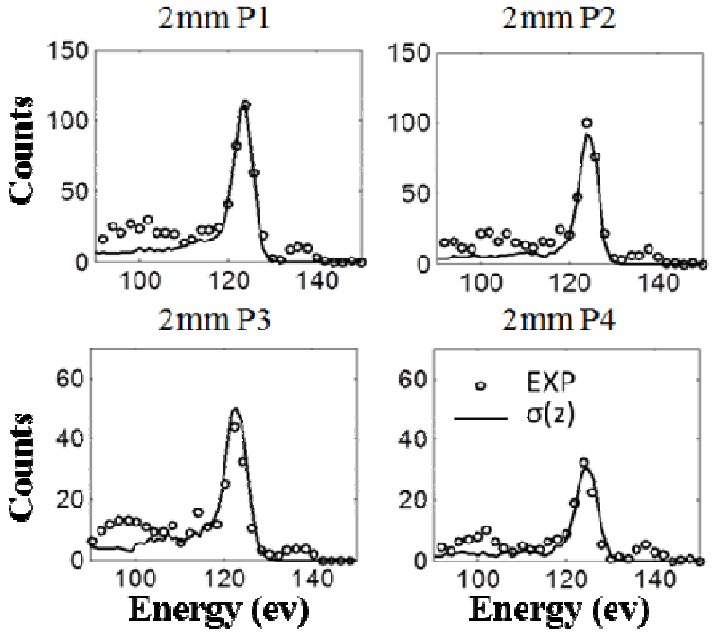

Figure 4L: Corresponding pixel (labeled in Figure 4j) spectra for 2 mm ERPC detector experimentally obtained inside 3T MRI scanner and compared with modeled spectra.

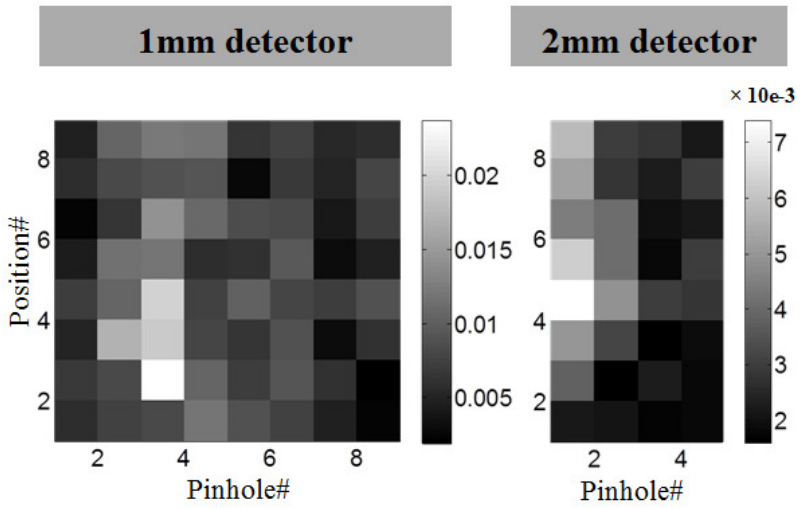

Figure 4M: Error plots of simulated 250 µm sphere source projections for 8-pinhole aperture (200 µm in size) coupled to 1mm detector and 4-pinhole aperture (400 µm in size) coupled to 2mm detector, when placed at 8 angular positions in SPECT imaging.

4.4.1 Digital 3D Mouse Brain Phantom

To evaluate the SPECT imaging performance, 3D digital mouse brain phantom from Beekman's lab [56] (Figure 4N) is used for SPECT simulation with voxel size 100 µm and 3D dimension 128×96×128. The total activity is 1mCi with 4 hours imaging time. The higher activity setting for mouse brain than as usual is based on two considerations: 1) some features in the phantom are much smaller than the intrinsic spatial resolution (200 pinhole and 350 detector pitch size); 2) the main purpose of this study is comparison of the imaging performance with and without presence of strong magnetic field.

The imaging performance of 1mm, 2mm and 5mm ERPC detector is evaluated with the compensation of effect from 3.0T and 9.4T magnetic field. In the simulation, the collimation aperture has 3×3 pinholes, 200µm in diameter and 60-degree open angle. The pinhole distance is 5.0cm. The detector-to-aperture and aperture-to-phantom distances are 32mm and 20mm. 2D projections of phantom are acquired in 360 degree at 8 angular positions, and image reconstruction is implemented by using MLEM algorithms.

With modeled magnetic field induced distortion in the system response function, simulated images obtained by 1mm, 2mm and 5mm detectors in 0T, 3.0T and 9.4T magnetic field are shown in Figure 4O and 4P. By using 1mm, 2mm and 5mm detector, the images obtained in 3.0T field proved the reasonable image qualities, when compared to the images with no presence of magnetic field. However, when 9.4T magnetic field is considered, there is obvious blurring even with distortion modeled in reconstruction (as Figure 4O and 4P), because under the effect of 9.4T, charges generated in single pixel volume is collected by much more pixels due to larger Lorenz angle. It leads to the significant broadening of point spread function (as Figure 4Q). One dimension profiles of reconstructed images are shown in Figure 4S.

To develop the MRI-compatible SPECT system working in multiple MRIs up to 9.4T magnetic field, depth-of-interaction (DOI) helps to accurate the system response function (as Figure 4Q). With DOI information, detectors or projections can be divided in to multiple independent layers, and the point spread function with DOI is converted into multiple independent portions in reconstruction. Reconstructed 3D images with modeled 9.4T field-induced distortion and DOI are shown in Figure 4R and compared to images with no magnetic field and no DOI added. With DOI in the model, the blurring obtained in the simulated images in 9.4T MRI has been improved a lot, and strong magnetic field does not cause any significant burring and keep the almost same image quality as the one acquired outside MRI room. Therefore, combined field-distortion model and DOI in reconstruction are all required to enable the capability of high resolution, when the SPECT system uses thicker detector (up to 5mm) and works in stronger magnetic field (up to 9.4T).

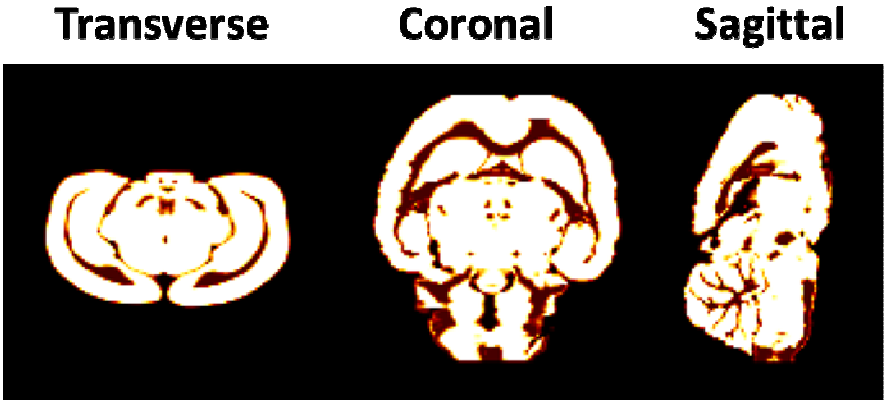

Figure 4N: 3D digital phantom from Beekman's Lab

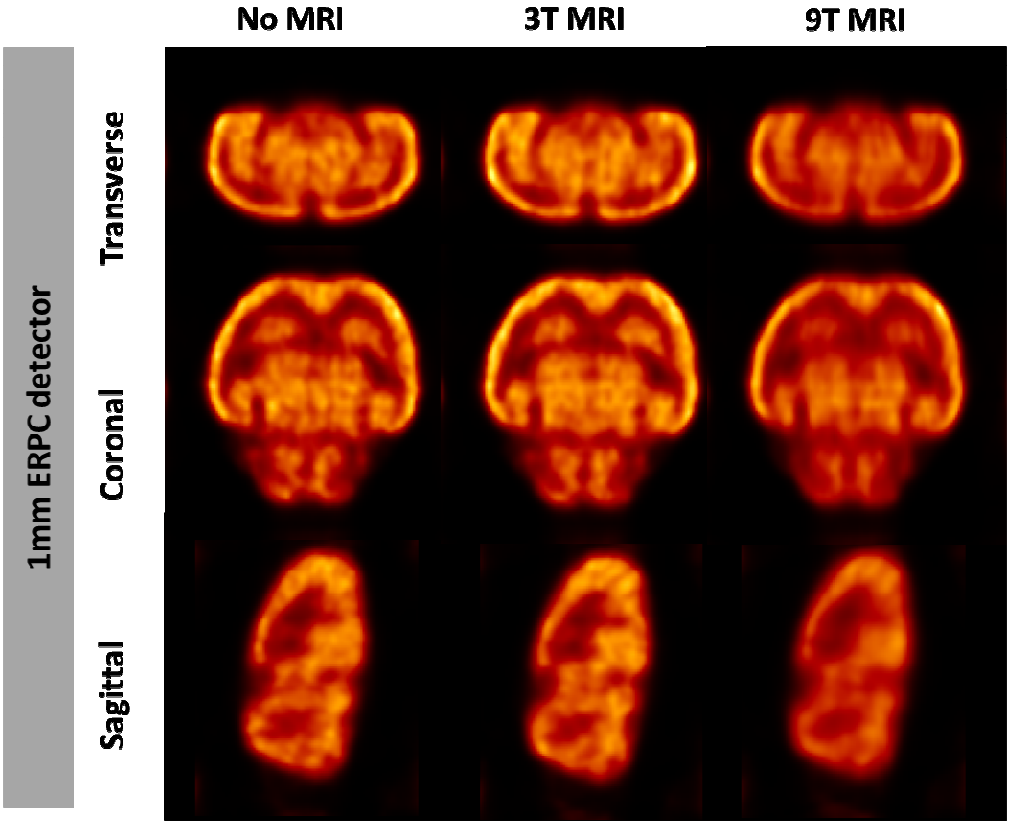

Figure 4O: Simulated images of mouse brain obtained in 0T, 3.0T and 9.4T MRI by using 1mm ERPC detector.

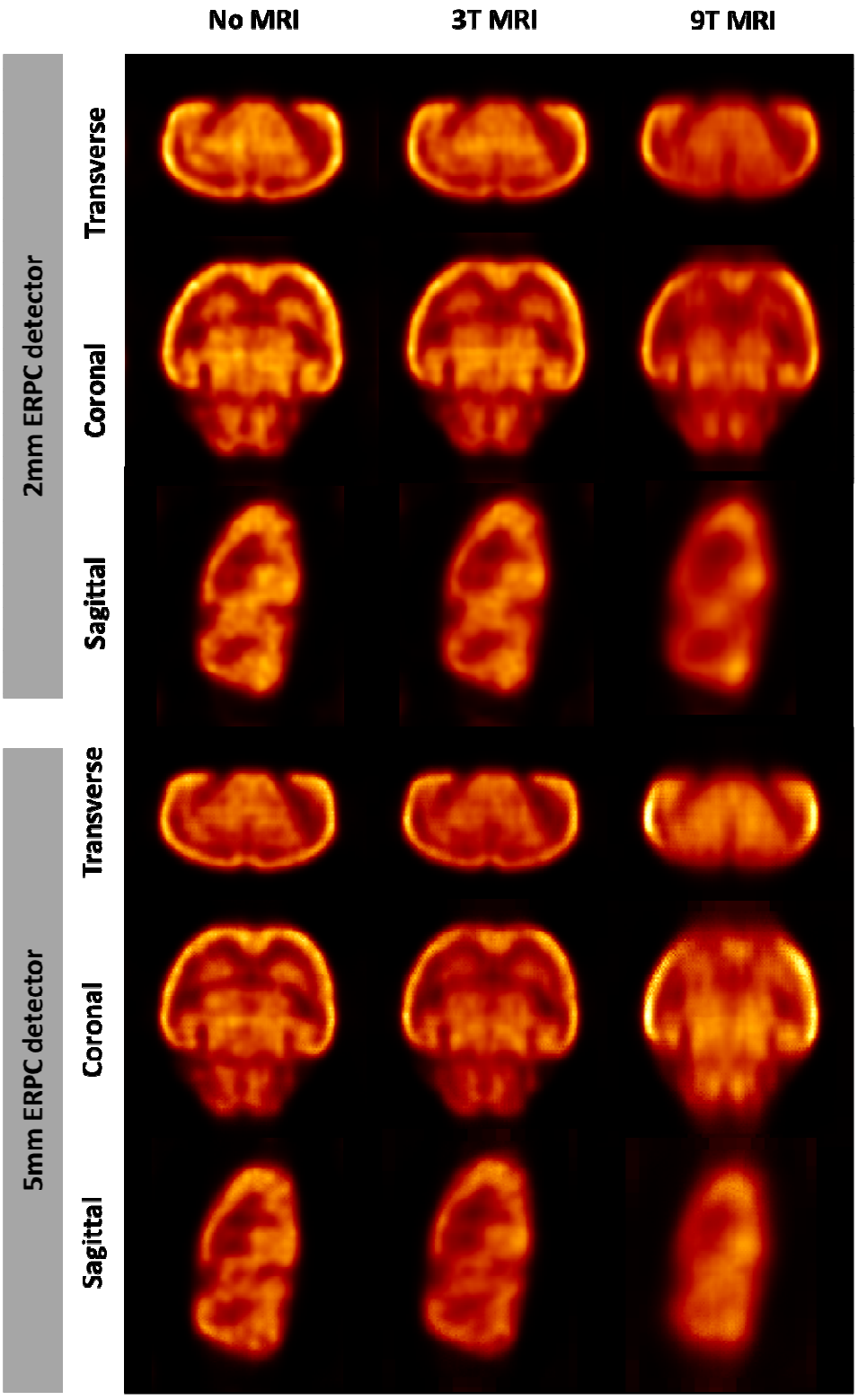

Figure 4P: Simulated images of mouse brain obtained in 0T, 3.0T and 9.4T MRI by using 2mm and 5mm ERPC detector.

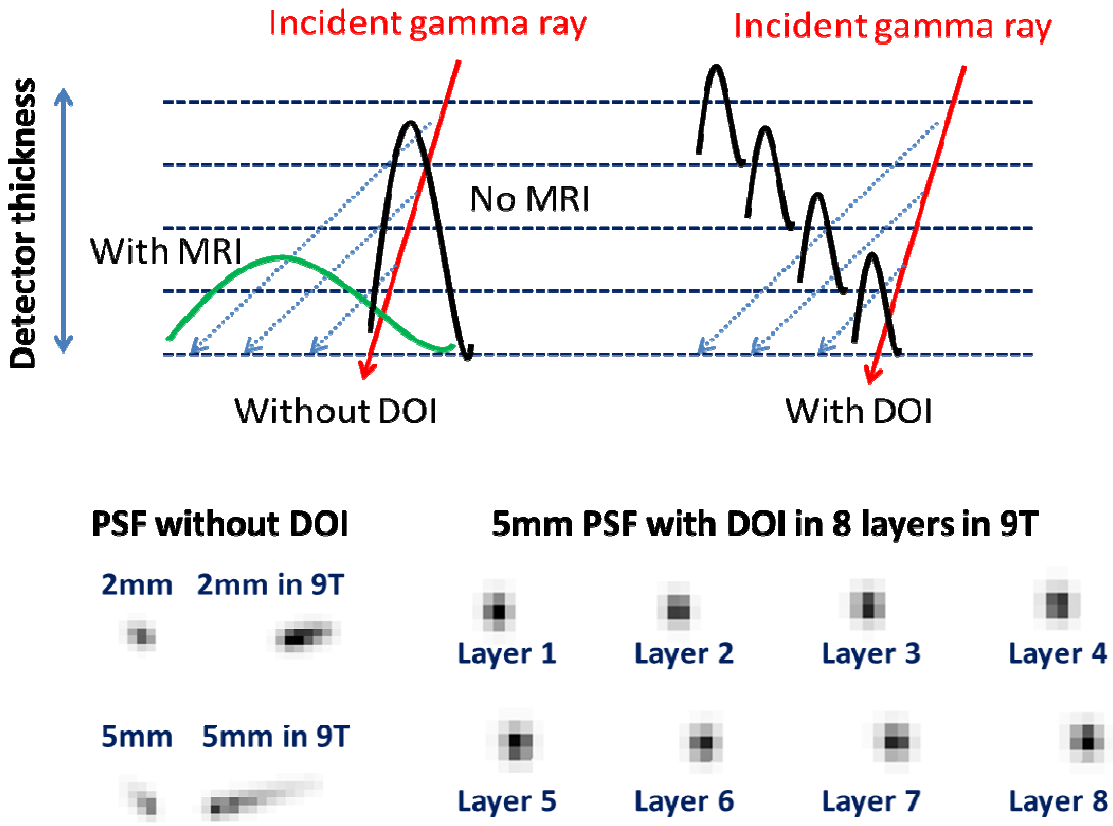

Figure 4Q: (Top) 1D point spread function with and without magnetic field and DOI; (Bottom) 2D point spread function with and without magnetic field and DOI.

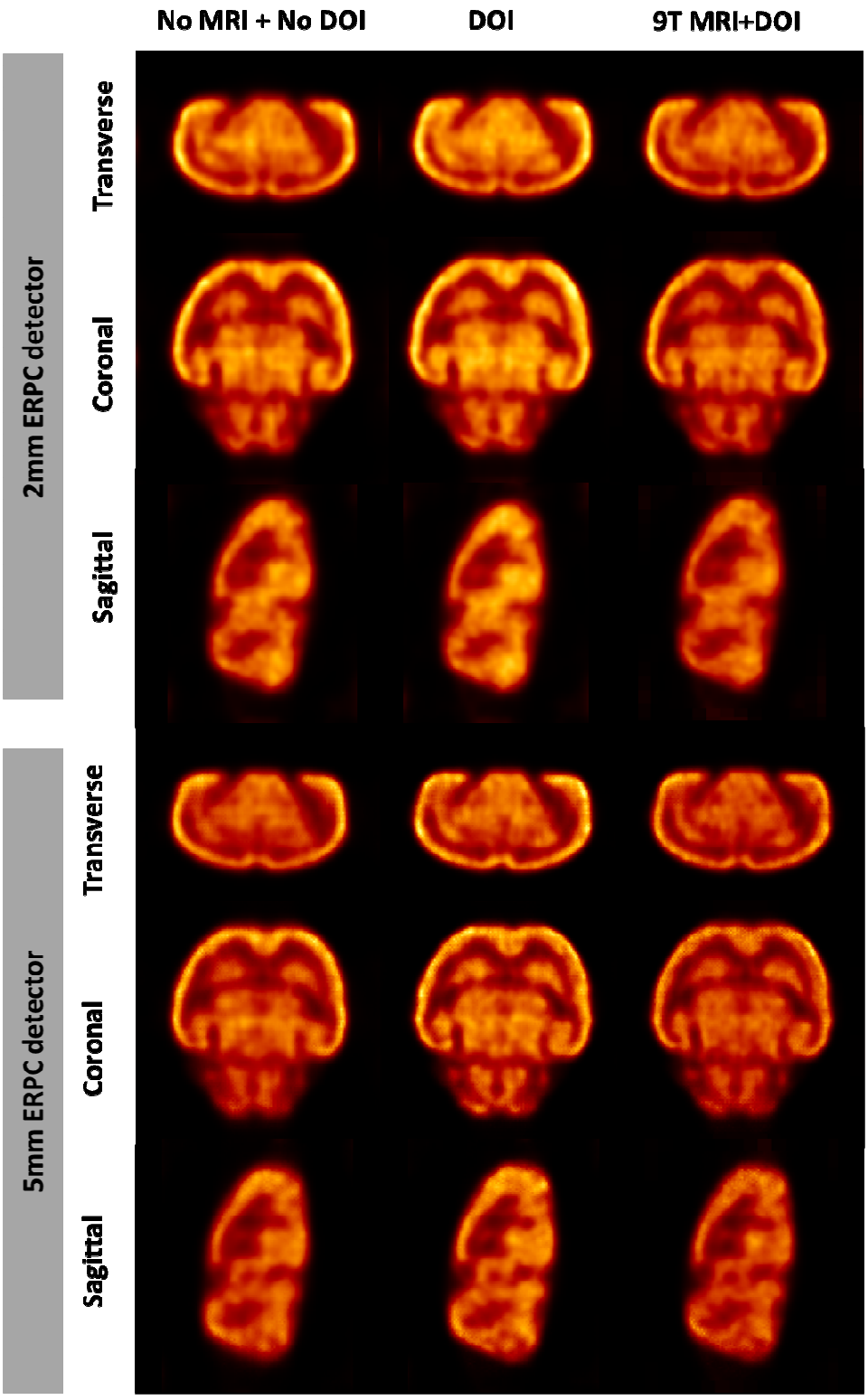

Figure 4R: With depth of interaction modeled (DOI), Simulated images of mouse brain obtained in 0T, 9.4T MRI by using 2mm and 5mm ERPC detector.

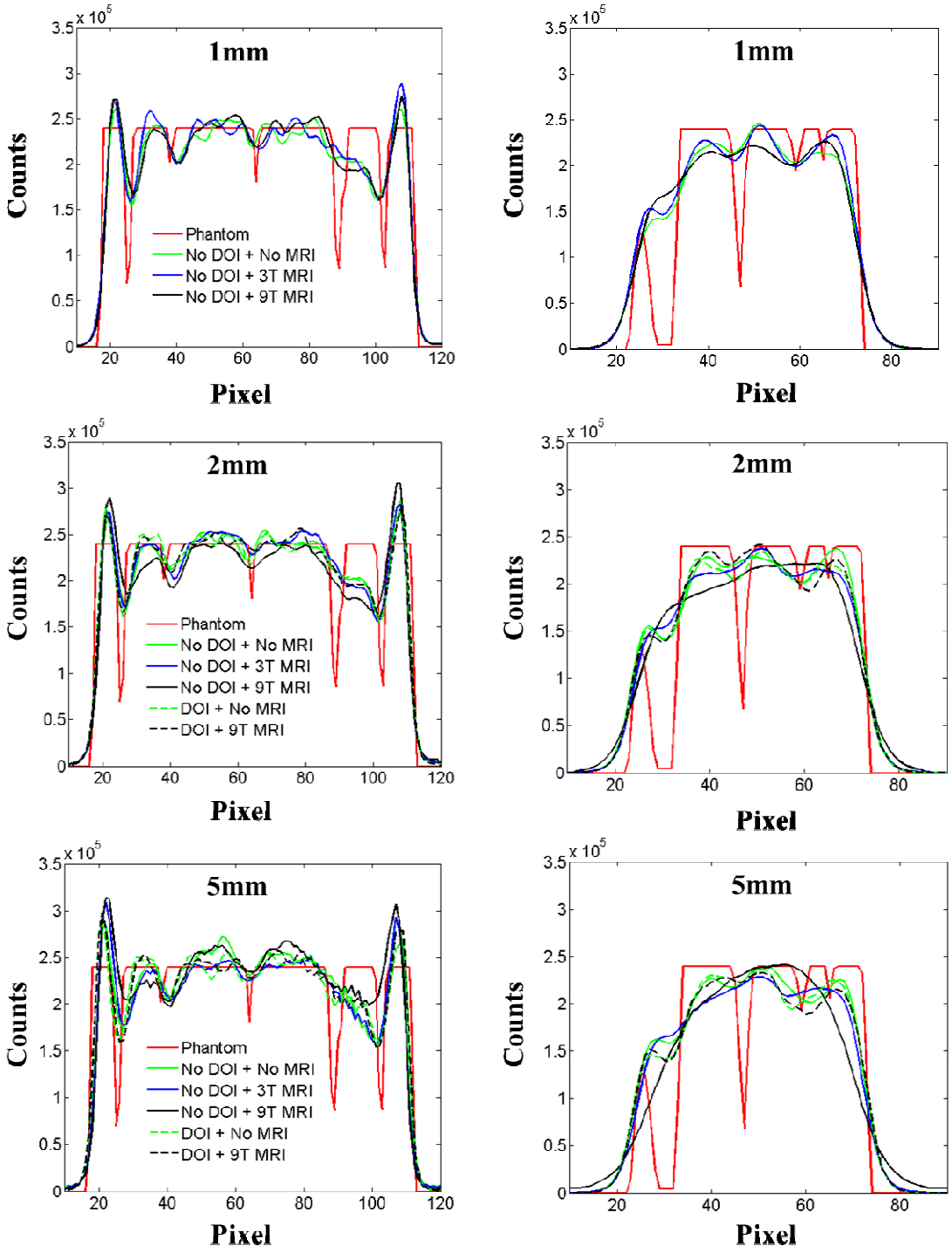

Figure 4S: One dimension profiles of reconstructed mouse brain by using 1mm, 2mm and 5mm detectors for several situations: no depth-of-interaction (DOI) and no magnetic field considered, no depth-of-interaction (DOI) and 3T magnetic field considered, no depth-of-interaction (DOI) and 9T magnetic field considered, depth-of-interaction (DOI) and no magnetic field considered, and depth-of-interaction (DOI) and 9T magnetic field considered.

4.5 Summary

This chapter is center on the derivation of comprehensive detector response function for the ERPC sensors operated inside strong magnetic field (up to 9.4T). This modeled response function includes all major physical phenomena, which include gamma ray interaction, charge generation, charge drifting with and without effect of strong magnetic field, and signal-induction process through the pre-amplifier and shaping amplifier chain.

To validate this Monte Carlo simulation model, we carried out a series of experimental measurements by using the prototype of MRI-compatible SPECT system operated inside a 3T clinical MR scanner. The experimental validation demonstrates an excellent accuracy for the modeled detector response function with different collimations used. By using this model, we are able to achieve great agreement between the measured detector response and simulated results. In addition, we used the calibrated model of detector response to predict the pinhole projection distortion for MRI-compatible SPECT system in different MR field strengths.

With this accurate model of system response in varying MR fields, we have the capability of delivering high performance SPECT images with up to 2mm in 3T MRI field. However, using thicker detector and operating in stronger magnetic field (9.4T) can cause obvious burring in reconstructed images even with distortion modeled. In this case, depth of interaction (DOI) is crucial for achieving the target spatial resolution of <0.5 mm. In practice, a DOI sensitive detector may be considered as multiple-layer CdTe detectors with single layer 0.5mm in thickness, and DOI information can be obtained with the cathode-to-anode signal ratio provided by the ERPC sensor.

To further investigate the imaging performance, the phantom study is required outside and inside 3T pre-existing MRI scanner to prove the image quality with magnetic field compensation. Some phantom study results are presented in Chapter 5.

CHAPTER 5
EXPERIMENTAL SPECT IMAGING STUDY IN 3T MRI SCANNER

In this chapter, an experimental imaging setup and some imaging studies are presented. To evaluate the imaging performance and validate the improvement with the MR field induced distortion modeled, we built a SPECT system, which contains multiple ERPC detectors, MRI-compatible collimators and non-magnetic mechanics. The detector cooling, shielding and collimation with holder are all made by non-magnetic materials. This setup allows the SPECT imaging system translation and rotation inside and outside MRI scanner. With this setup, the imaging process can be repeated outside and inside MRI scanner with the same geometry to investigate the effect of magnetic field.

In the SPECT data acquisition, point source and phantom source are used in imaging studies. The SPECT imaging is implemented by using rotating ERPC detectors around the imaging object by several steps. Both 1mm and 2mm ERPC detectors are evaluated for response in magnetic field and imaging performance in 3T MRI scanner. In addition, detector response change with presence of 3T magnetic field (first order effect) and inhomogeneity of magnetic field at different angular positions in SPECT imaging process (second order effect) is discussed in the chapter. This observed distortion is compared with the simulated prediction, and then the modeled distortion is combined into the system response function (SRF). The comparison between modeling and measurements and reconstructed images by using the normal SRF and refined SRF are presented. This SPECT imaging studies help to prove the feasibility of high spatial resolution when operated in strong magnetic field (3T) and provide critical insights for further refining the design of the MRI-compatible SPECT system for more biomedical applications.

5.1 MRI-compatible SPECT system based on ERPC detectors

The precision of the detector response and capability of predicting image distortion induced by strong field has been demonstrated by the last chapter. Imaging studies are needed to further confirm the performances of MRI-compatible SPECT system. The system uses ERPC detectors with 1mm and 2mm thick CdTe crystals, which are fixed on a non-magnetic housing (as Figure 5A) [57] [58].

In this setup, ERPC detectors are mounted in a Carbon fiber gantry, which can be remotely controlled by a non-magnetic rotation stage and can be fully inserted into MRI scanner (as Figure 5A). All mechanics are fixed on a specially made Aluminum cart for translation in MRI room. Each detector is coupled to a multiple-pinhole aperture, which is proved MRI-compatible in our previous study. A heat sink is attached on the backside of each detector for cooling by compress air. The operation temperature of the detector is around 25-28 degree. All power supplies and host PC are located outside the MRI room and connected to the detectors by cables with 10 meters in length. In this setup, the collimator has multiple pinholes of 200 μm or 400 μm in diameter and the pinhole distance is 7mm. Both aperture-object and aperture-detector distances are around 3.2 cm. The photo and the 1mm- 2mm ERPC CdTe detector and used pinhole apertures are shown in Figure 5B and 5C.

The image quality and spatial resolution improvement with field-induced distortion modeled are also verified by point source and phantom studies. Tomographic images of 100μCi sphere source and micro-Jaszczak resolution phantom [59] are acquired to evaluate the potential interference between modalities and imaging performance of SPECT. The resolution phantom we used is filled with Tc-99 up to 5mCi activity, which contains the features from 1000 μm to 350μm in diameter. Eight angular positions are set in 360 degree SPECT imaging and the total scan time is around 2 hours. The same SPECT imaging is repeated inside MRI, and the reconstruction is carried out sequentially with ordered-subset penalized maximum likelihood (OSEM) algorithm [60] [61]. The reconstructed images obtained by 1mm and 2mm detector are presented in chapter 5.3.

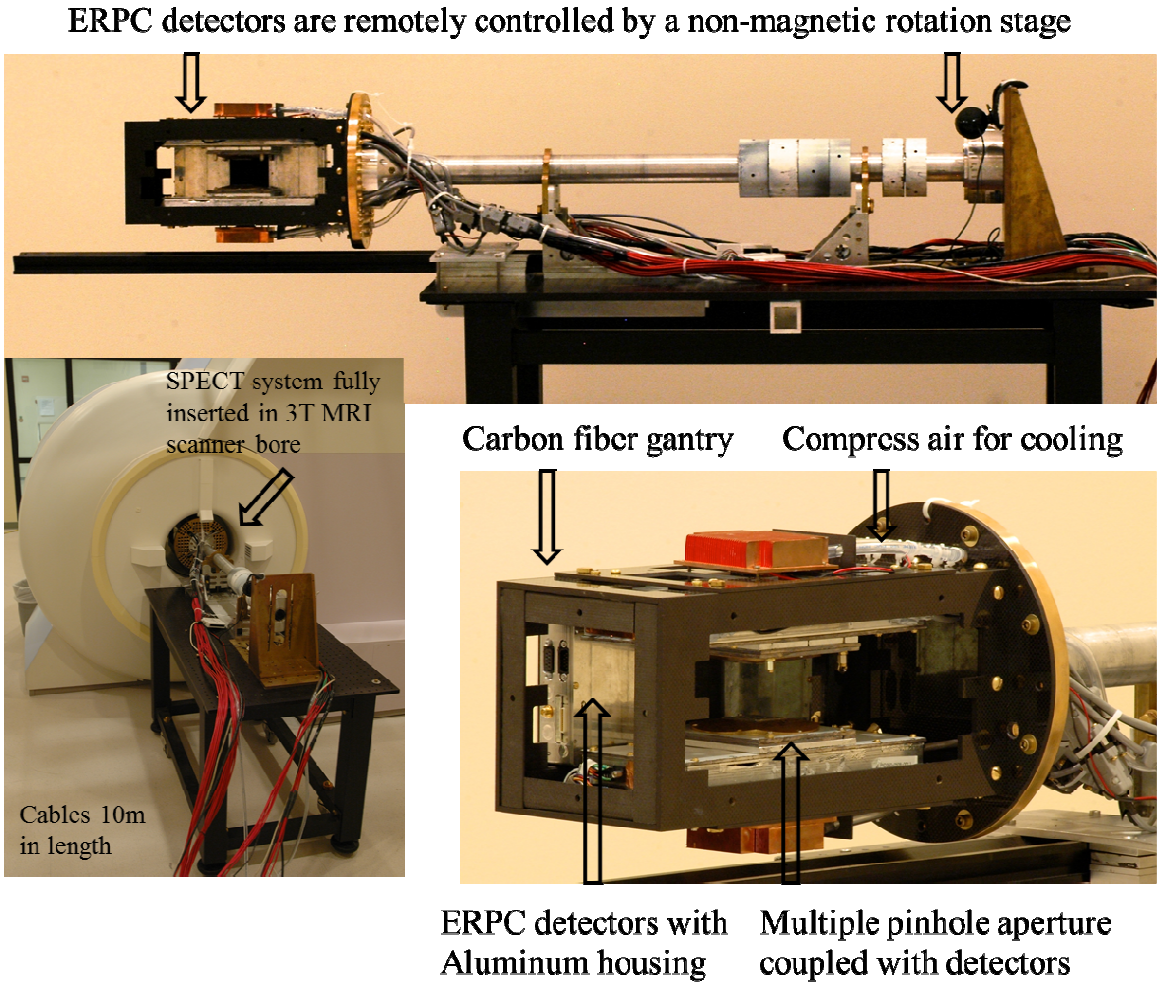

Figure 5A: Experimental SPECT setup based on the ERPC detectors arranged with ring configuration. Detectors supported in a Carbon fiber gantry and controlled by a non-magnetic rotation stage.

In the reconstruction process, the acquired projections of ERPC detector only consider the count in the photo peak of 122kev or 140kev. As discussed in the last two chapters, the effect of strong magnetic field on the SPECT projection and images is a key issue for high-resolution images. The quantify the distortion, we used a fixed source-collimator-detector assembly outside and inside MRI scanner, and obtained the projection shift of fixed source covering all angular positions in real SPECT imaging process, which needs to be modeled and compensated in reconstruction process, described in chapter 5.2.

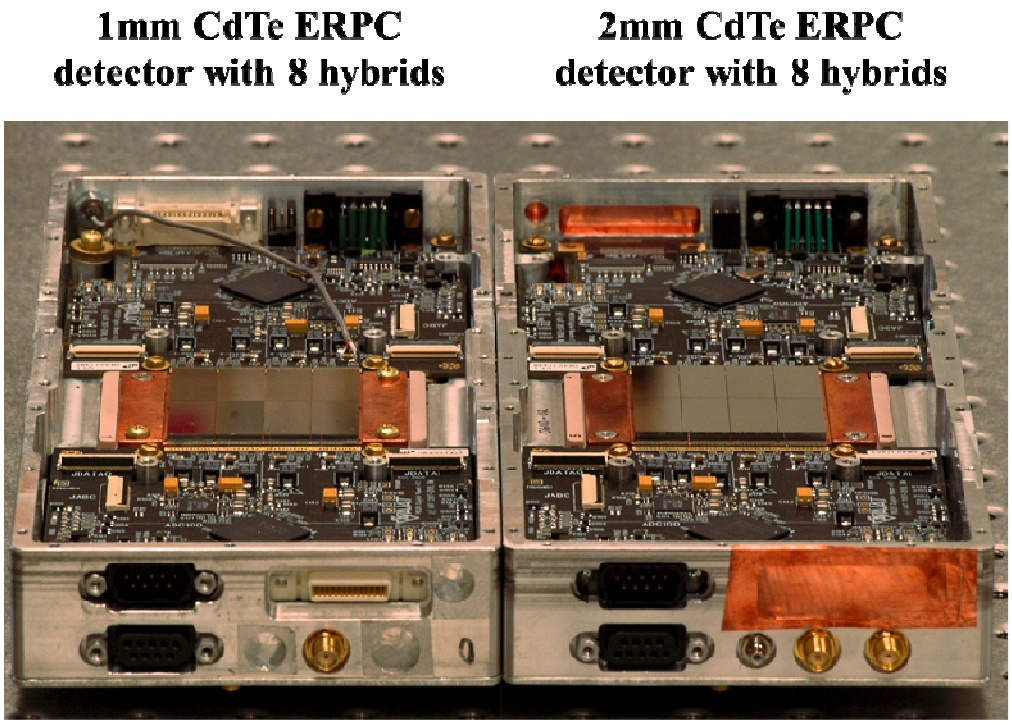

Figure 5B: Photo of 1mm and 2mm CdTe ERPC detectors in Aluminum housing used in the current experimental setup as Figure 5A.

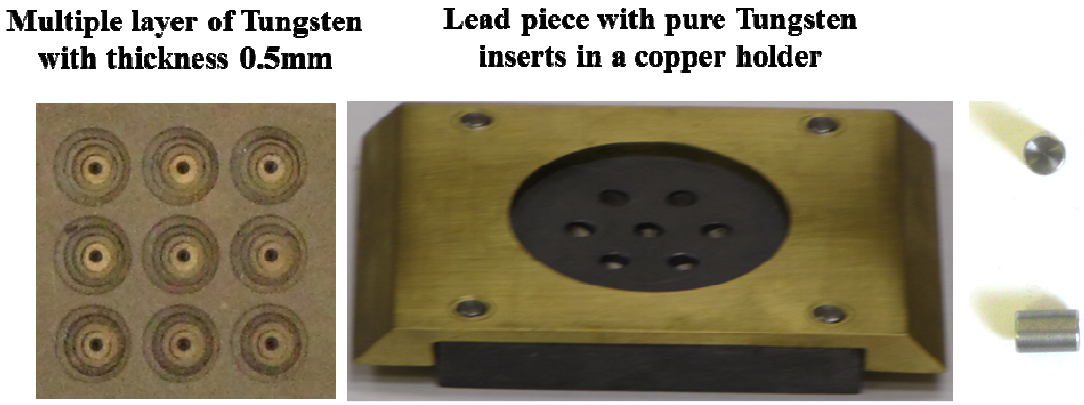

Figure 5C: Two pinhole apertures used in SPECT imaging process: 1) nine pinhole aperture made up with nine pieces of Tungsten with thickness 0.5mm each (left); 2): 6mm thick pure Lead collimator (middle) with Tungsten inserts (right).

5.2 Modeled detector response with first- and second- order effect

In Chapter 4, we highlighted the effect of the main magnetic field on the performance of a prototype SPECT system. This effect is originated by the Lorenz force exerted on charge carriers migrating inside the ERPC detector, which is referred to as the first-order effect of the magnetic field on SPECT images. We have also demonstrated that adding the modeled distortion in reconstruction process can compensate this effect. However, the magnetic field also poses the second-order effect on the SPECT detectors. This is due to the inhomogeneity of magnetic field that is introduced by the presence of metal parts inside the MR scanner. Therefore, SPECT detectors placed at different locations inside the MR scanner suffers from different amount of distortion. To demonstrate this effect, we used a pinhole aperture set between a single ERPC detector and fixed Co57 point source, and rotated the whole detection system in 360 degree with 15 steps. If only the first order effect is considered, the projection shifting should be unchanged when rotating in the MRI scanner, because the relative detection geometry are unchanged during rotation. In Figure 5D, we plotted the centroid positions of the projections of the source through a single pinhole at 15 angular steps inside and outside MRI. It is clearly shown that the projections of the fixed point source have been shifting by different distances towards different directions. The average distance between the projections outside and inside strong magnetic field is around 150μm, but the maximum distance among the projection positions acquired inside MRI is also around 150μm. This demonstrates the second order effect due to the inhomogeneity of magnetic field. If not correctly compensated, this effect would lead to extra burring in SPECT images and degradation in spatial resolution.

Since the second order effect is related to the presence of the metal parts used for SPECT in MRI, we tried other non-metal materials to replace metal parts in SPECT system and tried to construct the SPECT system as symmetric as possible, although these can not solve the problem completely. We repeated the same measurements with the same fixed source pinhole geometry but two detectors placed symmetric in MRI scanner, and comparison centroid positions are displayed in Figure 5F. The average distance between the projections outside and inside strong

magnetic field is still around 160µm, but the maximum distance among the projection positions acquired inside MRI is much less than 150µm (20µm -30µm). However, a more thorough approach would be to determine both the first- and the second-order effects experimentally and to build this information in SPECT reconstruction process. For this purpose, we can use a fixed point source placed in the field-of-view of the SPECT system and rotate the entire setup inside the MR scanner to cover the angular positions that are used in true SPECT imaging. This measurement can be repeated with the SPECT system outside the MRI scanner. By comparing the projections measurement inside and outside the magnetic field, we can derive the first- and second-order effects in terms of a projection-shifting function. This projection-shifting function can be modeled by Monte Carlo simulation and convolved with the normal response function that does not include a magnetic field. This process can give rise to a compressive detector response function that could be used in reconstruction to compensate the combined effects of the strong magnetic field on SPECT imaging.

In the simulation model, the combined first and second order effect of strong magnetic field is considered as electron and holes drifting shift under Lorenz force in 3D dimensional space. With the known gamma ray incidence information by geometry calibration, charge carriers drifting direction as a function of angular positions is calibrated to fit the measurements, and the pinhole projections modeled with fitted charge carrier drifting process are compared with measured projections. Some comparison results are shown in Figure 5G and 5H, and the centroid positions of measured and modeled projections are shown in Figure 5F, in which optimized position error is less than 30µm.

5.3 SPECT images obtained in 3T MRI with the combined first- and second-order correction in reconstruction

The Ø250µm sphere source (100µCi) and resolution phantom filled with Tc-99m solution are

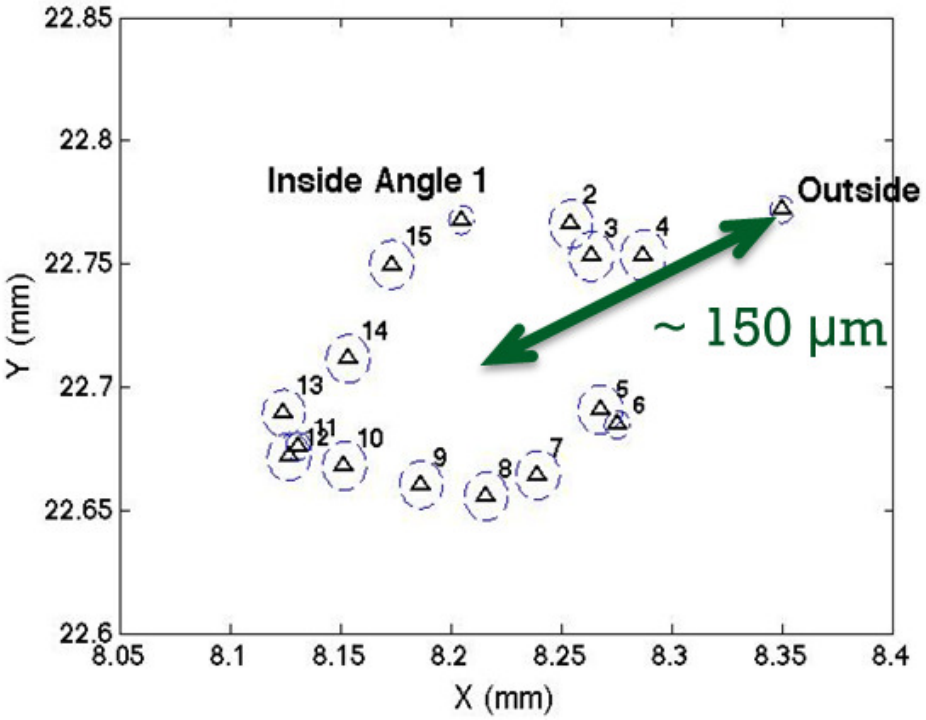

Figure 5D: centroid positions of the projections of the source through a single pinhole at 15 angular steps inside and outside MRI (Single detector detection system).

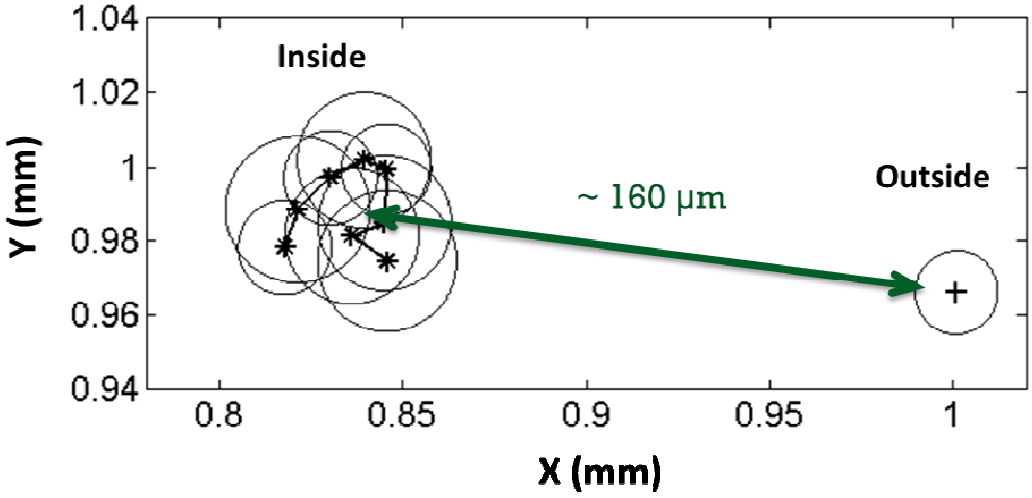

Figure 5E: centroid positions of the projections of the source through a single pinhole at 15 angular steps inside and outside MRI (Two detector system with symmetric detection setup).

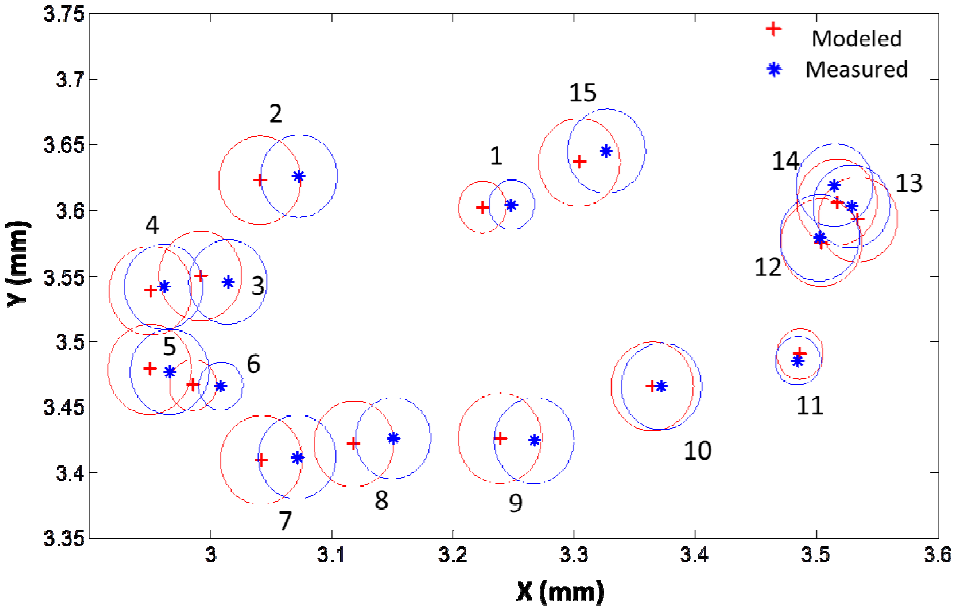

Figure 5F: Measured and modeled centroid positions of the projections of the source through a single pinhole at 15 angular steps inside MRI.

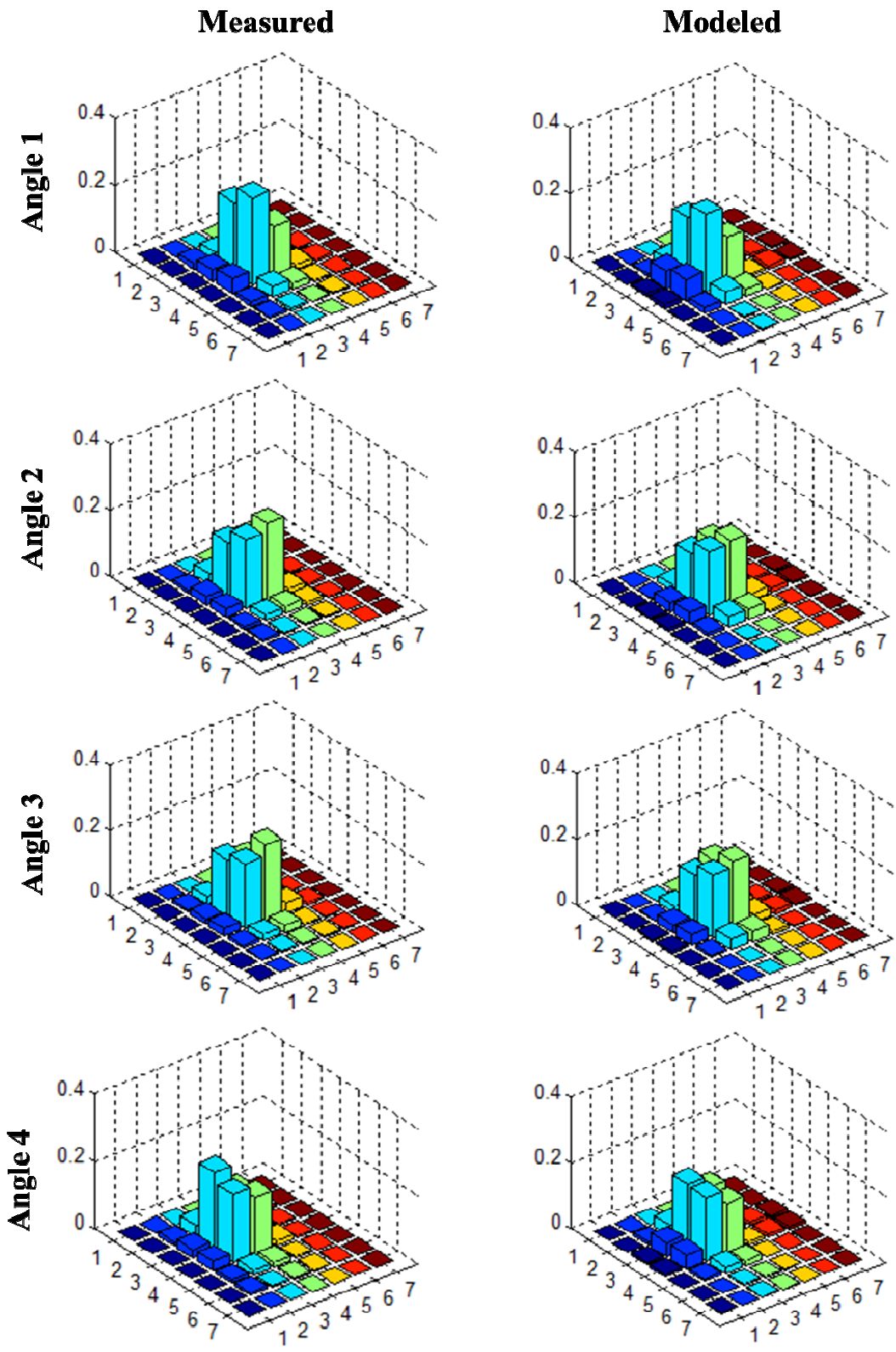

Figure 5G: Modeled and measured eight projections of fixed source obtained at angular positions 1-4.

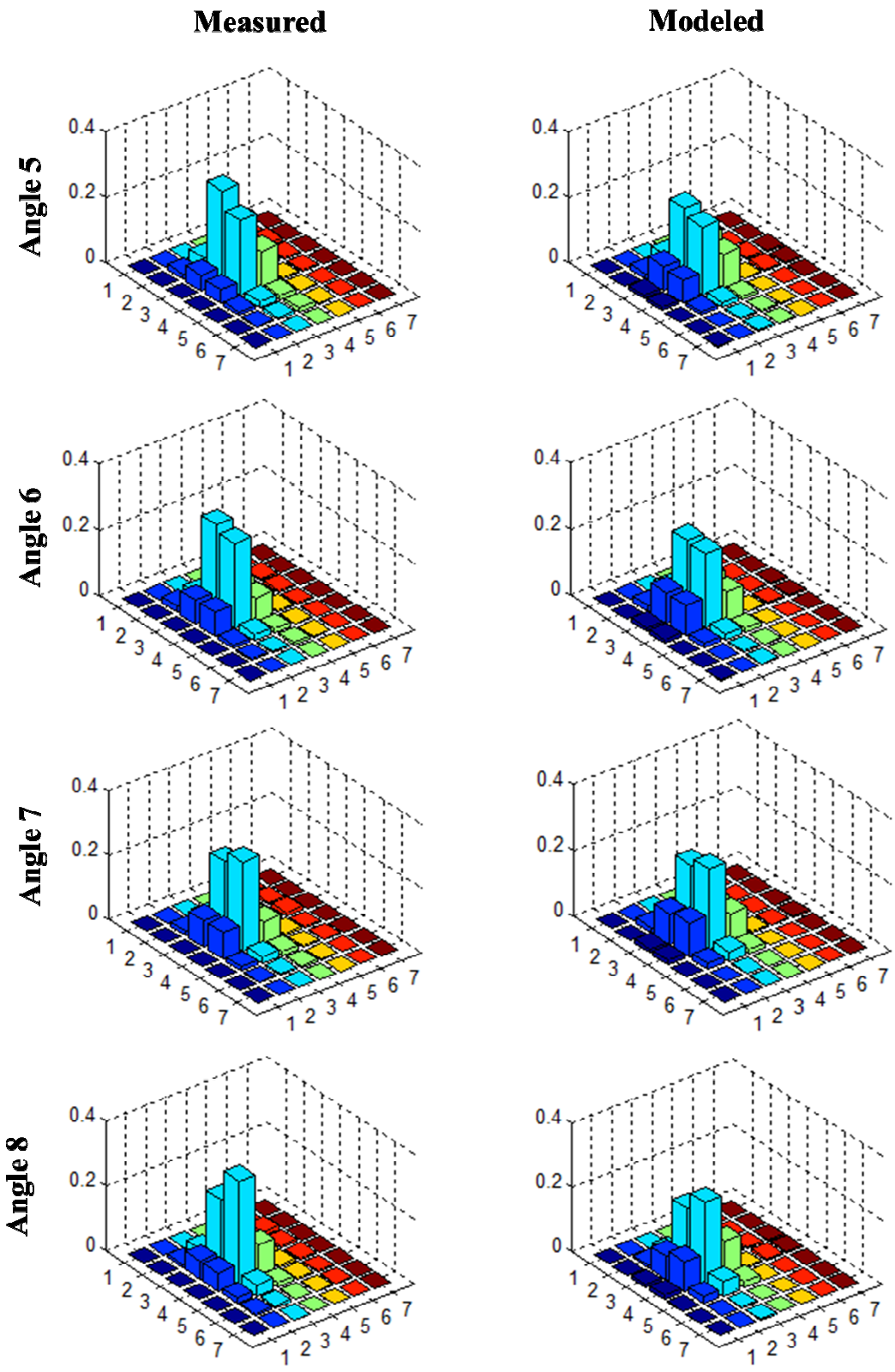

Figure 5H: Modeled and measured eight projections of fixed source obtained at angular positions 5-8.

used in SPECT imaging to investigate the performance of our SPECT system in strong magnetic field. The experimental results with and with no magnetic field considered can help to prove the system operation in strong magnetic field and accuracy of charge collection model in the last chapter.

The projections of point source are acquired by 1mm and 2mm in 360 degree at eight angular positions. The total imaging time is 80 minutes. The same imaging is repeated outside and inside 3T MRI scanner. As mentioned in this chapter, the strong magnetic field affect the charge collection process and thus lead the distortion in projection and reconstructed images. But if this distortion can be modeled in the system response function (SRF), the blurred images can be recovered, which was confirmed by 1D and 2D reconstructed images of 1mm and 2mm ERPC CdTe detectors (as shown in Figure 5I-5L).

With no effect from magnetic field the FWHM of reconstructed Ø250μm sphere source can be less than 200μm with 100μm source voxel size. Then the system is inserted into MRI with rotation axis parallel to the MRI axis. The field induced blur can only be obtained perpendicular to the direction of the magnetic field but no distortion along the magnetic field, so the image of sphere source is expanded in particular directions, which is more significant in thicker detector due to the longer charge drifting with Lorenz force. By adding the modeled distortion to refine the SRF, the reconstruction process is repeated with the same projection data, and the sphere source can be recovered, 2mm detector especially. The FWHM of reconstructed point source with newly refined SRF is improved a lot, which is closed to the values obtained outside MRI and less than real diameter of the sphere source (250μm).

The SPECT image of resolution phantom filled with 2.5mCi Tc-99m is obtained outside and inside MRI scanner as shown in Figure 5M. When the field-induced distortion included in the system response function, the 500μm features can be recovered. This can be resolved in image outside MRI but not in the images reconstructed with normal system response function. This improved image quality and spatial resolution confirm the imaging performance of our MRI-compatible SPECT system.

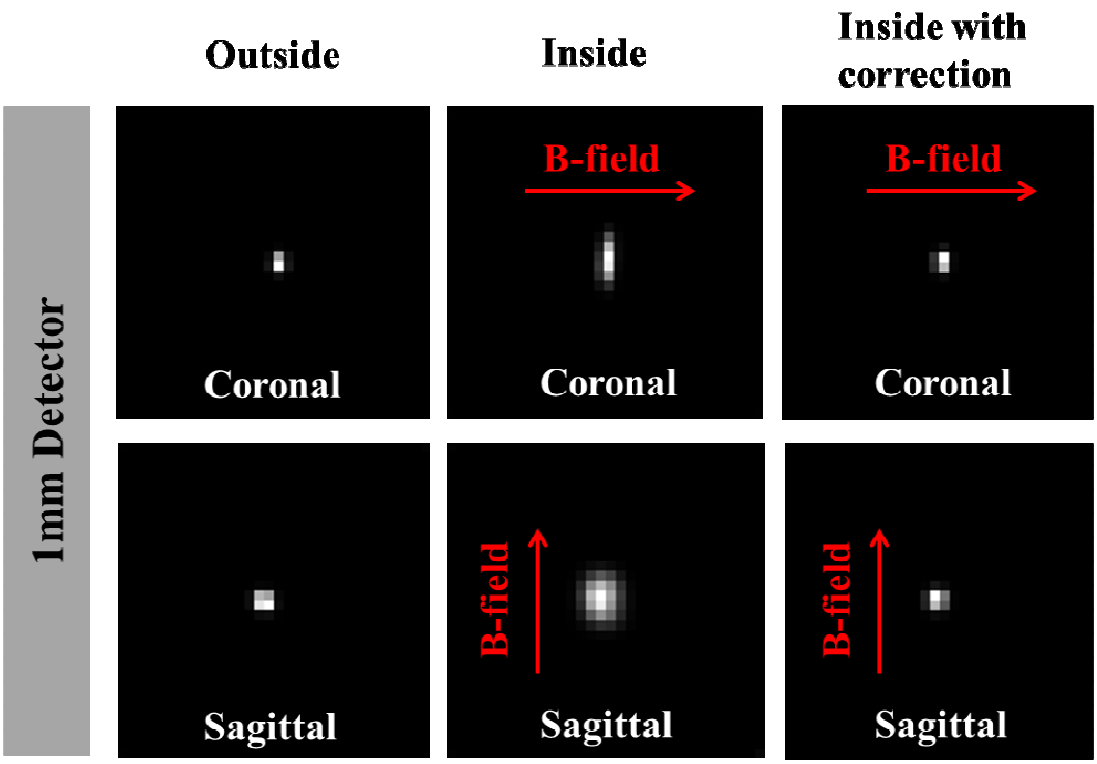

Figure 5I: 2D reconstructed images obtained by 1mm ERPC detector outside 3T MRI (left column), inside MRI without modeled field-induced distortion, and inside MRI with modeled field-induced distortion.

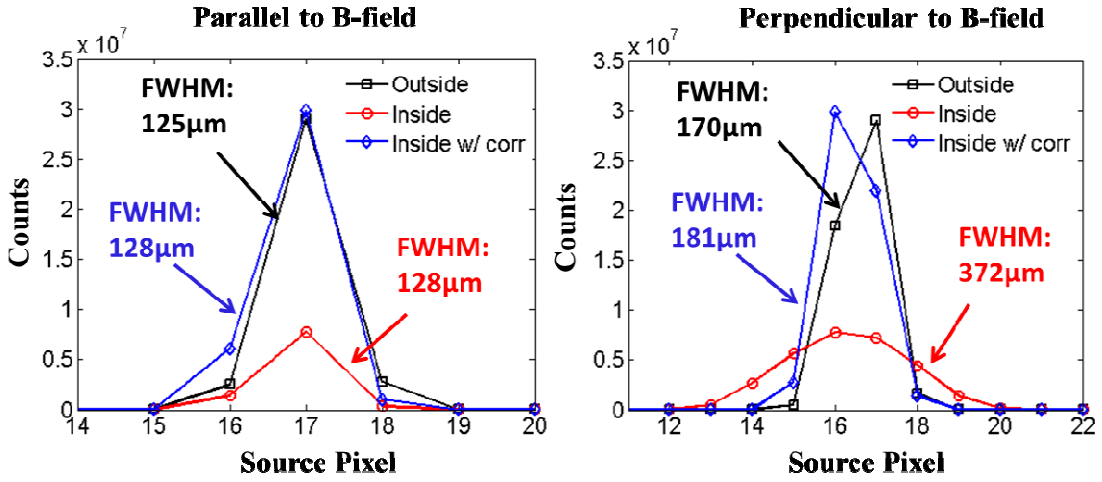

Figure 5J: Two 1D profiles of reconstructed images obtained by 1mm ERPC detector outside 3T MRI (left column), inside MRI without modeled field-induced distortion, and inside MRI with modeled field-induced distortion.

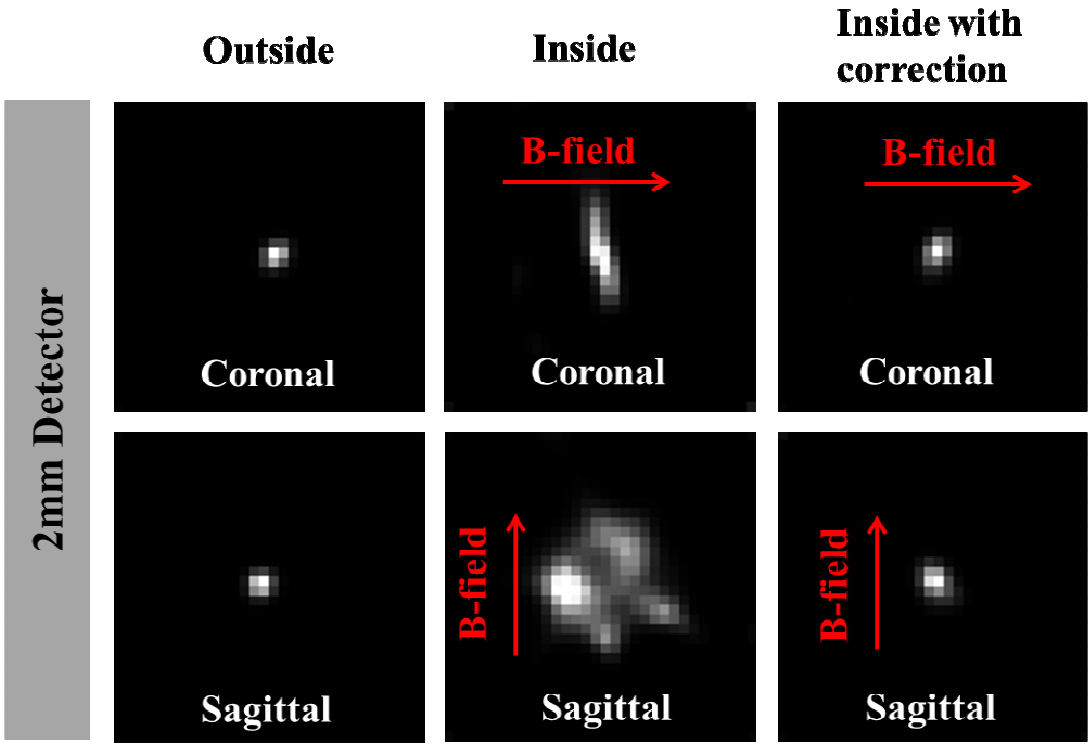

Figure 5K: 2D reconstructed images obtained by 2mm ERPC detector outside 3T MRI (left column), inside MRI without modeled field-induced distortion, and inside MRI with modeled field-induced distortion.

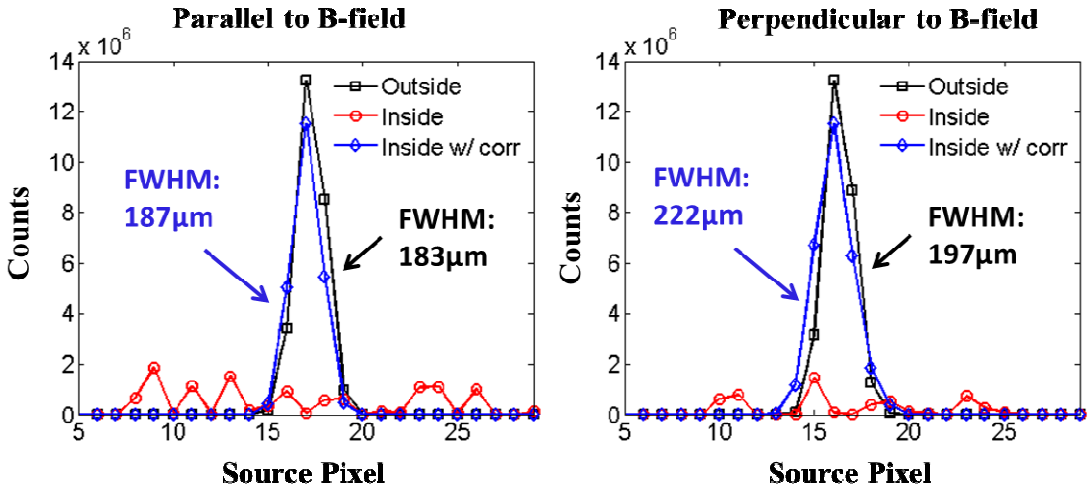

Figure 5L: Two 1D profiles of reconstructed images obtained by 2mm ERPC detector outside 3T MRI (left column), inside MRI without modeled field-induced distortion, and inside MRI with modeled field-induced distortion.

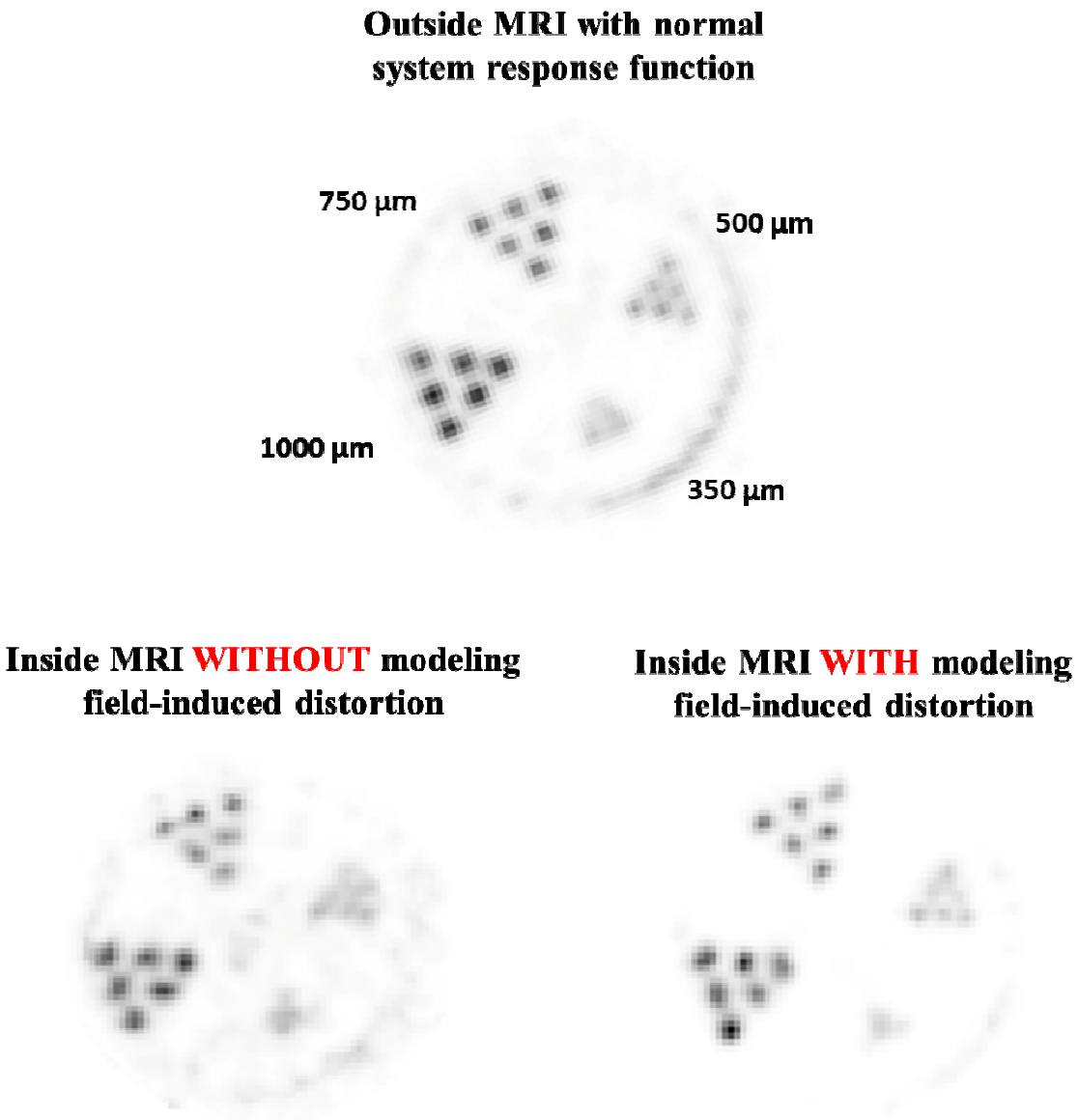

Figure 5M: Images obtained by 1mm ERPC detector outside MRI scanner with normal system response function (Top), inside MRI with normal system response function (Bottom left) and), inside MRI with field-induced distortion included system response function.

5.4 Summary

In this paper, we presented a study of a MRI-compatible high spatial resolution SPECT system based on the 1mm and 2mm thick energy-resolved photon counting CdTe detector. With the modeled distortion of magnetic field, the detector can provide an excellent spatial resolution down to ~500μm. To evaluate this compatibility and performance of SPECT system in the MRI (3.0 Tesla) scanner, we investigated several related technical issues, which are summarized as below:

Firstly, given the relatively large detector thickness (1-5 mm), the collection of charge carriers, are affected by the Lorenz force (first-order effect). This leads to an increased probability for charge sharing and event positioning error as previously discussed. Secondly, with the presence of our SPECT detectors, electric shielding material and various heavy-metal parts of apertures and supporting gantry in the magnetic field, it may cause that a reasonably small interference on SPECT detector can be maintained with the proposed system design, such as the inhomogeneity of magnetic field. This inhomogeneity of magnetic field that is introduced by the presence of metal parts inside the MR scanner can contribute extra burring in SPECT imaging process (second-order effect). This combined effect is modeled and compared with the measurements. An agreement is achieved and the effect is compensated in reconstruction as discussed in chapter 5.2 and the reconstructed images with first and second order compensation are shown in chapter 5.3, which confirms the improvement of the qualities and spatial resolution of images obtained in strong magnetic field.

The MRI-compatible SPECT system has a capability of delivering high spatial resolution (<500μm) when operated in strong magnetic field. One can therefore correlate the complementary information from both systems for in vivo mouse brain imaging, and make combined systems used in many imaging applications. In the future system design, we have to consider technical issues of using the detector with thicker detector for high-energy SPECT tracer in stronger MRI scanner. For that purpose, in particular, depth-of-interaction (DOI) information is needed to extrapolate the SPECT distortion compensation for thicker detectors (up to 5mm) or in

the strong MRI scanner (up to 9.4T). In addition, due to the space limit inside MRI scanner, more compact detector is under development that allows detector ring configuration with 6-8 detector modules in MRI scanner for many applications.

CHAPTER 6
CONCLUSIONS

In this developed MRI-compatible SPECT system, we used the Energy-Resolved Photon Counting (ERPC) pixel CdTe detector. This detector is designed based on hybrid detector concept, and CdTe/CdZnTe crystals in varying thickness are used in ERPC detector prototype. The detector prototype is made up of eight standard hybrids closely packed to provide 4.4cm×4.4cm detection area. Each detector hybrid module (CdTe) has array of 32 ×64 square pixels with pitch size 350μm× 350μm and anode size 300μm× 300μm. The CdTe and CdZnTe detector shared the same ASIC design, which is equipped with pre-amplifier, shaper, comparer, peak-hold circuitry discriminator and ADC. To evaluate the performance of the detector, we investigated the detector uniformity and energy resolution with the multiple open isotopes, and 4-5kev energy resolution @122kev has been proved experimentally. This energy resolution and the intrinsic spatial resolution (350 μm) allow the excellent SPECT performance with use of multiple low-energy SPECT tracers, such as I-123, Tl-201 and Tc-99. In addition, the ERPC detector uses standard detector module, which allows any detector size needed in multiple compact SPECT system.

By using this detector prototype in SPECT system, we presented some preliminary experimental results obtained by this high spatial resolution SPECT system. A series of studies, such as energy resolution, detector uniformity, charge sharing and imaging quality, are performed to investigate the performance of the detectors and the SPECT system. In order to achieve the goal of obtaining good energy resolution inside the MRI scanner, we measured energy spectra and demonstrated that the ERPC detector could reliably work inside the 3.0T MRI scanner. This detector can provide an excellent energy resolution of around 4keV and an intrinsic spatial resolution of 350μm for gamma rays @140keV in the pre-existing 3.0T MRI scanner.

However, to operate the SPECT system inside MRI bore, it raises several concerns when placing a high-resolution semiconductor sensor inside a strong magnetic field. The interference between the two imaging modalities may degrade the image quality. Firstly, the SPECT detector

and other metal parts in the system may affect the homogeneity of magnetic field. Besides the interference from the metal parts of the gantry, the eddy current induced by varying magnetic field on the large cathode plane and readout circuitry leads an increased noise level. To minimize the interference, we reduced the metal material used in system, and confirmed the compatibility of system in MRI. Secondly, when a detector is in use inside MRI bore, the collection of charge carriers, projections and the images are still affected by the Lorenz force. Therefore, a relatively larger detector thickness (ex. 2-4 mm) leads to an increased probability for charge sharing, event positioning error and image blur. For achieving an ultrahigh spatial resolution, the field-induced event-positioning error appears to be a critical issue that needs to be solved for achieving the target resolution (300-500μm). One of the most straightforward methods to solve this issue is to add the charge collection process with effect of magnetic field in the system response function (SRF) of SPECT, which helps to compensate the broadening or blur of the image acquired inside the MRI and allow capability of high spatial resolution. This procedure provides a more accurate modeling of all the important physical processes inside MRI, which should allow one to account for the event positioning error caused by magnetic field.

To predict the effect from the MRI-based magnetic field in pixel detector response, we built a Monte Carlo simulation mode to derive a comprehensive detector response function for the ERPC sensors when operated inside strong magnetic field (up to 9.4T). This modeled response function includes all the major physical processes, including gamma ray interactions, charge generation and drifting with and without strong magnetic field, and signal-induction process through the pre-amplifier and shaping amplifier chain. In addition, we carried out a series of experimental measurements to calibrate this model by using a prototype MRI-compatible SPECT system. This validation demonstrates an excellent accuracy for the modeled spatial and spectroscopic response function of detector with multiple collimations applied. By using this model, we were able to achieve great agreement between the measured and simulated responses results, and predict the pinhole projection distortion for SPECT systems in different field-strengths (up to 9.4T).

With this accurate model of system response as a function of MR-field strength, we simulated

the SPECT image of mouse brain by using detectors (1-5mm thick) in different magnetic field (3.0 and 9.4T). The simulated images prove the capability of delivering high performance SPECT images with up to 2mm detector in 3T MRI field. However, using thicker detector or operating in strong magnetic field (9.4T) cause the reconstructed images suffering from obvious burring even with distortion modeled. In this case, depth of interaction (DOI) is crucial for achieving the target spatial resolution of <0.5 mm for thick detector or in very strong magnetic field. In practice, a DOI sensitive detector may be considered as multiple-layer CdTe detectors with 0.5mm in thickness for each layer. The image of the same phantom is simulated by adding DOI in system response function, and compared with the images with normal system response function. Even the images obtained by the thickest detector in the strongest field have been improved a lot. In principle, DOI information can be experimentally obtained with the cathode-to-anode signal ratio of detector, and provide the depth position resolution around 0.5mm.

Finally, we presented an imaging study of a MRI-compatible high spatial resolution SPECT system based on the 1mm and 2mm thick energy-resolved photon counting CdTe detector system. The image reconstruction includes the model of the field-induced distortion. This process can successfully compensate the event positioning error in reconstruction. In the SPECT imaging, Lorenz force (the first order effect) is not only effect considered. With the presence of our SPECT detectors, electric shielding material and various heavy-metal parts of apertures and supporting gantry in the magnetic field, it may cause that a reasonably small interference on SPECT detector can be maintained with the proposed system design, such as the inhomogeneity of magnetic field. This inhomogeneity of magnetic field that is introduced by the presence of metal parts inside the MR scanner can contribute extra burring in SPECT imaging process (second-order effect). This combined effect is modeled and compared with the measurements to provide an excellent spatial resolution for point source (<250 μm) and resolution phantom (~500μm) in 3T field. Therefore, this experimental study confirm that our SPECT system enable to provide high quality images in strong magnetic field, and one can correlate the complementary information from MRI and SPECT for in vivo imaging applications.

In the furfure MRI-compatible SPECT system design, we investigated several related technical issues, which are summarized as below:

Firstly, we have to consider the next SPECT system with more detectors in ring configuration, which can avoid the detector rotation inside MRI during scanning. More compact detector under developing allows detector ring configuration with 6-8 detector modules in MRI scanner for more applications in small animal imaging studies. For that purpose, more compact design for ERPC detector is needed. In particular, the current housing of the detector prototype is relatively large, because two digital PCBs are placed at both sides of crystals. The setup make the overall size of the detector housing is much larger than the detector modules (4.4cm×4.4cm) as Figure 2I. We are developing next generation detector with digital readout placed on the backside of the detector modules, which reduces the overall size of the detector.

Secondly, although, the prototype of the ERPC detector has exhibited promising performance for gamma ray imaging, there are several keys for further improvements. Small amount of pixels do not work due to some manufacture process, especially the CdZnTe detector with larger inter-pixel gap size. We are still investigating the possible causes and solutions for the bad pixels to change the uniformity of all pixels in detector. Also depth-of-interaction is needed for thicker detector, which can be derived based on the cathode and anode signals. The cathode signal can be read out by discrete amplifier and A-to-D. In the future detector design, the DOI information needs to be considered and implemented to provide 3D positions of events. With DOI information, the SPECT imaging response function could be refined to accurate the SPECT distortion compensation for thicker detectors (up to 5mm) and to achieve the better spatial resolution, and this improvement is more obvious when operated in strong magnetic field (up to 9.4T).

This proposed MRI-compatible SPECT system allows a near ideal co-registration between the very-high resolution functional SPECT images and MR images with excellent tissue contrast. The SPECT scanning setup needs to be refined by adding more detectors inside the magnetic field for image studies. The charge shifting and collection based on magnetic field can be further modeled to quantify the distortion for each detector unit. Continued with this study, more small animal

studies are needed to further explore the interference between SPECT and MR systems, but this work demonstrates the feasibility simultaneous imaging of SPECT and MRI systems, and solve the key issue of the effect on SPECT image resolution from the strong magnetic field.

REFERENCES

[1]: Cherry, S. R. (2004). "In vivo molecular and genomic imaging: new challenges for imaging physics." *Physics in Medicine and Biology* 49(3): R13-48.

[2]: Tai, Y. C.,Ruangma, A., Laforest, R., Siegel, S., Newport, D. F. (2003). "Performance evaluation of the microPET (R) Focus: A second generation small animal PET system." *Journal of Nuclear Medicine* 44(5): 159p-160p.

[3]: http://psychology.wikia.com/wiki/Positron_emission_tomography

[4]: Research and Researchers Dana Foundation 2008 Annual Report

[5]: McElroy, D. P., MacDonald, L. R., Beekman, F. J., Wang, Y. C., Patt, B. E., Iwanczyk, J. S., Tsui, B. M. W., Hoffman, E. J. (2002). "Performance evaluation of A-SPECT: A high resolution desktop pinhole SPECT system for imaging small animals." *IEEE Transactions on Nuclear Science* 49(5): 2139-2147.

[6]: Weisenberger, A. G., Wojcik, R., Bradley, E. L., Brewer, P., Majewski, S., Qian, J., Ranck, A., Saha, M. S., Smith, K., Smith, M. F., Welsh, R. E. (2003). "SPECT-CT system for small animal imaging." *IEEE Transactions on Nuclear Science* 50(1): 74-79.

[7]: Furenlid, L. R., Wilson, D. W., Chen, Y. C., Kim, H., Pietraski, P. J., Crawford, M. J., Barrett, H. H. (2004). "FastSPECT II: A second-generation high-resolution dynamic SPECT imager." *IEEE Transactions on Nuclear Science* 51(3): 631-635.

[8]: Kastis, G. A., Furenlid, L. R., Wilson, D. W., Peterson, T. E., Barber, H. B., Barrett, H. H. (2004). "Compact CT/SPECT small-animal imaging system." *IEEE Transactions on Nuclear Science* 51(1): 63-67.

[9]: Meikle, S. R., Kench, P., Weisenberger, A. G., Wojcik, R., Smith, M. F., Majewski, S., Eberl, S., Fulton, R. R., Rosenfeld, A. B., Fulham, M. J. (2002). "A prototype coded aperture detector for small animal SPECT." *IEEE Transactions on Nuclear Science* 49(5): 2167-2171.

[10]: Smith, M. F., Majewski, S., Weisenberger, A. G. (2003). "Optimizing pinhole and parallel hole collimation for scintimammography with compact pixellated detectors." *IEEE Transactions on Nuclear Science* 50(3): 321-326.

[11]: Schramm, N. U., Behe, M., Schurrat, T., Engeland, U., Ebel, G., Behr, T. M. (2003). "Multi-pinhole SPECT: Recent results of an animal imaging system." *Journal of Nuclear Medicine* 44(5): 9P-10P.

[12]: Beekman, F. J., van der Have, F., Vastenhouw, B., van der Linden, A. J. A., van Rijk, P. P., Burbach, J. P. H., Smidt, M. P. (2005). "U-SPECT-I: A novel system for submillimeter-resolution tomography with radiolabeled molecules in mice." *Journal of Nuclear Medicine* 46(7): 1194-1200.

[13]: Schramm, N. U., Lackas, C., Gershman, B., Norenberg, J. P., deJong, M. (2007). "Improving resolution, sensitivity and applications for the NanoSPECT/CT: A high-performance SPECT/CT imager for small-animal research." *European Journal of Nuclear Medicine and Molecular Imaging* 34: S226-S227.

[14]: Lackas, C., Schramm, N.U., Hoppin, J.W., Hallin, H. (2005) "NanoSPECT: A Compact Multi-Pinhole SPECT Camera with Sub-Millimeter Resolution for Small-Animal Imaging."

[15]: Kinahan, P. E., Hasegawa, B. H., Beyer, T. (2003). "X-ray-based attenuation correction for positron emission tomography/computed tomography scanners." *Seminars in Nuclear Medicine* 33(3): 166-179.

[16]: Kinahan, P. E., Townsend, D. W., Beyer, T., Sashin, D. (1998). "Attenuation correction for a combined 3D PET/CT scanner." *Medical Physics* 25(10): 2046-2053.

[17]: Bockisch, A., Beyer, T., Antoch, G., Freudenberg, L. S., Kuhl, H., Debatin, J. F., Muller, S. P. (2004). "Positron emission tomography/computed tomography-imaging protocols, artifacts, and pitfalls." *Molecular Imaging and Biology* 6(4): 188-199.

[18]: Goertzen, A. L. (2003). "Development of a Combined microPET and microCT System for Mouse Imaging." Doctoral dissertation, University of California Los Angeles, *2003*.

[19]: Goertzen, A. L., Meadors, A. K., Silverman, R. W., Cherry, S. R. (2002). "Simultaneous molecular and anatomical imaging of the mouse in vivo." *Physics in Medicine and Biology* 47(24): 4315-4328.

[20]: Meng, L. J., Fu, G., Roy, E. J., Suppe, B., Chen, C. T. (2009). "An ultrahigh resolution SPECT system for I-125 mouse brain imaging studies." *Nuclear Instruments & Methods in Physics Research Section a-Accelerators Spectrometers Detectors and Associated Equipment* 600(2): 498-505.

[21]: Catana, C., Wu, Y. B., Judenhofer, M. S., Qi, J. Y., Pichler, B. J., Cherry, S. R. (2006). "Simultaneous acquisition of multislice PET and MR images: Initial results with a MR-compatible PET scanner." *Journal of Nuclear Medicine* 47(12): 1968-1976.

[22]: Zhang, N., Grazioso, R. F., Doshi, N. K., Schmand, M. J. (2006). "RF transformer coupled multiplexing circuits for APD PET detectors." *IEEE Transactions on Nuclear Science* 53(5): 2570-2577.

[23]: Woody, C., Schlyer, D., Vaska, P., Tomasi, D., Solis-Najera, S., Rooney, W., Pratte, J. F., Junnarkar, S., Stoll, S., Master, Z., Purschke, M., Park, S. J., Southekal, S., Kriplani, A., Krishnamoorthy, S., Maramraju, S., O'Connor, P., Radeka, V. (2007). "Preliminary studies of a simultaneous PET/MRI scanner based on the RatCAP small animal tomograph." *Nuclear Instruments & Methods in Physics Research Section a-Accelerators Spectrometers Detectors and Associated Equipment* 571(1-2): 102-105.

[24]: Grazioso, R., Zhang, N., Corbeil, J., Schmand, M., Ladebeck, R., Vester, M., Schnur, G., Renz, W., Fischer, H. (2006). "APD-based PET detector for simultaneous PET/MR imaging." *Nuclear Instruments & Methods in Physics Research Section a-Accelerators Spectrometers Detectors and Associated Equipment* 569(2): 301-305.

[25]: Pichler, B. J., Judenhofer, M. S., Catana, C., Walton, J. H., Kneilling, M., Nutt, R. E., Siegel, S. B., Claussen, C. D., Cherry, S. R. (2006). "Performance test of an LSO-APD detector in a 7-T MRI scanner for simultaneous PET/MRI." *Journal of Nuclear Medicine* 47(4): 639-647.

[26]: Strul, D., Cash, D., Keevil, S. F., Halsted, P., Williams, S. C. R., Marsden, P. K. (2003). "Gamma shielding materials for MR-compatible PET." *IEEE Transactions on Nuclear Science* 50(1): 60-69.

[27]: Wagenaar, D.J., Nalcioglu, O., Muftuler, L.T., Szawlowski, M.,Kapusta, M., Pavlov, N., Meier, D., Maehlum, G., Patt, B.E. (2006). "Development of MRI-Compatible Nuclear Medicine Imaging Detectors", *Nuclear Science Symp, and Medical Imaging Conf,* vol.3, pp.1825-1828.

[28]: Hamamura, M. J., Ha, S., Roeck, W. W., Muftuler, L. T., Wagenaar, D., Meier, D., Patt, B. E., Nalcioglu, O. (2010). "Development of an MR-compatible SPECT system (MRSPECT) for simultaneous data acquisition." *Physics in Medicine and Biology* 55(6): 1563-1575.

[29]: Breton, E., Choquet, P., Goetz, C., Kintz, J., Erbs, P., Rooke, R., Constantinesco, A. (2007). "Dual SPECT/MR imaging in small animal." *Nuclear Instruments & Methods in Physics Research Section a-Accelerators Spectrometers Detectors and Associated Equipment* 571(1-2): 446-448.

[30]: Goetz, C., Breton, E., Choquet, P., Israel-Jost, V., Constantinesco, A. (2008). "SPECT low-field MRI system for small-animal imaging." *Journal of Nuclear Medicine* 49(1): 88-93.

[31]: Meng, L. J., Tan, J. W., Spartiotis, K., Schulman, T. (2009). "Preliminary evaluation of a novel energy-resolved photon-counting gamma ray detector." *Nuclear Instruments & Methods in Physics Research Section a-Accelerators Spectrometers Detectors and Associated Equipment* 604(3): 548-554.

[32]: Ntziachristos, V., Bremer, C., Weissleder, R. (2003). "Fluorescence imaging with near-infrared light: new technological advances that enable in vivo molecular imaging." *European Radiology* 13(1): 195-208.

[33]: Contag, C. H., Bachmann, M. H. (2002). "Advances in vivo bioluminescence imaging of gene expression." *Annual Review of Biomedical Engineering* 4: 235-260.

[34]: Foster, F. S., Zhang, M. Y., Zhou, Y. Q., Liu, G., Mehi, J., Cherin, E., Harasiewicz, K. A., Starkoski, B. G., Zan, L., Knapik, D. A., Adamson, S. L. (2002). "A new ultrasound instrument for in vivo microimaging of mice." *Ultrasound in Medicine and Biology* 28(9): 1165-1172.

[35]: Arlt, R., Gryshchuk, V., Sumah, P. (1999). "Gamma spectrometric characterization of various CdTe and CdZnTe detectors." *Nuclear Instruments & Methods in Physics Research Section a-Accelerators Spectrometers Detectors and Associated Equipment* 428(1): 127-137.

[36]: Brzymialkiewicz, C. N., Tornai, M. P., McKinley, R. L., Bowsher, J. E.. (2005). "Evaluation of fully 3-D emission mammotomography with a compact cadmium zinc telluride detector." *IEEE Transactions on Medical Imaging* 24(7): 868-877.

[37]: Guerin, L., Verger, L., Rebuffel, V., Monnet, O.. (2008). "A new architecture for pixellated solid state gamma camera used in nuclear medicine." *IEEE Transactions on Nuclear Science* 55(3): 1573-1580.

[38]: Verger, L., Gentet, A. C., Gerfault, L., Guillemaud, R., Mestais, C., Monnet, O., Montemont, G., Petroz, G., Rostaing, J. P., Rustique, J.. (2004). "Performance and perspectives of a CdZnTe-based gamma camera for medical imaging." *IEEE Transactions on Nuclear Science* 51(6): 3111-3117.

[39]: Kim, H., Furenlid, L. R., Crawford, M. J., Wilson, D. W., Barber, H. B., Peterson, T. E., Hunter, W. C. J., Liu, Z. L., Woolfenden, J. M., Barrett, H. H.. (2006). "SemiSPECT: A small-animal single-photon emission computed tomography (SPECT) imager based on eight cadmium zinc telluride (CZT) detector arrays." Medical Physics 33(2): 465-474.

[40]: Singh, M., Doty, F. P., Friesenhahn, S. J., Butler, J. F.. (1995). "Feasibility of Using Cadmium-Zinc-Telluride Detectors in Electronically Collimated Spect." *IEEE Transactions on Nuclear Science* 42(4): 1139-1146.

[41]: Singh, M. and E. Mumcuoglu (1998). "Design of a CZT based BreastSPECT system." *IEEE Transactions on Nuclear Science* 45(3): 1158-1165.

[42]: Accorsi, R., Celentano, L., Laccetti, P., Lanza, R. C., Marotta, M., Mettivier, G., Montesi, M. C., Roberti, G., Russo, P.. (2008). "High-resolution I-125 small animal imaging with a coded aperture and a hybrid pixel detector." *IEEE Transactions on Nuclear Science* 55(1): 481-490.

[43]: Spartiotis, K., Leppanen, A., Pantsar, T., Pyyhtia, J., Laukka, P., Muukkonen, K., Mannisto, O., Kinnari, J., Schulman, T.. (2005). "A photon counting CdTe gamma- and X-ray camera." *Nuclear Instruments & Methods in Physics Research Section a-Accelerators Spectrometers Detectors and Associated Equipment* 550(1-2): 267-277.

[44]: Lutz G., Semiconductor Radiation Detectors, 1st Ed., Springer, New York, 1999, p232, ISBN 978-3-540-71678-5.

[45]: Wermes, N. (2004). "Trends in pixel detectors: Tracking and Imaging." *IEEE Transactions on Nuclear Science* 51(3): 1006-1015.

[46]: Lutz G., Semiconductor Radiation Detectors, 1st Ed., Springer, New York, 1999, p205, ISBN 978-3-540-71678-5.

[47]: Meng, L. J., Tan, J. W., Spartiotis, K., Schulman, T.. (2009). "Preliminary evaluation of a novel energy-resolved photon-counting gamma ray detector." *Nuclear Instruments & Methods in Physics Research Section a-Accelerators Spectrometers Detectors and Associated Equipment* 604(3): 548-554.

[48]: He, Z. (2001). "Review of the Shockley-Ramo theorem and its application in semiconductor gamma-ray detectors." *Nuclear Instruments & Methods in Physics Research Section a-Accelerators Spectrometers Detectors and Associated Equipment* 463(1-2): 250-267.

[49]: http://geant4.cern.ch/

[50]: Knoll K. F., Radiation Detection and Measurement, 3rd Ed., Wiley & Son, New York, 1999, p115, ISBN 0-470-07338-5.

[51]: Benoit, M. and L. A. Hamel (2009). "Simulation of charge collection processes in semiconductor CdZnTe gamma-ray detectors." *Nuclear Instruments & Methods in Physics Research Section a-Accelerators Spectrometers Detectors and Associated Equipment* 606(3): 508-516.

[52]: http://ansoft.com/products/em/maxwell/

[53]: Castoldi, A., Gatti, E., Manzari, V., Rehak, P.. (1997). "Performance of silicon drift detectors in a magnetic field." *Nuclear Instruments & Methods in Physics Research Section a-Accelerators Spectrometers Detectors and Associated Equipment* 399(2-3): 227-243.

[54]: Meng, L. J. and Z. He (2005). "Estimate interaction timing in a large volume HgI2 detector using cathode pulse waveforms." *Nuclear Instruments & Methods in Physics Research Section a-Accelerators Spectrometers Detectors and Associated Equipment* 545(1-2): 234-251.

[55]: Knoll K. F., Radiation Detection and Measurement, 3rd Ed., Wiley & Son, New York, 1999, p480, ISBN 0-470-07338-5.

[56]: http://home.planet.nl/~wilt0003/vdw-1-products-06.htm

[57]: Tan J. W., Cai L., and Meng L. J. (2009). " A prototype of the MRI-compatible ultra-high resolution SPECT for in vivo mice brain imaging," *IEEE Nuclear Science Symposium and Medical Imaging Conference*, Orlando,FL.

[58]: Meng L. J., Tan J. W., Cai L. (2010). "Sub-500 μm Resolution SPECT Imaging inside a 3T MRI Scanner." *IEEE Nuclear Science Symposium and Medical Imaging Conference*, Knoxville, TN.

[59]: Jaszczak, R. J., Li, J. Y., Wang, H. L., Zalutsky, M. R., Coleman, R. E.. (1994). "Pinhole Collimation for Ultra-High-Resolution, Small-Field-of-View SPECT." *Physics in Medicine and Biology* 39(3): 425-437.

[60]: Hudson, H. M. and R. S. Larkin (1994). "Accelerated image reconstruction using ordered subsets of projection data." *IEEE Trans Med Imaging* 13(4): 601-9.

[61]: Shepp, L. A. and Y. Vardi (1982). "Maximum likelihood reconstruction for emission tomography." IEEE Trans Med Imaging 1(2): 113-22.